SHOCK-WAVE PROPERTIES AND HIGH-PRESSURE EQUATIONS OF STATE OF GEOPHYSICALLY IMPORTANT MATERIALS

Thesis by

Mark Bruce Boslough

In Partial Fulfillment of the Requirements

of the Degree of

Doctor of Philosophy

California Institute of Technology

Pasadena, California

1984

(submitted September 21, 1983)

This thesis is dedicated

to the memory of my father, Bruce

and to my mother, Norma

Acknowledgements

I sincerely thank Thomas J. Ahrens for his continual support, advice, and encouragement during my years at Caltech. Greg Lyzenga and Joana Vizgirda were particularly helpful when I was getting started, and I am grateful for the profitable and enjoyable association with them. The work in this thesis could never have been carried out without the help of Papo Gelle and Mike Long, whose work in the shock-wave lab was certainly above and beyond the call of duty.

It is impossible to list everyone from whose association I benefitted from intellectually or personally, or in some way made the writing of this thesis easier, but I wish to thank Roger Aines, Don Anderson, JoAnn Anderson, Jeannette Arnold, Doug Bakker, Jay Bass, Ellen Bus, Warren Ginn, Peter Goldreich, Ralph James, Raymond Jeanloz, Ed Jerbic, Ken-ichi Kondo, Manfred Lange, Jim Long, Chuck Manning, Rob Manning, Mickey McConnell, Art Mitchell, Bill Nellis, Sally Rigden, George Rossman, Doug Schmitt, Edgard Schweig, Malcolm Somerville, Svend Sondergaard, Dave Stevenson, Bob Svendson, Jim Trainor, Mario Vassiliou, Peter Watt, Ray Weldon, Sue Yamada, and Barton Zweibach. A special thanks to those who added to the quality of subterranean life.

I am grateful for the financial support provided by the National Science Foundation, the National Aeronautics and Space Administration, and the Lawrence Livermore National Laboratory.

Abstract

Shock wave (Hugoniot), shock temperature, and release data are presented for several geophysically important, refractory materials. A sensitive multi-channel optical pyrometer was developed to measure shock temperatures (2500 to 5600°K at pressures from 48 to 117 GPa) in anorthite ($CaAl_2Si_2O_8$) glass. Shock temperatures of 3750 to 6000°K at pressures from 140 to 182 GPa were measured in calcium oxide (CaO). Temperature data were used to constrain the energetics of the B1-B2 phase transition at 70 GPa in CaO, and to construct a finite-strain equation of state for CaO consistent with previous Hugoniot data.

The new CaO equation of state was used with equation of state parameters of other oxides to construct a theoretical mixed oxide Hugoniot of anorthite, which is in agreement with new Hugoniot data above about 50 GPa, determined using new experimental techniques developed in this study. The mixed oxide model, however, overestimates the shock temperatures, and does not accurately predict measured release paths. Both shock temperature and release data for anorthite indicate that several high pressure phase regions of stability exist above 50 GPa. A similar mixed oxide Hugoniot was constructed for lunar gabbroic anorthosite, and agrees with two new Hugoniot points at 120 GPa. Release data from lunar gabbroic anorthosite shocked to 120 GPa give evidence for shock vaporization.

Because the densities and bulk properties of CaO and the high pressure phase or phases of anorthite are so close to those determined seismologically

for the lower mantle, the amount of these materials present in the lower mantle is not well constrained. The possibility of significant enrichment of the lower mantle in these refractory materials, as predicted by inhomogeneous accretion models, is still open.

A simple model is developed to explain the measured time dependences of radiated light in the shock temperature experiments, and constrain the absorption coefficient of the shocked material. The absorption coefficient is found to be an increasing function of shock pressure in shocked anorthite glass.

Hugoniot and release paths were determined using electromagnetic particle velocity gauges for San Gabriel anorthosite and San Marcos Gabbro shocked to peak stresses between 5 and 11 GPa. The data indicate a loss of shear strength in both rocks, and a partial phase transition of the anorthosite to a denser phase. This implies that estimates of shock wave attenuation in these materials based on elastic-plastic models are too high, and previously calculated amounts of internal energy gained by surface materials from impact or explosion events have been underestimated.

Table of Contents

Introduction

Dynamic compression of materials by strong shock waves provides a unique method by which matter can be studied in the laboratory at high pressures and temperatures. Shock waves have become a tool of both physicists and geophysicists, and furnish a research area rich in possibilities for experimental innovation. The purpose of this thesis is threefold: to develop new experimental shock wave methods to study condensed matter under high pressure, to explain the physics of experimental observations, and to apply the knowledge gained to problems in solid earth geophysics.

In most experimental shock wave work, only the Hugoniot state is determined. The Hugoniot curve, or locus of shock states of a material with a specified initial state, is useful in modeling high pressure bulk properties and detecting phase transformations with large volume changes, but its sensitivity to energies of transformation, specific heat, and Gruneisen parameter is limited. The usefulness of shock temperature measurements in constraining these thermal properties has been demonstrated, as well as the need for more precision and sensitivity in shock temperature measurement. A new optical pyrometer was designed with this purpose, and is described in Appendix I. Calibration of this instrument is outlined in Appendix II, and determination of temperatures from measured spectral radiances, along with the data, is presented in Appendix III.

Chapter 1 illustrates the usefulness of shock temperature data in supplementing Hugoniot data to constrain the physical properties of materials at high pressure. With both types of data taken together, the energy of the B1-B2 phase transformation of CaO is strongly constrained. Further constraint is provided for both heat capacity and Gruneisen parameter. Chapter 2 points out the application of temperature data to the detection of phase transformations which are unresolvable with Hugoniot data alone, in the case of anorthite.

Experimental shock wave research at 100 GPa pressures requires a large investment for little data. It is therefore important to glean as much information as possible from a given experiment. Chapter 3 contains an outline of three approaches used to obtain shock wave Hugoniot data from experiments with other primary objectives.

Hugoniot data by itself is useful in determining high pressure bulk properties of materials (i.e. bulk modulus, pressure derivative of the bulk modulus, and zero pressure density of high pressure phases). Chapter 1 provides a good example of an "inverse" problem--that is a least squares fit for these parameters to measured Hugoniot data with an assumed functional form for the high pressure behavior (third order finite strain). On the other hand, Chapter 3 illustrates the "forward" problem, in which these parameters are calculated based on an *a priori* model--in this case a mixture of the oxide components of anorthite and lunar anorthosite--and a theoretical Hugoniot is calculated. The validity of the model is checked by comparing the theoretical Hugoniot to the measured Hugoniot.

Release data can supplement temperature data as indicators of phase transformations. Partial release states of shocked anorthite delineate possible

regions of stability in Chapter 3. Partial release states of shocked lunar anorthosite indicate vaporization upon release. At lower stresses, release data can detect the loss of shear strength in shocked materials, as in Chapter 4 for San Gabriel anorthosite and San Marcos gabbro. In Appendix IV, an experimental technique is outlined which can determine an entire decompression path in a single experiment. This approach may eventually be applied to the problem of determining principal isentropes of fluids.

The behavior of materials under high pressure is of geophysical interest for two principal reasons. First, the static pressures present in the earth's interior extend to 370 GPa, and knowledge of the high pressure physics of earth materials is a prerequisite to understanding the earth's interior. Second, because of the high dynamic pressures existing during the hypervelocity impact of bodies, an understanding of behavior of earth materials under shock is necessary in order to model impact and accretional processes.

In Chapters 1 and 3, the bulk properties of CaO and of the high pressure phases of anorthite are compared to those determined seismologically for the lower mantle. Because of the similarity in bulk properties, the possibility exists for an enrichment of the lower mantle in these materials, as predicted by inhomogeneous accretion theories.

The shock vaporization of lunar anorthosite suggested by the data in Chapter 3 has implications in cratering mechanics, and also supports the possibility of an impact-origin of the moon. The measurement of rarefaction wave velocities in Chapter 4 will allow more precise calculations to be made of shock wave decay in natural impacts, and more accurate estimates of energy partitioning in such events.

Chapter 1

Shock Temperatures in CaO

ABSTRACT

Blackbody temperatures of CaO shocked to pressures from 140 to 182 GPa have been measured in the 3750 to 6000 °K range using the Lawrence Livermore National Laboratory light gas gun. These shock temperatures, along with Hugoniot, porous Hugoniot, and isothermal data, are used to construct equations of state for the high pressure (B2) phase of CaO. The zero-pressure density of the B2 phase is between 3.8 and 4.0 Mg/m^3, and the B1-B2 transition energy is 2.1 to 2.3 kJ/g. The density and bulk modulus at pressures from 70 to 130 GPa are similar to seismically determined values for the lower mantle. Thus, mixed-oxide models of the lower mantle will be insensitive to the quantity of CaO assumed.

Introduction

The calcium-bearing minerals perovskite ($CaTiO_3$), melilite ($Ca_2Al_2SiO_7$–$Ca_2MgSi_2O_7$), diopside ($CaMgSi_2O_6$) and anorthite ($CaAl_2Si2O_8$) are among the first phases to condense from the solar nebula (Grossman and Larimer, 1974). They are of geophysical importance because they are hosts for the

actinide series elements U and Th, and because Ca is the most common large-ion lithophile element in the solar system (Ross and Aller, 1976). In inhomogeneous accretion models (Turekian and Clark, 1969), the lower mantle is significantly enriched in these minerals. At the high pressures of the lower mantle (70 to 135 GPa), these minerals transform into a series of high pressure phases (Liu, 1978, 1979) whose high pressure equation of state properties may be close to those of their equivalent mixed oxides (Boslough *et al.*, 1983). Thus, the high pressure behavior of CaO is of interest.

CaO exists in the B1 (NaCl) phase under standard conditions, and densities calculated by extrapolation of its compression curve (e.g. Perez-Albuerne and Drickamer, 1965, Chang and Graham, 1977, Mammone *et al.*, 1981) to lower mantle pressures are significantly lower than seismologically determined lower mantle densities (e.g. Dziewonski *et al.*, 1975, Anderson and Hart, 1976, Dziewonski and Anderson, 1981, Fig. 1-1). Jeanloz *et al.* (1979) found that at about 70 GPa, CaO undergoes a phase transition to the B2 (CsCl) structure, which is denser than the B1 phase. At high pressure the B2 phase of CaO has densities and compressibilities which are close to those of the mantle, according to Hugoniot data (Jeanloz and Ahrens, 1980).

The reason for conducting shock temperature experiments on this material is to characterize its thermal properties at high pressures. Not only can the energetics of the B1-B2 phase transition be constrained, but the possible existence of further phase transitions, such as melting, can be determined. The temperature-pressure Hugoniot is much more sensitive to such transitions than is the pressure-density Hugoniot (Lyzenga *et al.*, 1983). Armed with well-constrained transition energies in this way, the adiabatic compression curve

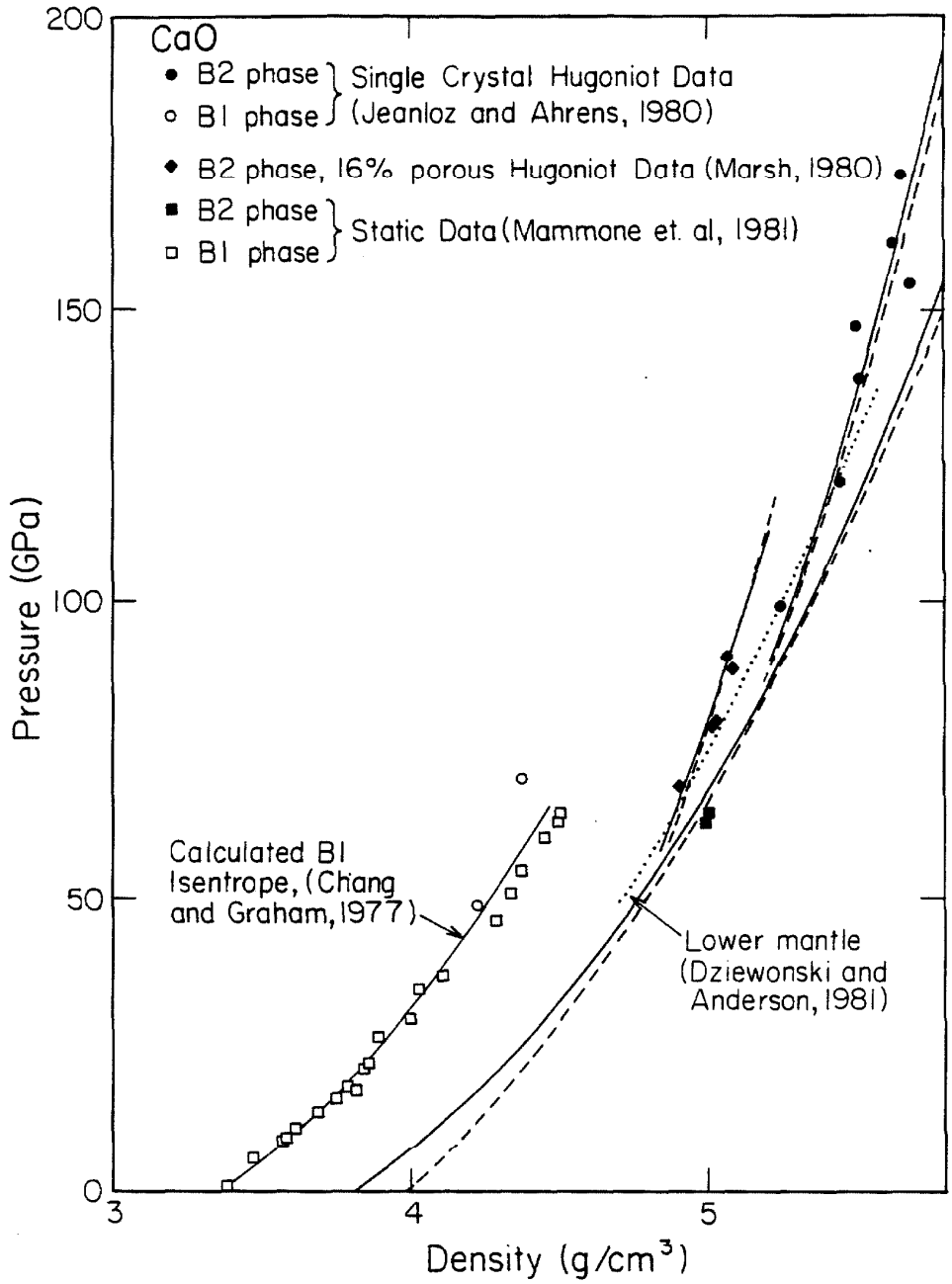

Fig. 1-1 Single crystal Hugoniot data (Jeanloz and Ahrens, 1980), porous Hugoniot data (Marsh, 1980), and static isothermal data (Mammone et al., 1981) for CaO. Solid and dashed curves are low and high zero-pressure density fits to B2 data, respectively. Calculated B1 isentrope based on ultrasonically determined values of K_{OS}=112.5 GPa and K'_{OS}=4.8, of Chang and Graham (1977). Lower mantle curve based on PREM model of Dziewonski and Anderson (1981).

(K_{0S} and K'_{0S} in the Birch-Murnaghan approximation, Davies, 1973) can be determined with better precision.

Experimental Methods

The CaO samples were obtained from Oak Ridge National Laboratory where they were grown by an arc-fusion process. They are from the same boule as samples used by Jeanloz and Ahrens (1980), and are free from all but trace impurities. Because optical methods are used to determine the shock temperature, samples ideally should be perfectly transparent. These samples appear bluish in color, due to the Rayleigh scattering of white light by microbubbles inherently present in highly pure crystals grown by the arc-fusion method (Abraham *et al.*, 1971). A Cary 17 spectrophotometer was used to measure the absorbance at visible and near infrared wavelengths (Fig. 1-2). It demonstrates an approximate λ^4 dependence, as is expected with Rayleigh scattering (Jackson, 1975).

There is some evidence for minute amounts of hydration in the form of portlandite ($Ca(OH)_2$) in infrared spectra (Jeanloz and Ahrens, 1980). Both the microbubbles and the portlandite should lead to bulk densities which are lower than the x-ray density. This is observed; densities of samples used range from 3.341 to 3.345 Mg/m^3, compared to the x-ray density of 3.345 Mg/m^3. Samples were approximately 3 mm thick and 17 mm wide, and both surfaces were polished to optical quality. They were mounted on copper driver plates and shocked to pressures from 140 to 182 GPa by 2 mm thick copper and tantalum flyer plates fired from the Lawrence Livermore Laboratory light gas gun (Mitchell and Nellis, 1981) at speeds from 6.3 to 7.1 km/s.

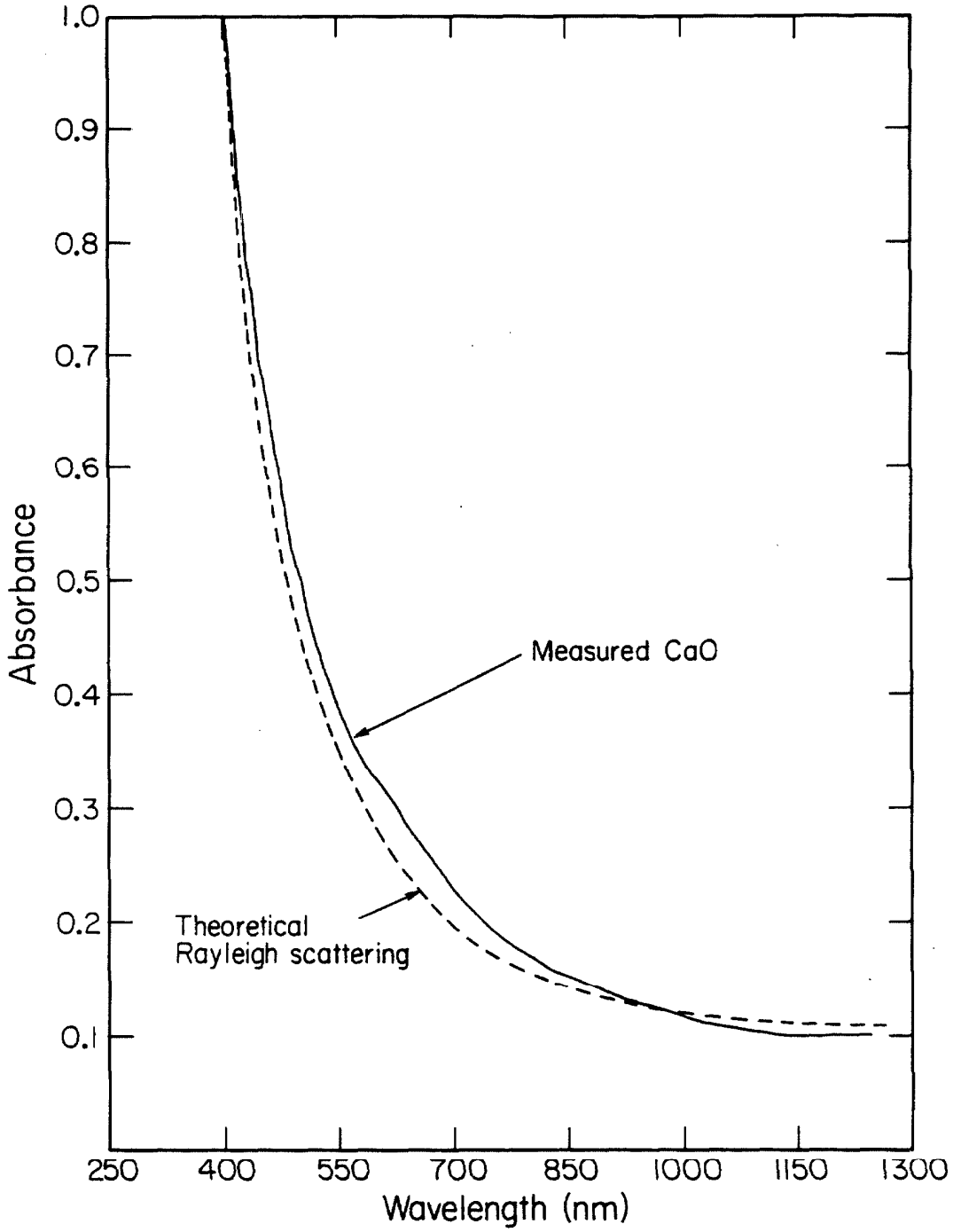

Fig. 1-2 Absorbance spectrum of a representative sample of CaO, measured with Cary 17 Spectrophotometer. Theoretical curve is of form: $[h_o (\frac{\lambda_o}{\lambda})^4 + \mu]d$ with $h_o d_o = 1.0$, $\mu d_o = 0.1$, and $\lambda_o = 400$nm.

The projectile velocity is determined by flash radiography, and this is used in an impedance match solution (Rice *et al.*, 1958) to calculate the shock pressure in the CaO. Thermal radiation is emitted from the shocked material and transmitted through the unshocked portion of the sample, which acts as a window. The intensity of the light is measured at six wavelengths in the visible and near infrared with an optical pyrometer (Lyzenga and Ahrens, 1979). The measured spectral radiances are used to calculate the shock temperature.

In an ideal situation in which the sample is initially perfectly transparent, the shocked sample is perfectly opaque, and the shock wave is planar, parallel to the sample faces, and exhibits no time dependent behavior, the shock wave profile would appear as in Fig. 1-3. At time t_1, the shock wave enters the transparent sample from the opaque driver plate. The shocked material immediately begins to radiate at an intensity determined by its temperature, and the signal increases suddenly to R_S. As the shock wave approaches the free surface, it is steady so the signal is constant. At time t_2 the shock reaches the free surface and reflects as a rarefaction. The light intensity drops to R_R, characteristic of the residual, post-shock temperature.

Results and Discussion

A typical shot record from this study is shown in Fig. 1-4. It deviates from the ideal case in two principal ways. First, the rise from t_a to t_b is not instantaneous, but is nearly 50 ns. Second, the light intensity is not constant during shock transit, but increases approximately linearly with time.

The long rise time cannot be accounted for by the HP5082-4207 photodiode rise time, which is approximately 1 ns (Lyzenga and Ahrens, 1979) nor is it due

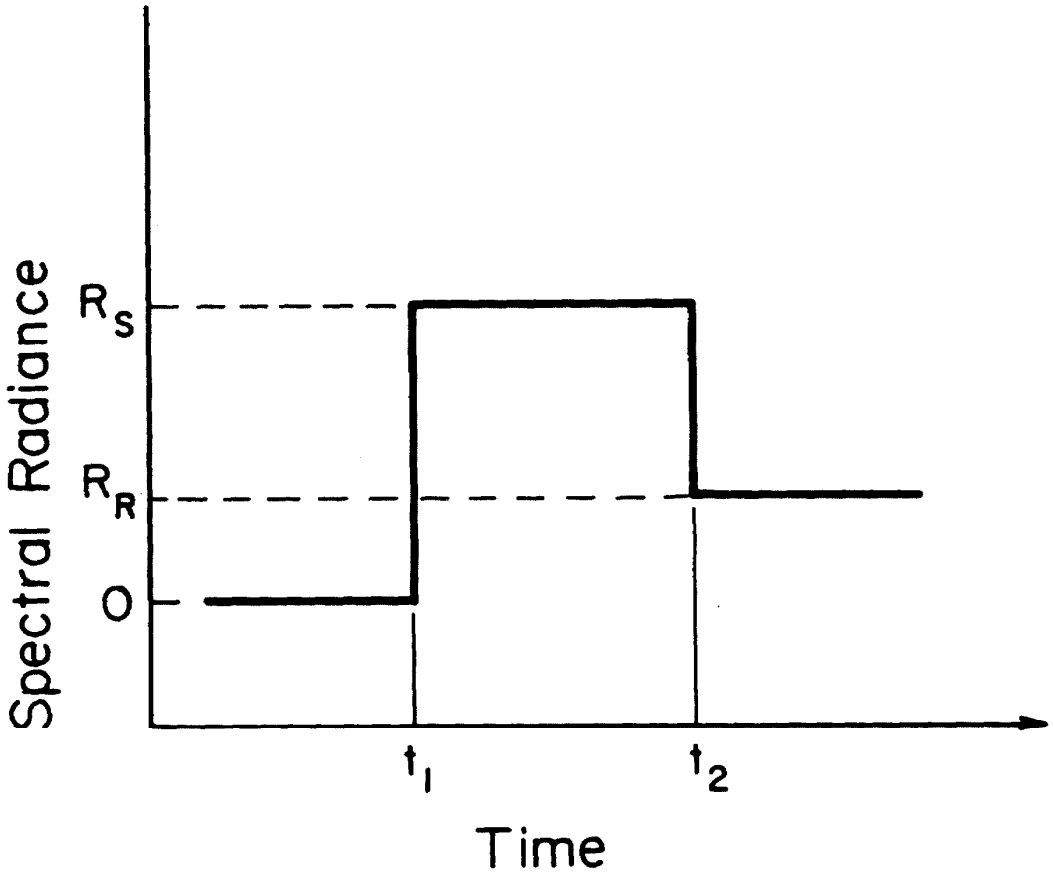

Fig. 1-3 Hypothetical shock temperature record for ideal case where initial state is perfectly transparent and shock state is perfect black body. Shock wave enters sample at time t_1 and reaches free surface at t_2. R_S and R_R are spectral radiances characteristic of shock temperature and post-shock temperature, respectively.

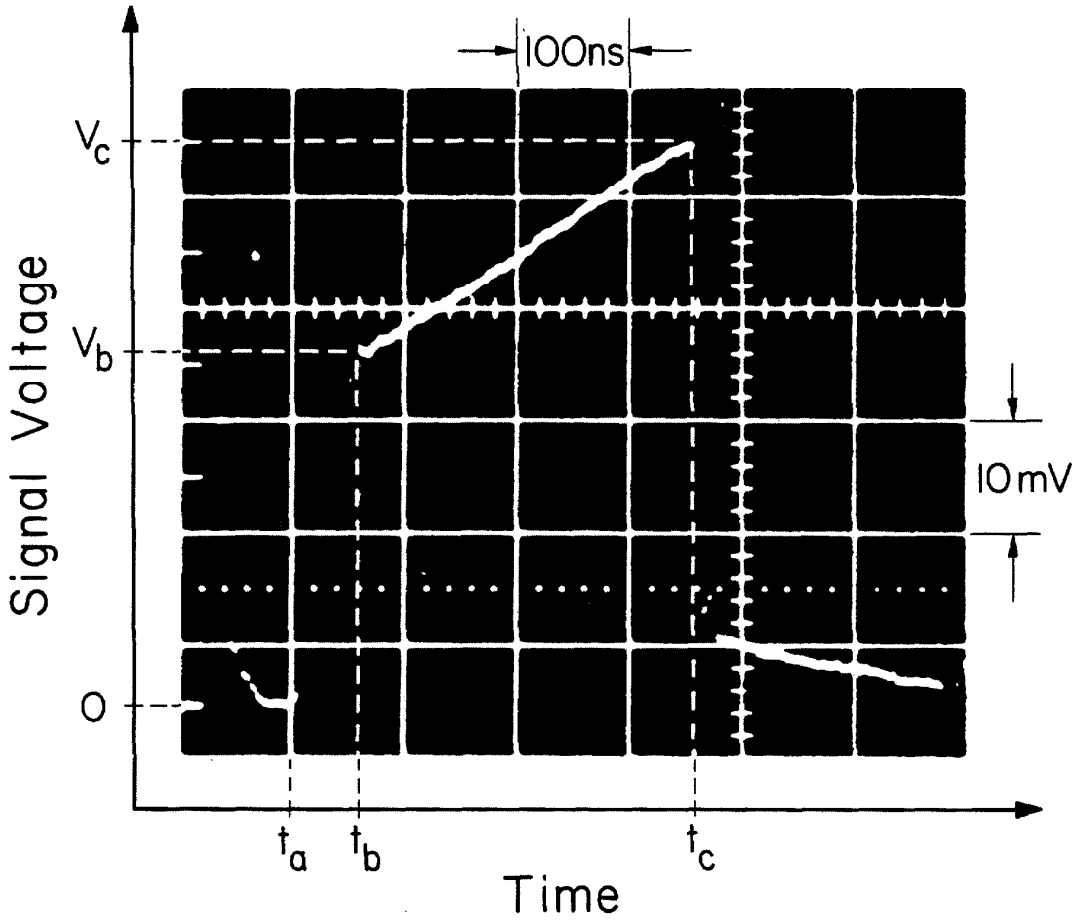

Fig. 1-4 Shock temperature record for shot Ca03T at λ = 508nm. Time t_a: shock wave enters sample, light is scattered indirectly to detector. Time t_b: shock wave enters detector field of view. Time t_c: shock wave reaches free surface; spectral radiance is read at this point.

to shock wave tilt within the field of view of the photodiode. The active area of the detector is about 1 mm in diameter, and the optics demagnify the image by a factor of 0.43, so the field of view is 2.3 mm. The maximum projectile tilt is 0.05 radians (Mitchell and Nellis, 1981). At typical projectile velocities of 6mm/ μs, the maximum time interval for the line of intersection between shock front and driver/sample interface to cross the field of view is 20 ns; insufficient to account for the measured time lag. Because the samples are strong optical scatterers, the material within the detector field of view begins scattering light from the shock wave the instant it enters at one edge of the sample. The line of intersection between shock front and driver/sample interface can take as much as 70 ns to sweep across the 8 mm from the sample edge into the photodetector field of view, accounting for the long observed rise times. Unfortunately, interference from this scattered light precludes precise determination of the shock transit times, so these experiments cannot be used to determine Hugoniot states (e.g. Boslough *et al.*, 1983 for anorthite glass).

The approximately linear increase in light intensity with time as the shock wave propagates through the sample can be explained by scattering and absorption of light. The intensity of light transmitted through a medium is decreased by a factor of $e^{-(\mu+h)d}$, where μ is the linear absorption coefficient, h is the extinction coefficient due to scattering, and d is the light propagation distance through the medium. This distance is $(t_c-t)U_s$, where U_s is the shock velocity, and t_c is the time of shock arrival at the free surface. For $(\mu+h)d \ll 1$, the light intensity is

$$I = I_o(1 - (\mu + h)(t_c - t)U_s) \qquad (1\text{-}1)$$

which increases linearly with time. At $t=t_c$, the measured intensity is equal to the radiated intensity, so shot records were read at free surface arrival t_c.

The ratio of initial intensity I_b to final intensity I_c was found to be smaller at shorter wavelengths, consistent with Rayleigh scattering. In Table 1-1, measured values are tabulated for shot CaO3T, along with the best fitting theoretical values which assume a wavelength dependent Rayleigh scattering component $h = h_0 \left(\frac{\lambda_0}{\lambda}\right)^4$ and a wavelength independent absorption component μ. The effects of the two sources of attenuation are about equal at λ=450 nm, and the wavelength independent component dominates at λ=792 nm.

Shock Temperatures

Two approaches were used to determine shock temperatures from optical pyrometer shot records. Both involve least squares fitting the spectral radiance data to a Planck distribution function (Appendix III). In method (a), both the emissivity and temperature are varied to obtain the best fit. In method (b) only the temperature is allowed to vary; the emissivity is assumed to be unity--equivalent to the assumption of a black body.

Temperatures and emissivities calculated via methods (a) and (b) are presented in Table 1-2 with the standard deviations σ and mean fractional deviations $\frac{\sigma}{\bar{N}_\lambda}$. Pressures are calculated from an impedance match solution using the measured impact velocity and the known Hugoniots of the flyer materials (McQueen *et al.*, 1970) and CaO (Jeanloz and Ahrens, 1980). In two of the three experiments the best emissivities are greater than unity--an unphysical situation. In all experiments method (a) does not give significantly better agreement

Table 1-1

Shot Ca03T measured and theoretical intensity ratios

λ (nm)	$\xi_{measured}$	$\xi_{theoretical}$
450	.56	.56
508	.46	.46
545	.37	.41
598	.42	.37
650	.37	.35
792	.29	.32

$\xi_{measured} = I_b / I_c$

$\xi_{theoretical} = \left[\mu + h_o(\lambda_o/\lambda)^4\right] d_o$

$\left\{\begin{matrix} h_o d_o = .27 \\ \mu d_o = .29 \end{matrix}\right\}$ best fit to data

λ_o = 450 nm

Table 1-2

Calcium Oxide Shock Temperature Data

Shot	Flyer/Driver Material	Projectile Velocity (km/s)	Initial Density (Mg/m^3)	Pressure (GPa)	Temperature Calculation Method	ε	T (°K)	σ ($W/sr\ m^3$)	$\sigma/\bar{N}_\lambda$
CaO2T	Cu/Cu	6.258 ±.055	3.3449 ±.0013	140.1 ±1.9	(a)	0.60	4075 ±156	5.8 $\times 10.^{11}$	0.25
					(b)	1.00	3749 ±178	7.8 $\times 10.^{11}$	0.34
CaO1T	Cu/Cu	7.102 ±.021	3.3422 ±.0012	171.0 ±1.2	(a)	1.09	5242 ±222	3.4 $\times 10.^{12}$	0.21
					(b)	1.00	5333 ±238	3.5 $\times 10.^{12}$	0.21
CaO3T	Ta/Cu	6.457 ±.027	3.3411 ±.0014	181.6 ±1.2	(a)	1.15	5899 ±195	4.2 $\times 10.^{12}$	0.14
					(b)	1.00	6083 ±225	4.5 $\times 10.^{12}$	0.15

(a): best fit with Planck function and variable ε

(b): best fit with Planck function and $\varepsilon \equiv 1$ (blackbody)

than method (b), as measured by the standard deviation. Shot CaO2T was the only experiment which led to a best fit with $\varepsilon<1$. If the emissivity were really 0.6, as determined by the fit, one would expect to see the time dependent behavior similar to that observed in forsterite by Ahrens *et al.* (1982) or anorthite glass at lower pressures (Boslough *et al.*, 1983), due to the increasing thickness of the shocked material with time, unless the shock front is opaque and has a finite reflectivity. Because this is not observed, it is reasonable to conclude that the emissivity is close to unity for all three experiments.

Equation of State

Shock temperatures determined by methods (a) and (b) are plotted in the P-T plane in Fig. 1-5, along with a theoretical calculation by the method of Ahrens *et al.* (1969), based on parameters of Jeanloz and Ahrens (1980), and a Dulong-Petit specific heat $C_v= 3R$. If the temperatures calculated by method (a) are believed, there is strong evidence for a phase transition at about 4000°K, with a transition energy, $E_{tr}\geq 0.5$ kJ/ g. We do not favor this interpretation, but include it for completeness.

The results of method (b) (blackbody temperatures) are preferred for reasons outlined above, and there is no evidence for a phase transition at or above 4000°K based on these temperatures. However, all three measured temperatures lie about 600°K below the theoretical curve of Jeanloz and Ahrens, indicating that E_{tr}, the energy of transition between the initial state and the metastable final phase at standard conditions, is actually larger than the value used in the calculations: 1.6 kJ/g.

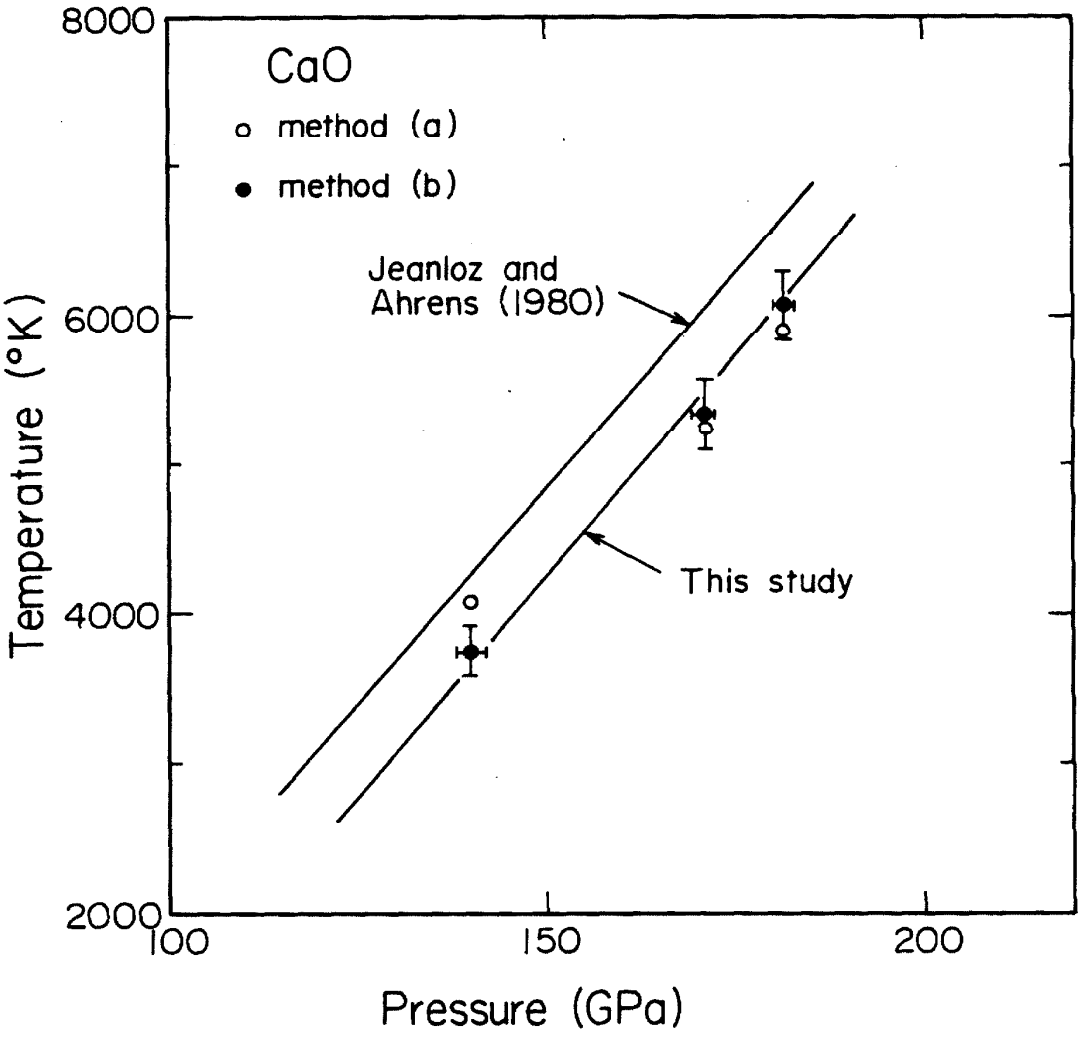

Fig. 1-5 Shock temperature data determined by method (a) ($\varepsilon \neq 1.0$) and method (b) (blackbody). Calculated Hugoniots based on Jeanloz and Ahrens (1980) and both low and high zero-pressure-density solutions of this paper.

One possible interpretation is a second phase transition below 140 GPa. This phase transition would have to have an $E_{tr} \approx 0.5$ kJ/g, unless E_{tr} for the B1 to B2 transition is significantly less than 1.6 kJ/g, which is unlikely. Such a small E_{tr} would probably not result from melting, which would be expected to have an E_{tr} of around 1.4 kJ/g, the latent heat of fusion at 1 atmosphere (Robie *et al.*, 1979).

If the B2 phase indeed exists on the Hugoniot to 182 GPa, a complete equation of state for that phase can be constructed from the present data. Rather than simply assuming the parameters determined by Jeanloz and Ahrens and finding the E_{tr} which provided the best agreement to the new temperature data, all the available data for the B2 phase were simultaneously fit. This included porous Hugoniot data (Marsh, 1980), and isothermal data (Mammone *et al.*, 1981). The inversion procedure was based on third order finite strain theory (Davies, 1973) and the Mie-Gruneisen approximation, with $\frac{\gamma}{V}$ assumed constant, where γ is the thermodynamic Gruneisen parameter $V\left(\frac{\partial P}{\partial E}\right)_V$. Despite the abundance of data, a wide range of values provided good conformity. Parameters for the two extreme models are given in Table 1-3, based on zero pressure densities of 3.8 and 4.0 g/cm^3.

Curves calculated with these parameters are plotted with the shock temperature data in Fig. 1-5, and with the isothermal and Hugoniot data in Fig. 1-1. Both the low and high density solutions give approximately the same curve in the P-T plane, but the high density equation of state requires a 0.2 kJ/g greater energy of transition. The slope of the theoretical curve is determined primarily by the specific heat. It is in good agreement with the data, indicating that the

Table 1-3

Fits to CaO B2 data

	Low density fit	High density fit
ρ (Mg/ m^3)	3.8	4.0
K_{os} (GPa)	121.0	190.0
dK_o/dP	5.2	4.0
E_{tr} (kJ/g)	2.1	2.3
γ_o	1.8	1.8

Dulong-Petit value (C_v =3R) is a good approximation for CaO, in contrast to anorthite (Boslough *et al.*, 1983) and quartz (Lyzenga *et al.*, 1983).

Conclusions

The first shock temperature data have been presented for CaO to 182 GPa. They can be fit well with theoretical shock temperature calculations for CaO in the B2 phase and allow a precise energy of transition (2.1 to 2.3 kJ/g at STP) to be determined for the B1-B2 phase transformation. This E_{tr} in turn provides further constraint for calculating the bulk modulus and its pressure derivative from Hugoniot data. A range of equations of state were determined in this manner. The equation of state with the lowest zero pressure density in the range does not differ greatly from that of Jeanloz and Ahrens (1980) but is better constrained. At lower mantle pressures, the present models predict densities of CaO to be lower than the lower mantle by up to 1.3%, and bulk moduli greater by 3 to 13%. Thus, depending on the bulk properties of the other components of lower mantle models, and the particular model used, CaO cannot be precluded as a major component of the lower mantle on the basis of its density and bulk modulus. However, because such a wide range of equations of state for the B2 phase are indistinguishable with the data, theoretical considerations may be necessary to choose the best equation of state.

Acknowledgments

We wish to thank D. Bakker, E. Jerbic, and the rest of the technical personnel at the Lawrence Livermore National Laboratory light-gas gun facility and standards laboratory. We appreciate discussions with G. Lyzenga, W. Nellis, and J. Trainor, and the facilities provided by W. Nellis at Livermore. M. Abraham provided CaO samples, and G. Rossman and his students at Caltech provided assistance in determining optical properties, for which we are grateful. We also appreciate the help of E. Gelle and others at the Caltech shock-wave laboratory in sample preparation. Support was provided by NSF EAR78 12942 at the California Institute of Technology, and by the Lawrence Livermore National Laboratory. This manuscript has been submitted to *J. Geophys. Res.* with co-authors Thomas J. Ahrens and Arthur C. Mitchell. Contribution 3931, Division of Geological and Planetary Sciences, California Institute of Technology.

References

Abraham, M.M., C.T. Butler, and Y. Chen, Growth of high-purity and doped alkaline earth oxides: I. MgO and CaO, *J. Chem. Phys.*, *55*, 3752-3756, 1971.

Ahrens, T.J., C.F. Peterson, and J.T. Rosenberg, Shock compression of feldspars, *J. Geophys. Res.*, *74*, 2727-2746, 1969.

Ahrens, T.J., G.A. Lyzenga, and A.C. Mitchell, Temperatures induced by shock waves in minerals: Applications to geophysics, in *High-Pressure Research in Geophysics*, edited by S. Akimoto and M.H. Manghnani, 579-594, Center for Academic Publications Japan, Tokyo, 1982.

Anderson, D.L. and R.S. Hart, An earth model based on free oscillations and body waves, *J. Geophys. Res.*, *81*, 1461-1475, 1976.

Boslough, M.B., S.M. Rigden, and T.J. Ahrens, Hugoniot equation of state of anorthite glass and lunar anorthosite, *Geophys. J. R. astr. Soc.*, submitted, 1983.

Chang, Z.P. and E.K. Graham, Elastic properties of oxides in the NaCl-structure, *J. Phys. Chem. Solids*, *38*, 1355-1362, 1977.

Davies, G.F., Quasi-harmonic finite strain equations of state of solids, *J. Phys. Chem. Solids*, *34*, 1417-1429, 1973.

Dziewonski, A.D. and D.L. Anderson, Preliminary reference earth model, *Phys. Earth Planet. Interiors*, *25*, 297-356, 1981.

Dziewonski, A.M., A.L. Hales, and E.R. Lapwood, Parametrically simple earth models consistent with geophysical data, *Phys. Earth Planet. Interiors*, *10*, 12-48, 1975.

Grossman, L., and J.W. Larimer, Early chemical history of the solar system, *Rev. Geophys. Space Phys.*, *12*, 71-101, 1974.

Jackson, J.D., *Classical Electrodynamics*, John Wiley & Sons, New York, 1975.

Jeanloz, R., T.J. Ahrens, H.K. Mao, and P.M. Bell, B1/B2 transition in CaO from shock-wave and diamond cell experiments, *Science*, *266*, 829-830, 1979.

Jeanloz, R., and T.J. Ahrens, Equations of state of FeO and CaO, *Geophys. J.R. astr. Soc.*, *62*, 505-528, 1980.

Liu, L.-G., A new high-pressure phase of $Ca_2Al_2SiO_7$ and implications for the earth's interior, *Earth Planet. Sci. Lett.*, *40*, 401-406, 1978.

Liu, L.-G., High-pressure phase transformations in the system $CaSiO_3$–Al_2O_3, *Earth Planet. Sci. Lett.*, *43*, 331-335, 1979.

Lyzenga, G.A., and T.J. Ahrens, A multi-wavelength optical pyrometer for shock compression experiments, *Rev. Sci. Instrum.*, *50*, 1421-1424, 1979.

Lyzenga, G.A., T.J. Ahrens, and A.C. Mitchell, Shock temperatures of SiO_2 and their geophysical implications, *J. Geophys. Res.*, *88*, 2431-2444, 1983.

Mammone, J.F., H.K. Mao, and P.M. Bell, Equations of state of CaO under static pressure conditions, *Geophys. Res. Lett.*, *8*, 140-142, 1981.

Marsh, S.P., *LASL Shock Hugoniot Data*, 680 pp. University of California Press, Berkeley, 1980.

McQueen, R.G., S.P. Marsh, J.W. Taylor, J.N. Fritz, and W.J. Carter, The equation of state of solids from shock wave studies, in *High-Velocity Impact Phenomena*, edited by R. Kinslow, pp. 293-417, Academic, New York, 1970.

Mitchell, A.C. and W.J. Nellis, Diagnostic system of the Lawrence Livermore National Laboratory two-stage light-gas gun, *Rev. Sci. Instrum.*, *52*, 347-359, 1981.

Perez-Albuerne, E.A. and H.G. Drickamer, Effect of high pressures on the compressibilities of seven crystals having the NaCl or CsCl structure, *J. Chem. Phys.*, *43*, 1381-1387, 1965.

Rice, M. H., R. G. McQueen, and J. M. Walsh, Compressibility of solids by strong shock waves, *Solid State Phys.*, *6*, 1-63, 1958.

Robie, R.A., B.S. Hemingway, and J.R. Fisher, *Thermodynamic Properties of Minerals and Related Substances at 298.15K and 1 Bar (10^5 Pascals) Pressure and at Higher Temperatures*, pp. 216-221, Government Printing Office, Washington, D.C., 1979.

Ross, J.E. and L.H. Aller, The chemical composition of the sun, *Science*, *191*, 1223-1229, 1976.

Turekian, K.K. and S.P. Clark, Jr., Inhomogeneous accretion model of the earth from the primitive solar nebula, *Earth Planet. Sci. Lett.*, *6*, 346-348, 1969.

Chapter 2

Shock Temperatures in Anorthite Glass

ABSTRACT

Temperatures of $CaAl_2Si_2O_8$ (anorthite glass) shocked to pressures between 48 and 117 GPa have been measured in the range from 2500 to 5600°K, using optical pyrometry techniques. The pressure dependence of the shock temperatures deviates significantly from predictions based on a single high-pressure phase. At least three phase transitions, at pressures of about 55, 85, and 100 GPa and with transition energies of about 0.5 kJ/g each (≈1.5 kJ/g total) are required to explain the shock-temperature data. The phase transition at 100 GPa can possibly be identified with the stishovite melting transition. Theoretical models of the time dependence of the thermal radiation from the shocked anorthite based on the geometry of the experiment and the absorptive properties of the shocked material give good agreement with observations, indicating that it is not necessary to invoke intrinsic time dependences to explain the data in many cases. Observed time dependences were used to calculate absorption coefficient of the shocked material of from 1 to >14 mm^{-1}; an increasing function of shock pressure. The assumption that the shocked material radiates as a blackbody is supported by the

theoretical model, and by the close agreement between measured and calculated blackbody spectral radiance as a function of wavelength.

Introduction

Because of the cosmochemical abundance of Ca and Al, and the refractory nature of calcium-aluminum silicates such as anorthite, their high pressure polymorphs are important to consider in any model of the earth's mantle. Models for the earth's composition based on chondritic abundances predict atomic abundance ratios of $\frac{Ca}{Si} \approx 0.05$ and $\frac{Al}{Si} \approx 0.07$ (Ross & Aller, 1976). It is possible however, that the lower mantle is significantly enriched relative to the whole earth in calcium-aluminum silicates, because these are among the first phases to condense from the solar nebula (Grossman & Larimer, 1974) and accrete onto the earth, in inhomogeneous accretion models (Turekian & Clark, 1969). Moreover, the construction of equations of state for anorthosite are key ingredients in carrying out cratering calculations for impacts on the crusts of terrestrial planets (Ahrens & O'Keefe, 1977, 1983), and in determining quantities of melting and vaporization resulting from such an impact (Boslough & Ahrens, 1983).

In previous work on anorthite, a high pressure equation of state to pressures greater than 120 GPa has been constructed by Jeanloz & Ahrens (1980) based on Hugoniot data only. This equation of state is incomplete in that the thermal behavior of the shocked material was inferred from pressure-density states only. The parameter which is most sensitive to thermal properties and

energetics of phase transitions, namely the temperature, was not measured.

Past work (Kormer *et al.*, 1965, Ahrens *et al.*, 1982, Lyzenga *et al.*, 1983, Boslough *et al.*, 1983a) has demonstrated the usefulness of shock-temperature data in constraining the high-pressure-high-temperature properties of materials, and in defining phase transitions. For example, the stishovite melting curve was determined from shock-temperature data on α-quartz and fused quartz. This phase transition is readily apparent from the temperature data, but is not at all obvious from Hugoniot data in the pressure-density plane (Lyzenga *et al.*, 1983). It is reasonable to expect similar results for other materials. The purpose of the present study was to measure temperatures of shocked anorthite glass using the optical pyrometry technique, and determine the high-pressure thermal behavior of $CaAl_2Si_2O_8$.

Experimental

Amorphous $CaAl_2Si_2O_8$ samples, with measured Archimedean initial densities of 2.69 Mg/m^3 were used in these shock-temperature experiments. The samples, obtained from Corning Glass Co. (Corning, N.Y.), were clear and homogeneous, with a composition described by $An_{99.5}\ Ab_{0.4}\ Or_{0.1}$ – essentially the composition of pure anorthite. A microprobe analysis of a representative sample is given in terms of oxides in Table 2-1. The transmittance of a 3mm thick, polished sample of the glass over the wavelength range of interest is shown in Fig. 2-1, measured with a Cary Model 17 spectrophotometer.

Shock experiments were carried out on two-stage light-gas guns at the California Institute of Technology and Lawrence Livermore National Laboratory. Copper and tantalum projectiles were accelerated to velocities between 3.7 and

Table 2-1

Electron microprobe analysis of anorthite glass (Corning)

Oxide	Wt.%
Na_2O	0.05
MgO	0.00
Al_2O_3	36.36
SiO_2	43.48
K_2O	0.01
CaO	20.73
TiO_2	0.06
FeO	0.04
BaO	0.03
Total	100.76

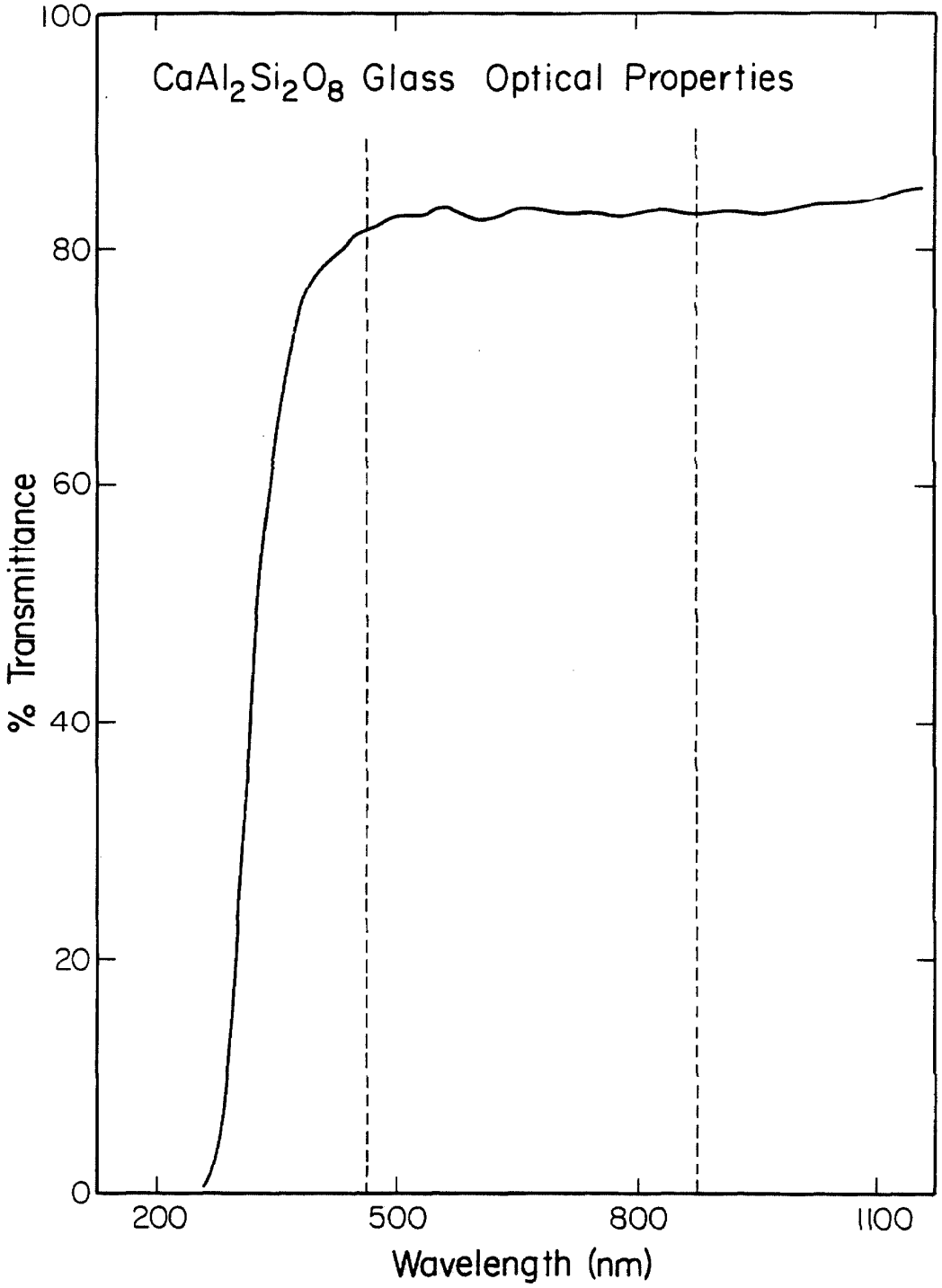

Fig. 2-1. Transmittance spectrum of a representative sample of $CaAl_2Si_2O_8$ glass (sample An7T), measured by Cary 17 spectrophotometer. Transmittance shows negligible wavelength dependence between wavelength limits of optical pyrometers (dashed lines).

5.7 km/s. Projectile velocities were determined using flash X-radiography, as described elsewhere (Jeanloz & Ahrens, 1977; Mitchell & Nellis, 1981). Shock pressures were determined by the method of impedance matching (Rice *et al.*, 1958) and using the standard equation of state of McQueen *et al.* (1970) for tantalum and copper, and the Hugoniot of Boslough *et al.* (1983b), for the anorthite glass.

Temperatures were determined by measuring the intensity of thermally radiated light at several wavelengths in the visible and near infrared wavelengths. The thermal radiation was filtered by interference filters and focused onto silicon photodiodes. The resulting electrical signals were recorded by an array of oscilloscopes with Polaroid cameras. The recorded time-resolved voltages are directly proportional to the spectral radiances of the thermal radiation. Calibration of the pyrometer systems was carried out using light sources with known spectral radiances in the wavelength range in which measurements were made. The two optical pyrometers used in this study are described in detail by Lyzenga & Ahrens (1979) and in Appendix I and II.

Results

Eight shock temperature experiments were conducted on anorthite glass; three using a 10 nm bandwidth six-channel optical pyrometer at Lawrence Livermore National Laboratory (Lyzenga & Ahrens, 1979), and five using a 40 nm bandwidth four-channel optical pyrometer at the California Institute of Technology (Appendix I). Representative data are shown in Figs. 2-2 and 2-3.

Three general types of time-dependence were observed. In shots An6T, An5T, and An3T--the three experiments below 70 GPa--the sharp increase in

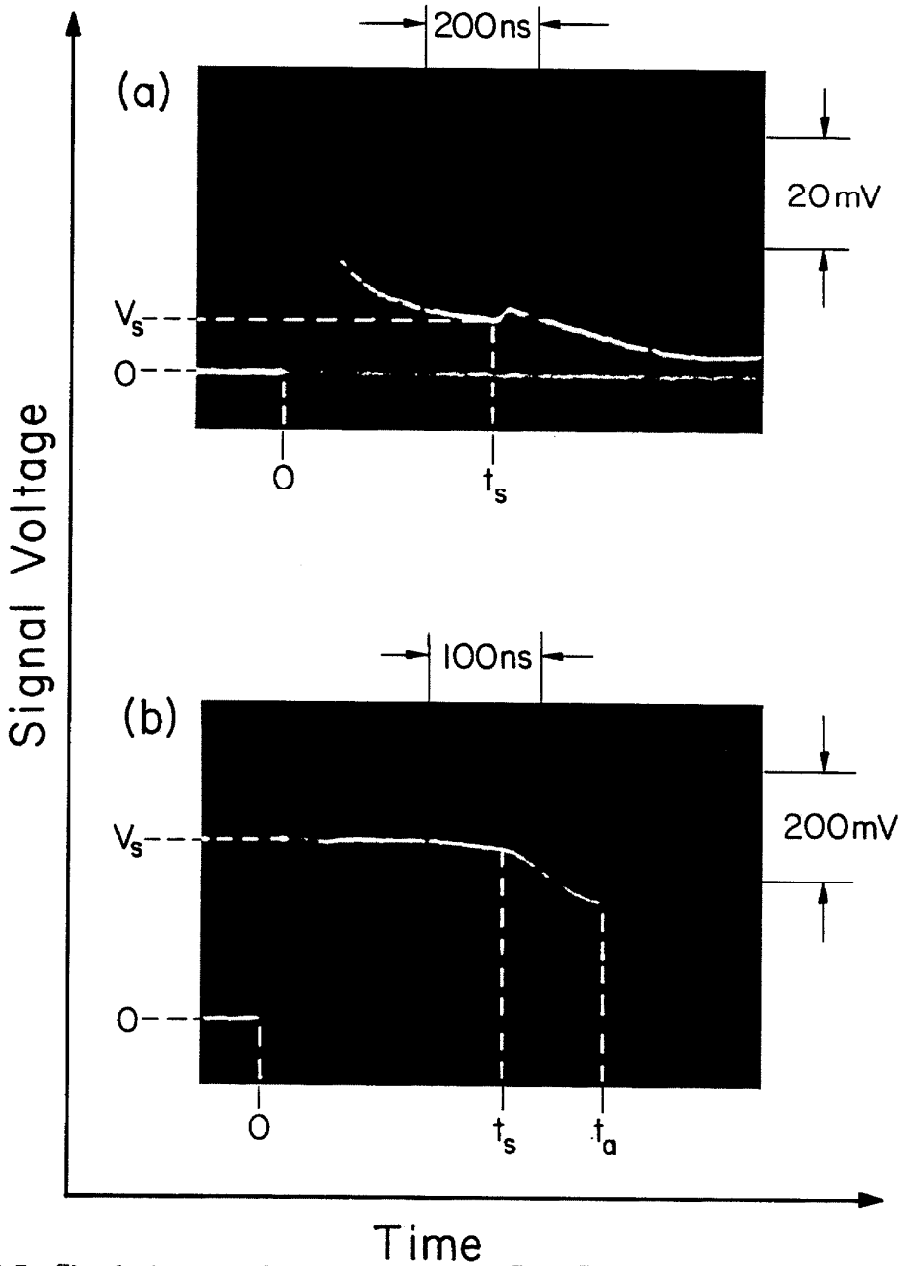

Fig. 2-2 Shock temperature records for $CaAl_2Si_2O_8$ glass. Signal voltage is directly proportional to the intensity of the radiated light at the wavelength of the filter. (a) An5T: P = 55 GPa, T = 2700°K, λ = 750nm. Time dependence is due to combination of effects: Cooling of interface and thickening of radiating (shocked) layer. (b) An10T: P = 117 GPa, T = 5600°K, λ = 600nm. Initially constant signal due to high opacity of shocked layer. Decrease in intensity just before free surface arrival due to decay of shock by edge rarefaction.

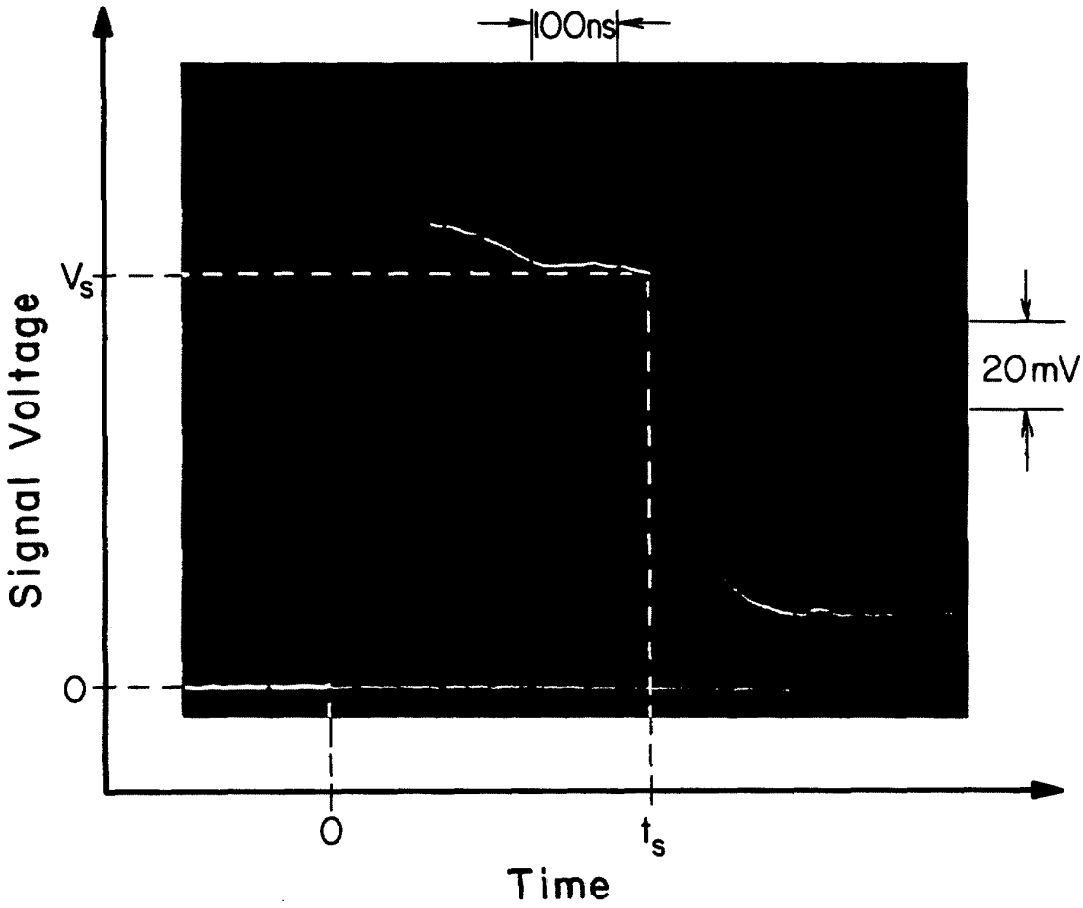

Fig. 2-3. Shock temperature record for shot An9T: P=85 GPa, T=4000°K, λ=750nm. Time dependence can only be explained by unsteady shock. Signal voltage is directly proportional to the intensity of the radiated light at 750nm.

intensity corresponding to the entrance of the shock wave into the sample is followed by an exponential decay to an approximately constant value (Fig. 2-2a). In shots An2T, An7T, An1T, and An10T--four experiments above 89 GPa--the light intensity remains constant to within about 10% until the shock wave reaches the free surface or is overtaken by an edge rarefaction (Fig. 2-2b). Shot An9T--to about 85 GPa--shows an anomalous behavior, in which the intensity decreases at a nonuniform rate during shot transit (Fig. 2-3).

There are three causes which could account for time dependence in the emitted light: temperature dependence, emissivity dependences, or time dependence of the absorption or scattering of an intervening layer. All three of these causes are invoked to explain the observed time dependences. It is important to note that the observed light is not necessarily radiated from only the shock front unless the shocked material is perfectly opaque. In general, a material that is initially semi-transparent, with initial linear absorption coefficient a_u is shocked to a state with linear absorption coefficient a_s and temperature T. The absorbance of the unshocked layer is $A_u = e^{-a_u d_u}$, and the shocked layer is $A_s = e^{-a_s d_s}$, where d_n and d_s are the thicknesses of unshocked and shocked layers, respectively. According to Kirchoff's radiation law for a non-reflector (Jenkins & White, 1976) the emissivity of a layer is equal to its absorbance. If the sample thickness is d, the shock velocity is U_s, and graybody light (with a Planckian wavelength distribution and an emissivity less than unity) is radiated only from the shocked layer at constant temperature T, the time dependence will be

$$I_s(t) = f_\lambda(T)\left[1-e^{-a_s u_s t}\right]e^{-a_u(d - U_s t)}, \qquad (2\text{-}1)$$

where $f_\lambda(T)$ is the Planck distribution function. In the case of anorthite glass, the initial state is essentially transparent (Fig. 2-1), so $a_u=0$ and this becomes:

$$I_s(t) = f_\lambda(T)\left[1 - e^{-a_s U_s t}\right]. \tag{2-2}$$

It is also necessary to consider the effect of light generated at the interface between the driver and sample material, due to the non-ideality of the surfaces, which, despite their optical quality, have imperfections which leave a gap on the order of 1μm wide as determined by counting visible fringes (Newton rings) with an optical flat.

The temperature at the interface due to passage of the shock wave is higher than the shock temperature of either boundary material, due to multiple reverberation (Urtiew & Grover, 1974) and shock heating of any gas trapped in the gap. The temperature decay as a function of time at the interface can be modeled simply as a Fourier diffusion boundary value problem in one dimension. The metallic driver is considered to be a thermally conducting half-space with initial temperature T_d, the shock temperature of the driver, and thermal diffusivity κ. The sample is modelled as a thermal insulator. This problem is solved by Carslaw & Jaeger (1959, p.51). The solution is

$$T(x,t) = T_d + \frac{Q}{2\rho C_V \sqrt{\pi \kappa t}} e^{-x^2/4\kappa t}, \tag{2-3}$$

where t is the time after impact, x is the distance of a point in the driver from the interface, Q is the quantity of heat per unit area (unknown) deposited at the interface by the closing of the gap, and ρ and C_V are the density and the specific heat at constant volume of the driver material, respectively. The time

dependence of the interface temperature is

$$T_i(t) = T(0,t) = T_d + Ct^{-1/2}. \tag{2-4}$$

If the interface radiates as a blackbody, the observed light intensity from it (with attenuation due to the growing shocked layer) is

$$I_i(t) = f_\lambda(T_d + Ct^{-1/2})e^{-a_s U_s t}. \tag{2-5}$$

The total light intensity observed is due to both sources (Eqns. 2-1 and 2-5)

$$I(t) = f_\lambda(T)\left[1-e^{-a_s U_s t}\right] + f_\lambda(T_d+Ct^{-1/2})e^{-a_s U_s t}. \tag{2-6}$$

One can easily see that for $t \gg \frac{1}{a_s U_s}$, the shocked layer is effectively an opaque blackbody, and there is no time dependence in the observed intensity. For sufficiently large a_s, this occurs at t smaller than the rise time of the pyrometer photodiode and no time dependent behavior is observed at all. This is observed in shots An1T, An7T, and An10T (Fig. 2-2b).

For smaller a_s, the time dependence is depicted schematically in Fig. 2-4, and is illustrated by the spectral radiance observed in shot An3T in Fig. 2-5. The contribution due to the shocked sample increases from zero, when the shock wave enters the sample, asymptotically to $f_\lambda(T)$, the intensity of a blackbody at temperature T, with a time constant $\tau = \frac{1}{a_s U_s}$. The interface contribution decreases from infinity (because of the idealized assumption that all the heat is deposited at the two-dimensional interface) to zero, with a time constant $\tau < \frac{1}{a_s U_s}$, because the source is also decaying with time. The observed light

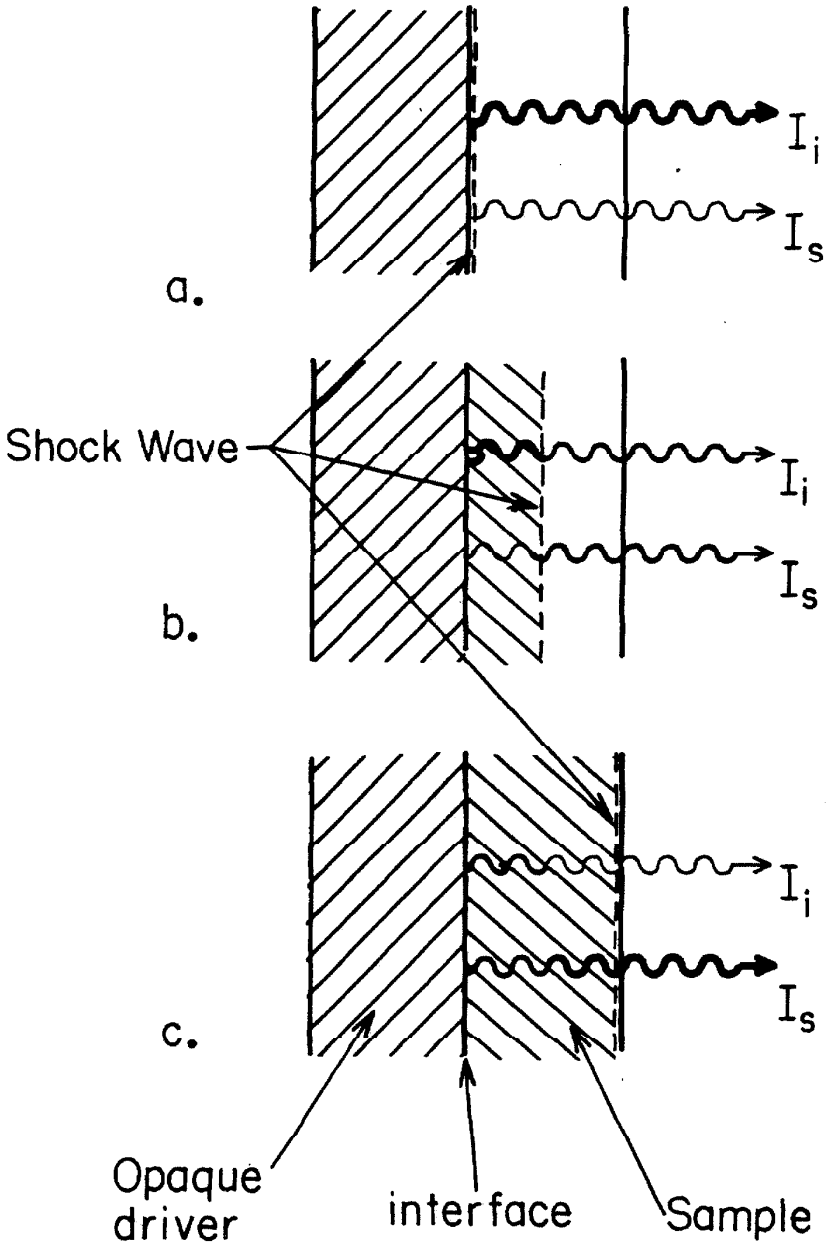

Fig. 2-4 Schematic of shock temperature experiment. Measured light intensity is sum of light from interface (I_i) and shocked sample layer (I_s). (a) Just after shock enters sample, light from hot interface dominates. and is not attenuated significantly by thin shocked layer. (b) I_i has decreased due to cooling of interface and thickening of attenuating layer. I_s has increased due to thickening of emitting layer. (c) Interface has cooled and is further blocked by thick shocked layer. I_s, the light intensity characteristic of the shock temperature now dominates.

TJA83108SFD

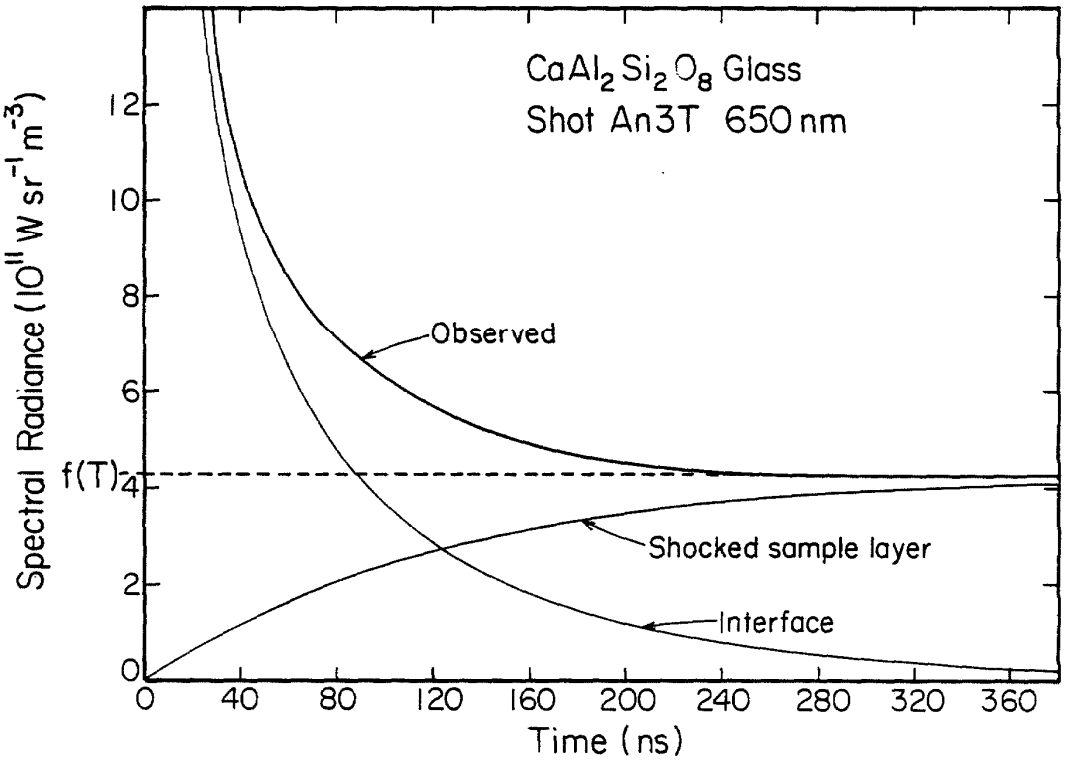

Fig. 2-5. Measured spectral radiance from shot An3T (P = 66 GPa, T = 3000°K) at λ = 650nm. The measured time dependence can be fit by a function of the form: $A(1-e^{-\alpha t}) + Bt^{-1/2} e^{-\alpha t}$, an approximation of equation (2-6), with $A = 4.3\times10^{11}$ $WSr^{-1}m^{-3}$, $B = 8.2\times10^{12}$ $WSr^{-1}m^{-3}$, and $\alpha = 8.0\times10^{-3}ns^{-1}$.

TJA83109SFD

intensity is the sum which decreases asymptotically to $f_\lambda(T)$, with an effective decay time bounded above by $\frac{1}{a_s U_s}$. This is the time dependence observed in shots An2T, An3T, An5T, and An6T (Fig. 2-2a).

One experiment, An9T, exhibits time-dependent behavior not accounted for by this simple model. The intensity of the emitted light decreases in steps as the shock wave passes through the sample, indicating that the time-dependence is in the shock front itself, as a fluctuation in temperature, absorption coefficient, or both. This is similar to behavior observed in fused quartz shocked to the stishovite-liquid mixed phase region by Lyzenga *et al.* (1983), which they interpret as a possible rate dependent behavior due to metastability near the phase transition pressure.

In the simple model developed above (Eq. 2-6), the linear absorption coefficient a_s for the shocked anorthite can be constrained by measuring the effective decay times from the oscilloscope records for the shots whose results agree with the model. The upper bound for a_s is $a_{smax} = \frac{1}{\tau U_s}$. These values are tabulated in Table 2-2. The bound on a_s is seen to be an increasing function of shock pressure.

$CaAl_2Si_2O_8$ Shock Temperatures

Temperatures were calculated from the spectral radiance data by fitting them to a Planck function, as outlined in Appendix III. This was done in two ways for each experiment. First, a least squares fit is carried out in which both the temperature T and emissivity ε are independent variables. The temperatures and emissivities determined in this manner are given in Table 2-3, along with the

Table 2-2

Bounds on absorptivity of shocked anorthite glass

Shot	τ (μs)	U_s (mm/μs)	a_{smax} (mm^{-1})	Pressure (GPa)
An6T	0.15	6.5	1.0	50.3
An5T	0.10	7.0	1.4	57.0
An3T	0.08	7.7	1.6	68.2
An2T	0.01	8.6	12	90.4
Others	<0.007	<10.	>14	>93.1

$$a_{smax} = \frac{1}{\tau U_s}$$

Table 2-3

Anorthite Glass Shock Temperature Data

Shot	Flyer/ Driver Material	Projectile Velocity (km/sec)	Initial Density (Mg/m^3)	Pressure (GPa)	Temperature Calculation Method	ε	T (°K)	σ ($W/sr\ m^3$)	σ/N_λ
An6T	Cu/Cu	3.72 ±.10	2.6908 ±.0010	48.3 ±2.2	(a)	1.76	2323 ±5	0.2 $\times 10^{10}$	0.02
					(b)	1.00	2481 ±37	1.4 $\times 10^{10}$	0.13
An5T	Cu/Cu	4.038 ±.002	2.6909 ±.0013	55.0 ±1.1	(a)	0.98	2723 ±37	2.7 $\times 10^{10}$	0.12
					(b)	1.00	2714 ±39	2.8 $\times 10^{10}$	0.12
An3T	Cu/Cu	4.536 ±.006	2.6900 ±.0010	66.4 ±1.2	(a)	1.05	2997 ±104	1.5 $\times 10^{11}$	0.30
					(b)	1.00	3017 ±105	1.5 $\times 10^{11}$	0.30
An9T	Cu/Cu	5.255 ±.003	2.6953 ±.0012	84.5 ±1.3	(a)	1.01	4002 ±21	1.2 $\times 10^{11}$	0.03
					(b)	1.00	4010 ±22	1.3 $\times 10^{11}$	0.04
An2T	Cu/Cu	5.455 ±.010	2.6899 ±.0011	89.9 ±1.3	(a)	1.34	3802 ±6	0.4 $\times 10^{11}$	0.01
					(b)	1.00	3985 ±71	4.0 $\times 10^{11}$	0.12
An7T	Cu/Cu	5.563 ±.006	2.6927 ±.0011	92.9 ±1.2	(c)	1.00	4564 ±104		
An1T	Ta/Ta	5.678 ±.010	2.6893 ±.0011	111.5 ±1.3	(a)	1.24	4904 ±76	1.1 $\times 10^{12}$	0.08
					(b)	1.00	5110 ±122	1.6 $\times 10^{12}$	0.12
An10T	Ta/Cu	5.562 ±.003	2.6944 ±.0012	116.8 ±1.1	(a)	0.91	5741 ±218	3.5 $\times 10^{12}$	0.19
					(b)	1.00	5625 ±214	3.6 $\times 10^{12}$	0.20

(a): best fit with Planck function and variable ε

(b): best fit with Planck function and $\varepsilon \equiv 1$ (blackbody)

(c): brightness temperature

standard deviation σ and the mean fractional deviation $\sigma / \overline{N}_\lambda$ of the fit. There appears to be no correlation between the shock pressure and the emissivity which gives the best fit, and in the majority of cases the best fitting emissivity is greater than unity--an unphysical situation.

Because of this discrepancy, and the fact that the model developed in the previous section implies that the observed intensity corresponds to a blackbody on the asymptote, temperatures were also calculated assuming $\varepsilon = 1.0$, and conducting a standard single variable least squares fit for T.

In four of the eight anorthite shots, the best fitting emissivities are within 10% of unity, and the goodness of the fits, as determined by the standard deviations are not significantly reduced by requiring that $\varepsilon = 1.0$. In three shots, the best fitting emissivities are significantly greater than unity. Two of these shots, An2T and An6T, have extremely good fits, with mean fractional standard deviations of .01 and .02, respectively. However, the emissivities which give rise to these fits are 1.34 and 1.76, respectively; unphysical values which imply that the quality of the fits is fortuitous. When the inversion is carried out with an emissivity of unity for these three shots, however, the qualities of the fits are still comparable to those for the other experiments.

In one shot, (An7T), the spectral radiance was obtained at only one wavelength. The shock temperature of this shot was assumed to be the brightness temperature. This assumption is based on the close agreement between the observed spectral radiances and blackbody distributions in the other seven experiments. The temperature error for this shot was taken from the estimated error in the measured spectral radiance.

In the other seven shots, the temperature errors were determined systematically by the equation

$$\Delta T = \frac{\sigma_N}{f_T\,(T,\lambda = 600\text{nm})}, \tag{2-7}$$

where σ_N is the standard deviation in spectral radiance, and $f_T(T,\lambda)$ the partial derivative of the Planck distribution function with respect to temperature. The partial derivative was evaluated at a wavelength of 600 nm, because this is near the middle of the widest wavelength range used.

The intensities used in the temperature calculations were taken from the oscilloscope records as indicated in Figs. 2-2 and 2-3. According to the simple model, the intensity of light most representative of thermal radiation from the shocked region of the sample is just before the shock wave arrives at the free surface. In all but one case, that is where the oscillograms were read. In the other case, shot An9T the shock wave begins to decay before it approaches the free surface, apparently due to an edge rarefaction. The intensity was taken from this set of shot records just prior to the beginning of the decay of the shock wave. The spectral radiances determined in this manner are tabulated in Appendix III, along with plots which show the measured spectral radiances and those calculated for the blackbody temperatures which give the best fits. The results of shot An9T are illustrated in Fig. 2-6.

Temperatures determined by both of these methods, along with their respective emissivities, standard deviations in spectral radiance and fractional standard deviations are summarized in Table 2-3. The associated pressures are determined from the measured projectile velocity, and impedance matching

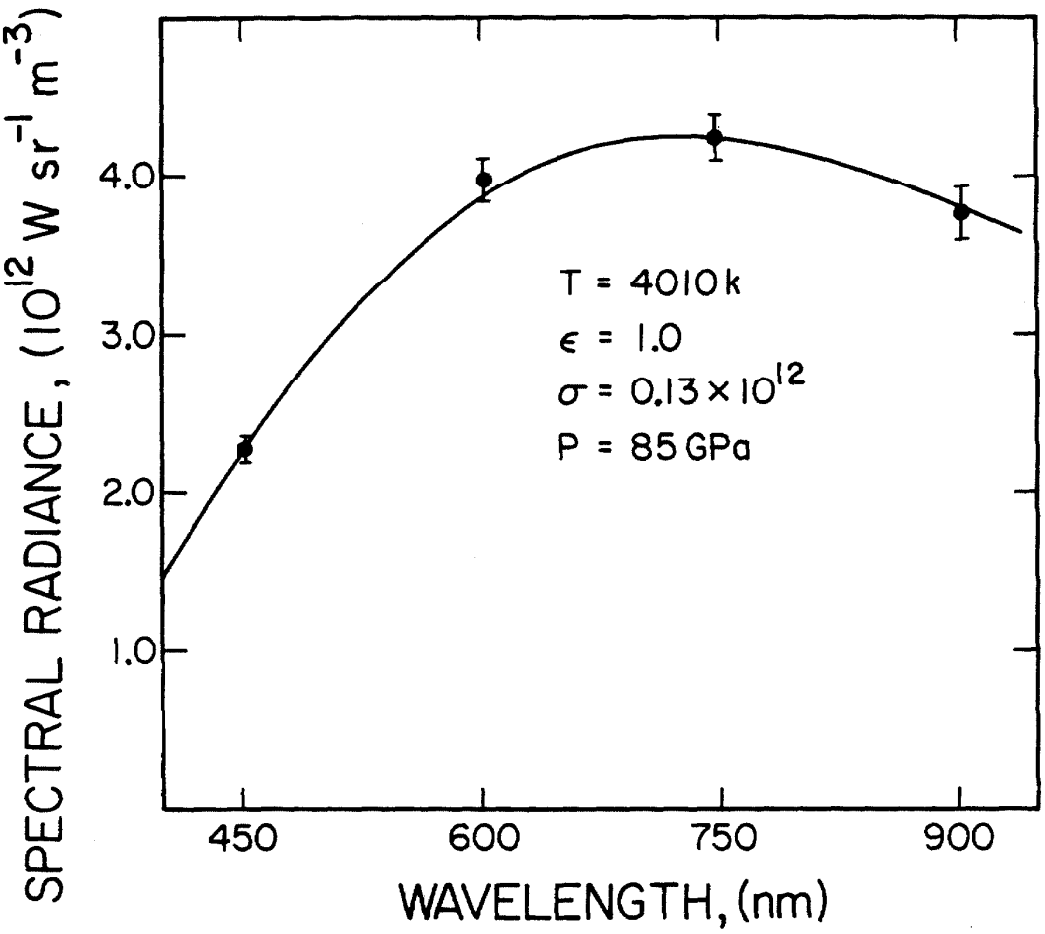

Fig. 2-6. Spectral radiance measured in shot An9T at four wavelengths. Best fitting blackbody curve is plotted.

TJA83089SFD

with a fit to the U_s–u_p data obtained in the Hugoniot experiments on anorthite glass (Boslough *et al.*, 1983). These impedance-match determined pressures are the preferred values to use when modelling the pressure-temperature Hugoniot, despite the fact that pressures were determined more directly for each shot by measuring shock-transit times. In the more direct pressure determination, projectile and shock velocity must both be measured. The precision by which the shock velocity can be measured is not as high as that of the projectile velocity measurement, and larger random errors can be introduced. In the impedance-match method, only the projectile velocity is used, which can be measured to better than ±0.2%, and a curve which is determined by a least-squares fit to the direct pressure measurements. This in effect smooths out the random errors.

Discussion

The measured shock temperatures in anorthite glass are plotted as a function of Hugoniot pressure in Fig. 2-7, along with pressure-temperature Hugoniot calculations based on several models. These models are the Jeanloz & Ahrens (1980) equation of state with a Dulong-Petit specific heat (C_V = 3R), the same equation of state with variable specific heat, and a model in which several phase transitions occur. The latter two models can provide reasonable fits to the data. The method of Ahrens *et al.* (1969) was used to calculate shock temperatures in all cases.

The Jeanloz & Ahrens (1980) equation of state considers all states above 30 GPa on the Hugoniot of anorthite crystal to be a single high pressure phase, as found by McQueen *et al.* (1967), and fits the Hugoniot data with a third order Eulerian finite strain (Burch-Murnaghan) isentrope (Davies, 1973). The

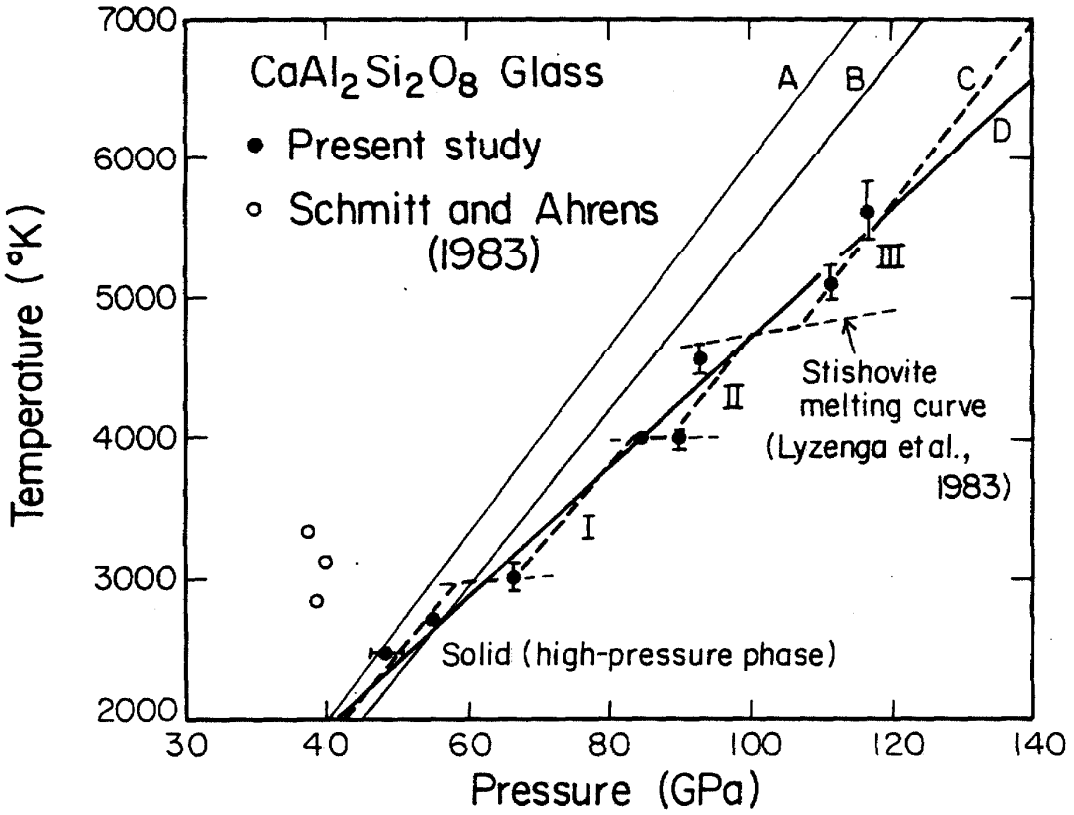

Fig. 2-7. Measured shock temperatures of $CaAl_2Si_2O_8$ assuming $\varepsilon = 1.0$, and four calculated pressure-temperature Hugoniots. (A) Mixed oxide model of Boslough et al. (1983). (B) Jeanloz and Ahrens (1980). (C) This study, assuming three phase transitions to high-pressure phase regimes denoted by I, II, and III, and $C_V = 3R$. (D) This study, assuming no phase transitions and $C_V = A + BT$. The lower two dashed lines are hypothetical phase transitions. The upper one is the stishovite melting curve (Lyzenga et al., 1983). Three shock temperature data by Schmitt and Ahrens (1983) are included, which exhibit heterogeneous hot spot (graybody) behavior.

TJA83119SFD

Gruneisen parameter was calculated by the pressure offset of the porous Hugoniot. The transition energy between single crystal anorthite and the metastable high pressure phase at standard conditions (E_{tr}) in this equation of state is .72 MJ/kg. This corresponds to an E_{tr} of .46 MJ/kg for anorthite glass, with the .26 MJ/kg energy difference between anorthite glass and crystal is accounted for (Robie *et al.*, 1978). Jeanloz & Ahrens considered anorthite above 2000°K to be a Debye solid in the classical limit--anorthite having a Debye temperature of 1000°K--and used the Dulong-Petit specific heat. This calculation gives reasonable agreement to the measured points below 60 GPa, but overestimates the shock temperature at higher pressure by as much as 1000°K. Clearly, the slope described by the data is less steep than the calculated slope.

In calculating shock temperatures by the method of Ahrens *et al.* (1969), the only way the theoretical T-P slope can change is to have a pressure or temperature-dependent C_V and/or phase transitions. There is ample theoretical and experimental evidence for a temperature dependent C_V in this temperature range, in departure from the Debye model of solids. A specific heat of the form

$$C_V = A + BT \qquad (2\text{-}8)$$

is equivalent to that of Wallace (1972) for NaCl, where A=3R and $B = \Gamma_2 - 2A_2$. Here, Γ_2 is the electronic contribution and A_2 is the first order anharmonic lattice contribution. The same form has been shown by Lyzenga *et al.* (1983) to describe shock temperature dependence on pressure for solid and liquid stishovite.

The coefficients for the best fit to the anorthite data are A = 0.92 kJ/kg°K and $B = 9.3\times10^{-5}$ kJ/kg°K^2. These coefficients are comparable to those

determined by Lyzenga *et al.* (1983) for solid and liquid stishovite, which has approximately the same mean atomic weight per atom as anorthite, with mean values of A = .86 kJ/ kg°K and B = 1.17×10^{-4} kJ/kg°K^2. B is in fact smaller for all the anorthite data taken together than for the single phases of the SiO_2 data, which indicates less temperature dependence for C_V overall.

It is probably unreasonable to expect that the anorthite undergoes no phase transition along this region of its Hugoniot, however, when one considers the complexity of its phase diagram at lower pressures, below 30 GPa (Liu, 1978), and when the behavior of simpler silicates such as SiO_2 in the same pressure range (Lyzenga *et al.*, 1983) is considered. Anorthite disproportionates to grossular, kyanite, and quartz at pressures from 3 to 15 GPa (Goldsmith, 1980; Boyd & England, 1961) and at 15 GPa the quartz transforms to stishovite along its Hugoniot (McQueen *et al.* 1963). Phase changes in grossular have been observed above 25 GPa (Liu, 1979). Hugoniot data indicate a mixed phase region in anorthite form 10 to 33 GPa (Jeanloz & Ahrens, 1980). Jeanloz & Ahrens give four candidate high-pressure phases above 33 GPa: $CaAl_2Si_2O_8$ (hollandite), CaO (B2 structure) + Al_2O_3 (corundum) + $2SiO_2$ (stishovite)–(mixed oxide assemblage), $CaAl_2O_4$ (calcium ferrite structure) + SiO_2 (stishovite), and $Ca_2Al_2SiO_7$ (sodium titanate structure) + Al_2O_3 (corundum) + $3SiO_2$ (stishovite). It is not unlikely, however, that phase transitions occur between these candidate phases, or others, above 33 GPa, or that further disproportionations or polymorphic transitions occur in the components of the candidate assemblages. Melting is also expected to occur in this shock-pressure range.

With each phase change is associated an energy of transition, which can be expressed in terms of ΔE_{tr}, the energy difference between the metastable phases

at standard conditions. The measured temperature for anorthite shocked into a mixed phase region will, if in equilibrium, lie on the coexistence curve. For anorthite shocked into a single phase regime, the measured temperature will lie $\frac{\Delta E_{tr}}{C_V}$ below the calculated metastable temperature of the lower phases. The slopes of the single-phase segments of the Hugoniot depend on C_V.

For constant $C_V = 3R$, at least three phase transitions (to assemblages indicated as I, II, and III in Fig. 2-7) are required to give a good fit to the data. If stishovite is a component of assemblage II, the highest transition--at about 4800°K--may correspond to the stishovite melting coexistence curve determined by Lyzenga *et al.* (1983) who found ΔE_{tr} for the stishovite to liquid transition to be about 1.6 MJ/kg. The transition at 4800° in anorthite gives a temperature difference of about 450° between the phases, which leads to $\Delta E_{tr} \approx .5$MJ/kg. The mass fraction of SiO_2 in $CaAl_2Si_2O_8$ is about .36, so if this phase transition is melting of SiO_2 only, this ΔE_{tr} corresponds to 1.4 MJ/kg in the SiO_2, which compares well with the value of Lyzenga *et al.* (1983).

Conclusions

When shock-temperature data are included in the description of the high-pressure phase assemblages in the system $CaAl_2Si_2O_8$, it is too complicated to be described by a single high pressure phase equation of state such as Jeanloz & Ahrens (1980). Although the shock temperature data can be roughly approximated assuming a single phase and choosing a temperature dependent model for C_V, the scatter of data around the best such single-phase curve in the pressure-temperature plane is still significantly greater than the estimated

errors in the temperature measurements. It is more reasonable to interpret the shock-temperature data by assuming that a series of phase transitions continue to occur along the Hugoniot. The data are consistent with three phase transitions--at about 55, 85, and 100 GPa—each with a transition energy of about 0.5 MJ/kg. The exact transition energies and pressures are not, however, well constrained by the data. The most realistic model would include both a temperature-dependent C_V and phase transitions. It is also possible that when melting does occur, it does so incongruently, with a compositional difference between the melt and solid. Such a transition must be treated in the context of a multi-component system, in contrast to the stishovite melting transition, for which SiO_2 can be treated as a single-component system. A possible consequence of incongruent melting would be a spreading of the mixed phase region out over a larger pressure range, and a resulting shallow slope for the Hugoniot in the pressure-temperature plane.

Success of modelling the time-dependence of the measured spectral radiances demonstrates the potential usefulness of the optical pyrometry method in studying optical properties of shocked material, in addition to measuring shock temperatures. By taking advantage of this fact the decay times of emitted light can be used to determine the absorption coefficient of the material behind the shock front, as in the case of anorthite glass, for which the absorption coefficient increases from 1 to >14 mm^{-1} as a function of shock-pressure (Table 2-2). Future experiments can be designed to determine absorption coefficient as a function of shock-pressure, and the shock state can be further characterized in this way.

Acknowledgments

We are indebted to E. Gelle, W. Ginn, M. Long, and C. Manning of the Caltech shock wave laboratory, and to D. Bakker, E. Jerbic and others at the Livermore facility for their expert technical help. We are grateful for the helpful discussions with G. Lyzenga, W. Nellis, and J. Trainor and to W. Nellis for providing facilities at Livermore. We wish to thank G. Rossman and his students at Caltech, who assisted in the determination of optical properties. Support was provided by NSF EAR78 12942 and NASA NGL-05-002-105 at the California Institute of Technology, and by the Lawrence Livermore National Laboratory. This manuscript has been submitted to *Geophys. J. R. astr. Soc.* with co-authors Thomas J. Ahrens and Arthur C. Mitchell. Contribution 3932, Division of Geological and Planetary Sciences, California Institute of Technology.

References

Ahrens, T.J., Peterson, C.F. & Rosenberg, J. T., 1969. Shock comperssion of feldspars, *J. Geophys. Res.*, **74**, 2727-2746.

Ahrens, T.J. & O'Keefe, J.D., 1977. Equations of state and impact-induced shock-wave attenuation on the moon. *Impact and Explosion Cratering*, pp. 639-656, eds Roddy, D.J., Peppin, R.O. & Merrill, R.B., Pergamon, New York.

Ahrens, T.J., Lyzenga, G.A. & Mitchell A.C., 1982. Temperatures induced by shock waves in minerals: applications to geophysics, in *High-Pressure Research in Geophysics*, pp. 579-594, eds Akimoto, S. & Manghnani, M.H., Center for Academic Publications Japan, Tokyo.

Ahrens, T.J. & O'Keefe, J.D., 1983. Impact of an asteroid or comet in the ocean and extinction of terrestrial life, *J. geophys. Res.*, **88**, A799-A806.

Boslough, M.B. & Ahrens, T.J., 1983. Shock-melting and vaporization of anorthosite and implications for an impact-origin of the moon, *Lunar and Planetary Science XIV*, pp. 63-64, Lunar and Planetary Institute, Houston.

Boslough, M.B., Ahrens, T.J. & Mitchell, A.C., 1983a. Shock temperatures in CaO, *J. geophys. Res.*, submitted.

Boslough, M.B., Rigden, S.M. & Ahrens, T.J., 1983b. Hugoniot equation of state of anorthite glass and lunar anorthosite, *Geophys. J. R. astr. Soc.*, submitted.

Boyd, F.R. & England, J.L., 1961. Melting of silicates at high pressures, *Carnegie Inst. Wash. Year Book*, **60**, 113-125.

Carslaw, H.S. & Jaeger, J.C., 1959. *Heat Conduction in Solids*, Oxford

University Press, Oxford, 510 pp.

Davies, G.F., 1973. Quasi-harmonic finite strain equations of state of solids, *J. Phys. Chem. Solids*, **34**, 1417-1429.

Goldsmith, J.R., 1980. The melting and breakdown reactions of anorthite at high pressures and temperatures, *American Mineralogist*, **65**, 272-284.

Grossman, L. & Larimer, J.W., 1974. Early chemical history of the solar system, *Rev. Geophys. Space Phys.* **12**, 71-101.

Jeanloz, R. & Ahrens, T.J., 1977. Pyroxenes and olivines: structural implications of shock-wave data for high pressure phases, in *High-Pressure Research*, pp. 439-461, eds Manghnani, M. & Akimoto, S., Academic Press, New York.

Jeanloz, R. & Ahrens, T.J., 1980. Anorthite: Thermal equation of state to high pressures, *Geophys. J. R. astr. Soc.*, **62**, 529-549.

Jenkins, F.A. & White, H.E., 1976. *Fundamentals of Optics*, McGraw-Hill, New York, 746 pp.

Kormer, S.B., Sinitsyn, M.V., Kirillov, G.A. & Urlin, V.D., 1965. Experimental determination of temperature in shock-compressed NaCl and KCl and of their melting curves at pressures up to 700 kbar, *Sov. Phys. JETP*, **21**, 689-700.

Liu, L.-G., 1978. A new high-pressure phase of $Ca_2Al_2SiO_7$ and implications for the earth's interior, *Earth planet. Sci. Lett.*, **40**, 401-406.

Liu, L.-G., 1979. High-pressure phase transformations in the system $CaSiO_3$–Al_2O_3, *Earth planet. Sci. Lett.*, **43**, 331-335.

Lyzenga, G.A. & Ahrens, T.J., 1979. A multi-wavelength optical pyrometer for shock compression experiments, *Rev. Sci. Instr.*, **50**, 1421-1424.

Lyzenga, G.A., Ahrens, T.J. & Mitchell, A.C., 1983. Shock temperatures of SiO_2 and their geophysical implications, *J. geophys. Res.*, **88**, 2431-2444.

McQueen, R.G., Fritz, J.N. & Marsh, S.P., 1963. On the equation of state of stishovite, *J. geophys. Res.*, **68**, 2319-2322.

McQueen, R.G., Marsh, S.P. & Fritz, J.N., 1967. Hugoniot equations of state of twelve rocks, *J. geophys. Res.*, **72**, 4999-5036.

McQueen, R.G., Marsh, S.P., Taylor, J.W., Fritz, J.N. & Carter, W.J., 1970. The equation of state of solids from shock wave studies, in *High Velocity Impact Phenomena*, pp. 294-419, ed. Kinslow, R., Academic Press, New York.

Mitchell, A.C. & Nellis, W.J., 1981. Diagnostic system of the Lawrence Livermore National Laboratory two-stage light-gas gun, *Rev. Sci. Instr.*, **50**, 347-359.

Rice, M. H., McQueen, R. G. & Walsh, J. M., 1958. Compressibility of solids by strong shock waves, *Solid State Phys.*, **6**, 1-63.

Robie, R.A., Hemingway, B.S., & Fisher, J.R., 1979. *Thermodynamic Properties of Minerals at 298.15 K and 1 Bar (10^5 Pascals) Pressure and at Higher Temperatures*, Government Printing Office, Washington, D.C.

Ross, J.E. & Aller L.H., 1976. The chemical composition of the sun, *Science*, **26**, 1223-1229.

Schmitt, D. R. & Ahrens, T. J., 1983. Temperatures of shock-induced shear instabilities and their relationship to fusion curves, *Geophys. Res. Lett.*, in press.

Turekian, K.K. & Clark, S.P., Jr., 1969. Inhomogeneous accretion model of the earth from the primitive solar nebula, *Earth planet. Sci. Lett.*, **6**, 346-348.

Urtiew, P.A. & Grover, R., 1974. Temperature deposition caused by shock interactions with material interfaces, *J. Appl. Phys.*, **45**, 140-145.

Wallace, D.C., 1972. *Thermodynamics of Crystals*, J. Wiley & Sons, New York, 484 pp.

Chapter 3

Hugoniot Equation of State of Anorthite Glass and Lunar Anorthosite

ABSTRACT

Twenty-one Hugoniot experiments were conducted on an amorphous material of anorthite composition, in the pressure range from 8 to 120 GPa, using both routine and new methods. Two Hugoniot measurements at about 120 GPa were made on lunar gabbroic anorthosite. Theoretical Hugoniots are constructed for both materials assuming they disproportionate to their component oxides. These accurately predict the P-ρ behavior of the lunar anorthosite Hugoniot at 120 GPa and the anorthite glass Hugoniot above 50 GPa, but overestimate the shock temperatures of anorthite glass. They do not predict the release paths of either material. We conclude that the mixed oxide model is a good description of the bulk properties of the high pressure phases of anorthite, but does not represent the actual phases. A significant enrichment of the earth's lower mantle is not precluded by the bulk properties of the anorthite high pressure phases.

Introduction

Anorthite is a mineral of considerable geophysical importance because it is among the first phases to condense in nebula models of the formation of the solar system (Grossman & Larimer, 1974). If the accretion process began before condensation was complete, the lower mantle would be expected to be enriched in refractories (Turekian & Clark, 1969). Such an inhomogeneous model would predict that a high pressure phase assemblage derived from anorthite is a major component of the lower mantle. Calculations based on cosmochemical abundances of Si, Mg, Al, and Ca (Ross & Aller, 1976) predict a mean mass fraction of 0.12 and 0.16 for an anorthite-composition phase in a predominantly enstatite- or forsterite-composition mantle, respectively.

Due to its geophysical importance, anorthite has been the subject of several shock wave studies. McQueen *et al.* (1967) conducted Hugoniot experiments on Tahawus anorthosite at pressures from 15 to 95 GPa. The samples used in this study were crystals, which were 90% plagioclase with .49 mole fraction anorthite, and initial densities ranging from 2.70 to 2.79 Mg/m^3 . McQueen *et al.* (1967) inferred from their data that above about 33 GPa the Hugoniot enters a regime in which the shock states correspond to a high pressure phase with a zero pressure density of between 3.46 and 3.53 Mg/m^3, and an initial isentropic bulk modulus of 88 to 112 GPa. This high pressure phase gives a close match to the seismologically-determined lower mantle density, but the inferred bulk modulus is considerably less than the lower mantle at comparable conditions.

Additional Hugoniot experiments of Ahrens *et al.* (1969a) on plagioclase from 18 to 68 GPa also indicate a transition of this material to a high-pressure high-density polymorph above 30 GPa. It was concluded in this study, and by

Ahrens *et al.* (1969b) that the high-pressure polymorph corresponds to the hollandite structure.

Jeanloz & Ahrens (1980) carried out a series of Hugoniot experiments on lunar anorthosite 60025, which is about 18% porous, and single-crystal Miyakezima anorthite. Shock pressures attained ranged from 40 to 120 GPa. The porous data were used to determine the Gruneisen parameter, and a thermal equation of state was constructed for the high pressure phase. The zero pressure density and initial isentropic bulk modulus were concluded to be 3.40 Mg/m^3 and 86.5 GPa, respectively for the calculated Hugoniot which gave the best fit to the data inferred by the authors as belonging in the high pressure regime, above 33 GPa. This is in close agreement with the lower values of McQueen *et al.* (1967). Jeanloz & Ahrens (1980) also concluded that, despite a close match in density to the lower mantle, the high pressure phase or phase assemblage of anorthite is too compressible to constitute a major lower mantle component.

Boslough *et al.* (1983a) conducted shock temperature experiments on anorthite glass in order to further study its high pressure thermal behavior at pressures from 50 to 115 GPa and temperatures of 2500 to 5600°K. They found significant deviations in measured temperatures from what would be calculated assuming a simple single-high-pressure-phase model in this pressure range, and concluded that as many as three phase transitions might occur between 50 and 115 GPa, at about 55, 85, and 100 GPa. Shock temperature experiments on anorthite glass were also carried out to about 40 GPa by Schmitt & Ahrens (1983). The high temperatures (≈ 3000°K) measured in these experiments were assumed to be at the melting point of the high pressure phase existing along

shear bands in the shocked material.

The purpose of this paper is to present the first Hugoniot data on anorthite glass, and discuss it in context with the previous porous and single crystal Hugoniot data and shock temperature data to generate a more complete self-consistent high pressure equation of state. For comparison, new Hugoniot data are presented for a lunar recrystallized and brecciated gabbroic anorthosite (Apollo 15,418). This rock was the subject of previous shock wave work by Ahrens el al. (1973) at pressures up to 28 GPa.

Experiment

Several different experimental techniques were employed to determine the Hugoniot of anorthite glass, all based on measuring the shock velocity through the sample. Determination of partial and fully released states in some samples was made by the use of low density buffer material and in two cases the free surface velocity was measured using an inclined mirror affixed to the sample (Ahrens & Gregson, 1964). Experiments were performed using either a 40 mm-bore propellant gun (Ahrens *et al.*, 1971) or a two-stage light-gas gun.

First, the standard Hugoniot experiment, as described by Jeanloz & Ahrens (1977) was used (Fig. 3-1). Second, anorthite "rider" mirrors were used in lieu of fused quartz mirrors on Hugoniot experiments which were primarily for other samples (Fig. 3-1). Third, shock transit times were measured from the oscillograms used primarily to determine the shock temperatures (Fig. 3-2) and finally, transit times were determined by obtaining streak camera records of light transmitted from the sample via optic fibers in several of the shock temperature experiments (Figs. 3-3 and 3-4).

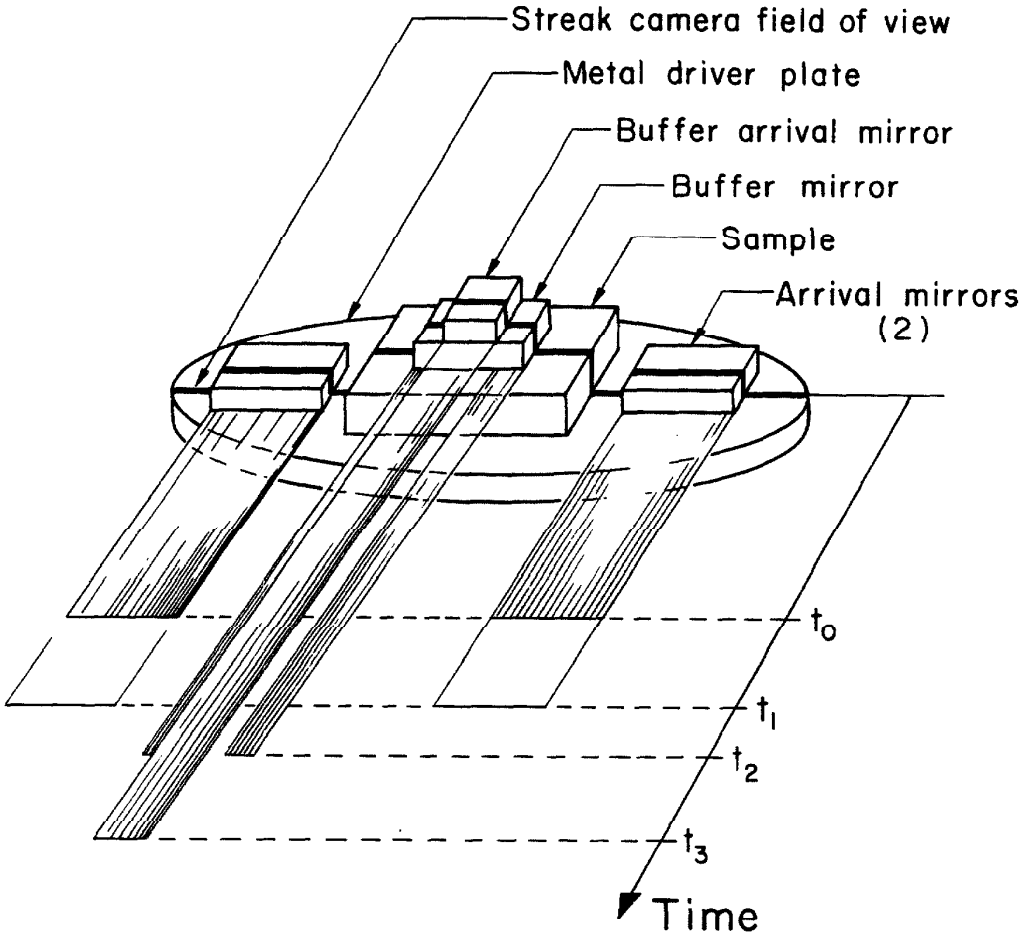

Fig. 3-1. Configuration of standard Hugoniot experiments including schematic representation of streak. Times t_0, t_1, t_2, and t_3 correspond to shock wave arrival at: driver-arrival mirror interface, arrival mirror free surface, sample-buffer mirror interface, buffer mirror-buffer arrival mirror interface, respectively. In ideal experiment (no shock tilt or bowing), transit times are: (t_2-t_0) for sample, (t_1-t_0) for arrival mirror, and (t_3-t_2) for buffer mirror. In the "rider" experiment, arrival mirrors are made of anorthite glass.

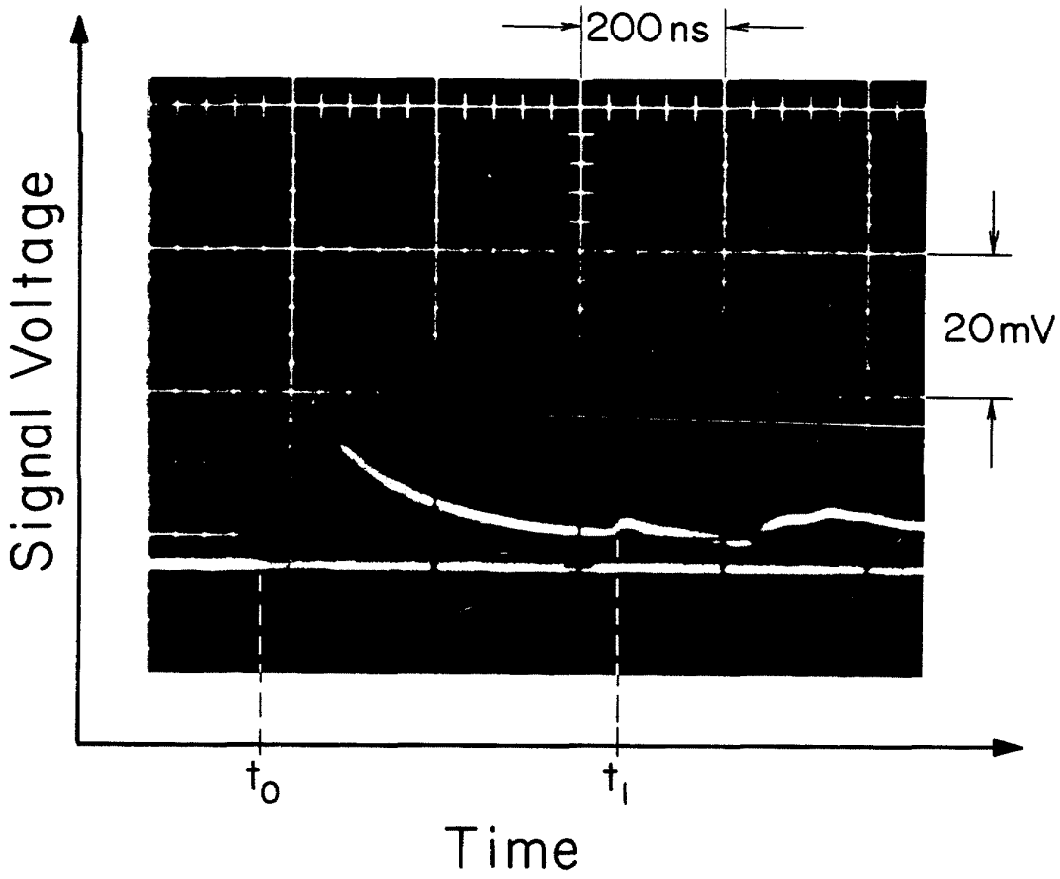

Fig. 3-2. Oscilloscope record from 750 nm channel of optical pyrometer; shot LGG 132 (An6T) to 48 GPa. At time t_o, shock wave arrives at driver-sample interface. At t_1, shock reaches sample free surface.

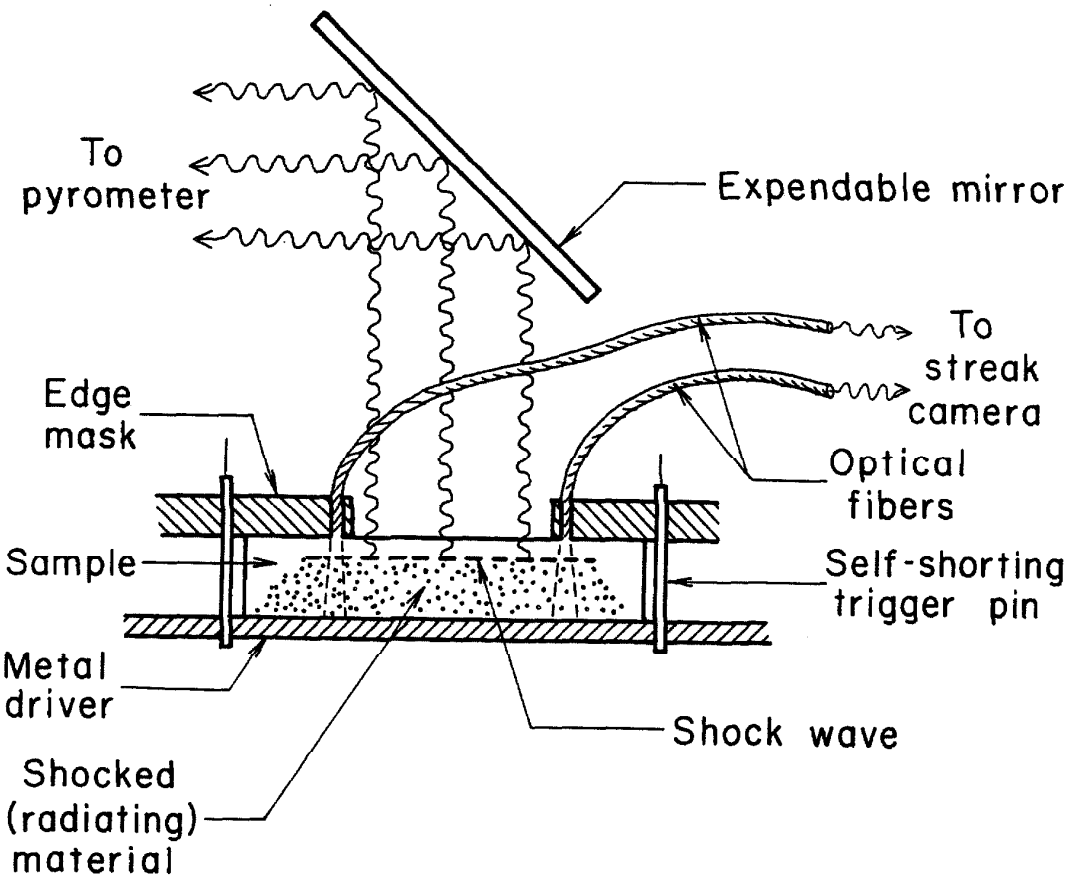

Fig. 3-3. Configuration of shock-temperature experiments in which Hugoniot data are also obtained. In one method, the shock transit time is taken from the optical pyrometer oscilloscope records of the light radiated from the shocked sample. In the other method, light is collected by optical fibers and conducted to a streak camera.

TJA83126SFD

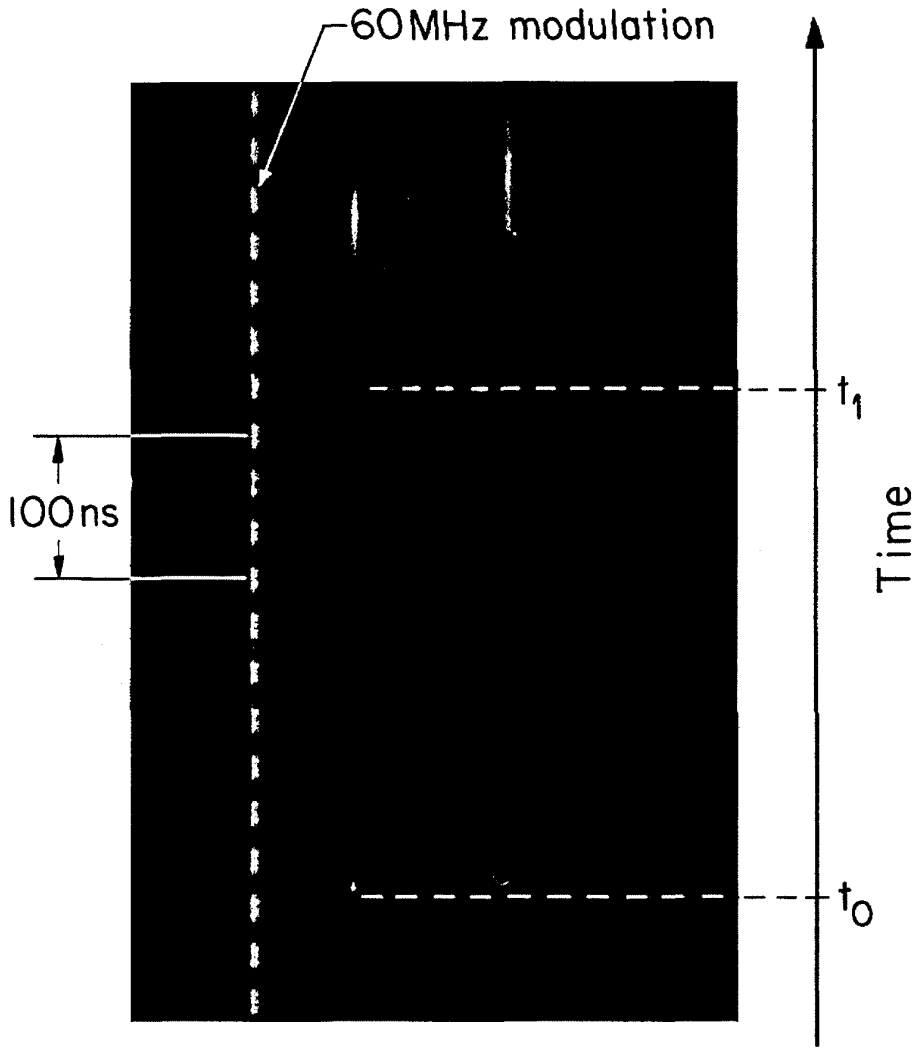

Fig. 3-4. Streak camera record from shot LGG 136 to 92 GPa, illustrating use of optical fibers in conjunction with shock temperature experiment to determine shock transit time. At time t_0, shock wave enters sample from opaque driver, and fiber collects thermally radiated light. At t_1, shock reaches sample-fiber interface and light intensity decreases. Time calibration is by a laser modulated at 60 MHz by a Pockels cell. Three of six fiber traces are shown.

In the standard Hugoniot experiment (Fig. 3-1), a shock wave is generated by the impact of a light-gas gun or 40mm gun-launched flyer plate with a stationary driver plate, on which are mounted the polished sample and two silvered quartz or polycarbonate (Lexan) arrival mirrors. After traveling through the driver plate, the shock enters the sample and mirrors. When the shock wave arrives at the driver-mirror interface, the lapped surface of the driver is driven into the specularly reflecting surface of the mirror, resulting in a rapid change in reflectivity which can be observed by monitoring the reflected light with a high speed Model 339B Beckman-Whitely continuous writing rotating mirror or TRW model 21A image converter streak camera. The shock wave continues through the sample to its other surface, where it impinges on a fused quartz or Lexan buffer mirror which changes its reflectivity in the same manner, providing a measure of the shock transit time through the sample. When the shock wave reflects from the buffer-sample interface, a rarefaction to a lower pressure state propagates back into the anorthite. Simultaneously a shock wave with the same pressure and particle velocity is driven into the buffer material. The arrival of this lower amplitude shock wave at the buffer material free surface is again detected by the loss of reflectivity of a buffer arrival mirror, which provides a measure of the shock transit time in the buffer. In some cases the buffer material was replaced by an inclined mirror whose angle of extinction allowed determination of the free surface velocity of the shocked sample. Solution of the Reimann integral (Rice *et al.*, 1958, Lyzenga & Ahrens, 1978) allowed determination of a partial (buffer) or full (inclined mirror) release state in the sample.

The "rider" method is a modification of this experiment, in which the sample is not anorthite glass, but some other material for which the experiment is primarily intended (Fig. 3-1). The arrival mirrors, however, are fabricated out of anorthite glass. When the shock wave arrives at the driver-sample interface the silvered surfaces of the anorthite arrival mirrors lose their reflectivity in the usual way. The top, unsilvered surface of the mirror material continues to reflect at about 5% this intensity, and does so until the shock wave reaches it. The light signal disappears within ≈ 2 ns of shock arrival, either as a result of shock tilt misaligning the free surface of the mirror in such a way that the light reflected from the xenon light source misses the aperture of the streak camera, or due to disruption of the specular reflecting quality of the surface by an unknown process. This appears on the streak as a lighter image, from which the transit time through the anorthite glass mirror can be determined. The anorthite glass mirrors still serve the same functional purpose as the normal mirror in determining the Hugoniot of the primary material. The states determined for the anorthite glass by this method are not as precise as those determined by the standard method, because the rider mirrors are about half the thickness (≈ 1.1 mm) of the standard samples. This doubles the fractional error in the shock velocity measurement. A release state is not determined for anorthite glass with this method.

Hugoniot states were also determined in the shock temperature experiments. The most straightforward method was to simply take the shock transit time from the oscilloscope shot records (Fig. 3-2), which display light intensity as a function of time (Boslough *et al.*, 1983a). This technique is less precise than the standard method for two reasons. First, the time resolution is limited by the

rise times of the photodiodes, which are 1 to 7 ns. Second, the field of view of the photodiodes (2.3 to 6.4 mm) is much larger than the slit width of the streak camera (0.13 mm), so if the shock wave is not perfectly parallel to the sample surfaces (because of projectile tilt or slight misalignment) this will not be resolved. For some samples, the optical quality of the sample may preclude the use of this method in determining shock transit times (Boslough *et al.* 1983b).

Several of the shock-temperature targets were designed to allow the streak camera to be used in measuring the shock-transit time, with the intent on improving the precision over reading the oscillograms. Several 0.25 mm diameter, Poly-Optical Products Co., acrylic optical fibers with polished ends were attached to the free surface of the samples, and held in place by the edge mask (Fig. 3-3). When the shock wave enters the sample, thermal radiation is collected by the optic fibers and carried to the streak camera. When the shock reaches the sample-fiber interface, the light intensity changes due to the impedance mismatch as the shock is driven into the fiber itself. The transit time is obtained by measuring the length of the bright streak (Fig. 3-4). This technique is not degraded by shock wave tilt, as the field of view of the fiber is on the order of the fiber diameter itself. The time resolution is decreased somewhat, however, by the fact that the fiber diameter is 0.25 mm, as opposed to the slit width in the standard experiments of 0.13 mm. By using 0.13 mm diameter fibers, or mounting larger fibers behind the 0.13 mm wide slit, this method can achieve the same precision as the standard Hugoniot experiment. A shock temperature of about 3500°K in the sample, corresponding to a spectral radiance in the visible of about 10^{12} $Wsr^{-1}m^{-3}$, is required to produce enough light intensity to give a sufficient exposure of the film in the streak camera when 0.25 mm

diameter fibers are used. If finer fibers are used, the required shock temperature will be higher. The required spectral radiance is approximately inversely proportional to the fiber diameter.

Results

The results of 21 Hugoniot measurements on anorthite glass are presented in Table 3-1 and shown in Figs. 3-5 through 3-8. Previous data for Izu Island anorthite (Jeanloz & Ahrens, 1980), porous lunar anorthosite 60025 (Jeanloz & Ahrens, 1978) and Tahawus anorthosite (McQueen *et al.*, 1967) are also shown in Fig. 3-6 for comparison.

All but six data from the present study are in the high pressure phase region, and are plotted in the U_s-u_p plane in Fig. 3-7. The high pressure phase data can be fitted by the linear relationship:

$$U_s = c_o + su_p \qquad (3\text{-}1)$$

A least squares fit gives the values c_o=1.64±0.26 km/s and s=1.82±0.07. This equation can be used for impedance match solutions, and was used to determine the pressures in the shock-temperature experiments by Boslough *et al.* (1983a).

The remaining data lie in the mixed phase region or in the low pressure phase region and form an approximately horizontal trend in U_s–u_p space (Fig. 3-7). Two samples have anomalously high shock velocities relative to the remainder and were excluded from the diagram. Poor shot records made these two experiments difficult to interpret and although they are included in Table 3-1, they will not be discussed further. A similar horizontal trend in U_s–u_p space has been described by Wackerle (1962) for the mixed phase region of fused

Table 3-1

Anorthite Glass Hugoniot and Release Data

Shot	Flyer Material	Driver Material	Projectile Velocity (km/s)	Initial Density (Mg/m^3)	Shock Velocity (km/s)	Particle Velocity (km/s)	Pressure (GPa)	Density (Mg/m^3)	Method
40-577	Al-2024	Al-2024	0.95 ± .01	2.691 .002	6.85 ± .12	0.45 ± .01	8.32 ± .12	2.881 0.006	(a)
	Partial Release State 1 (Lexan buffer)				3.48 ± .05	0.73 ± .03	3.05 ± .18	2.76 ± .03	(a)
	Partial Release State 2 (Graphite Foam buffer)				1.60 ± .02	0.62 ± .02	1.08 ± .04	2.85 ± .01	(a)
40-589	Lexan	Al-2024	1.97 ± .01	2.697 ± .002	6.42 ± .05	0.484 ± .004	8.37 ± .06	2.912 ± .003	(a)
	Partial Release State (Lexan buffer)				3.46 ± 0.03	0.72 ± .02	2.98 ± .11	2.827 ± .014	(a)
	Final Release State (e) (Inclined mirror)				-	1.02 ± .03	0.00	2.64 ± .04	(a)
40-581	Al-2024	Al-2024	1.00 ± .02	2.693 ± .002	6.36 ± .04	0.49 ± .01	8.46 ± .18	2.920 ± .006	(a)
	Partial Release State (Lexan buffer)				3.50 ± .03	0.745 ± .019	3.12 ± .11	2.822 ± .021	(a)
	Final Release State (e) (Inclined mirror)				-	0.87 ± .02	0.00	2.78 ± .04	(a)
40.580	Al-2024	Al-2024	1.105 ± .010	2.692 ± .002	6.745 ± .005	0.534 ± .006	9.69 ± .10	2.923 ± .003	(a)
	Partial Release State 1 (Lexan buffer)				3.47 ± .04	.726 ± .025	3.01 ± .14	2.876 ± .013	(a)
	Partial Release State 2 (Polystyrene foam buffer)				1.07 ± .05	0.74 ± .04	0.0 ± .(	2.886 ± .016	(a)

Table 3-1 (cont'd)

Shot	Flyer Material	Driver Material	Projectile Velocity (km/s)	Initial Density (Mg/m^3)	Shock Velocity (km/s)	Particle Velocity (km/s)	Pressure (GPa)	Density (Mg/m^3)	Method
40-587	Al-2024	Al-2024	2.266 ± .003	2.693 ± .002	6.46 ± .06	1.179 ± .005	20.52 ± .11	3.295 ± .010	(a)
	Partial Release State 1 (Lexan buffer)				3.53 ± .04	0.764 ± .025	3.227 ± .144	3.19 ± .02	(a)
	Partial Release State 2 (Polystyrene foam buffer)				1.94 ± .02	1.52 ± .02	0.165 ± .004	3.235 ± .013	(a)
40-588	W	Cu	2.455 0.005	2.693 ± .002	6.40 ± .04	2.279 ± .006	39.28 ± .21	4.182 ± .018	(a)
	Partial Release State 1 (Lexan buffer)				6.24 ± .08	2.49 ± .05	18.59 ± .62	4.14 ± .03	(a)
	Partial Release State 2 (Graphite foam buffer)				4.89 ± .05	0.15 ± .04	16.67 ± .37	3.66 ± .04	(a)
LGG 132	Cu	Cu	3.72 ± .10	2.6908 ± .0010	6.508 ± .092	3.731 ± .078	47.8 ± 1.5	4.636 ± .112	(c)
LGG 131	Cu	Cu	4.038 ± .002	2.6909 ± .0013	7.027 ± .081	2.929 ± .008	55.4 ± 0.5	4.614 ± .047	(c)
LLL 091880	Cu	Cu	4.536 ± .006	2.6900 ± .0010	7.717 ± .103	3.247 ± .011	67.4 ± 0.7	4.644 ± .056	(c)
LGG 138	Cu	Cu	5.255 ± .003	2.6953 ± .0012	6.167 ± .240	3.753 ± .025	82.8 ± 1.9	4.977 ± .152	(d)
LLL 091680	Cu	Cu	5.455 ± .010	2.6899 ± .0011	8.596 ± .050	3.867 ± .009	89.4 ± 0.4	4.868 ± .030	(c)
LGG 136	Cu	Cu	5.506 ± .003	2.6923 ± .0011	8.769 ± .085	3.887 ± .009	91.8 ± 0.7	4.836 ± .046	(d)
LGG 137	Cu	Cu	5.563 ±.006	2.6927 ±.0011	8.782 ±.093	3.930 ±.011	92.9 ±0.8	4.874 ±.052	(d)

Table 3-1 (cont'd)

Shot	Flyer Material	Driver Material	Projectile Velocity (km/s)	Initial Density (Mg/m^3)	Shock Velocity (km/s)	Particle Velocity (km/s)	Pressure (GPa)	Density (Mg/m^3)	Method
LGG 124	Cu	Cu	5.709 ±.003	2.6894 ±.0018	8.956 ±.068	4.025 ±.008	96.9 ±0.6	4.885 ±.037	(a)
	Partial Release State (Fused quartz buffer)				8.512 ±.095	4.461 ±.051	83.7 ±1.9	4.566 ±.116	(a)
LGG 114	Cu	Cu	5.892 ±.005	2.6912 ±.0018	9.352 ±.152	4.124 ±.016	103.8 ±1.3	4.814 ±.076	(b)
LGG 133	Cu	Cu	6.166 ±.004	2.6912 ±.0018	9.535 ±.090	4.315 ±.010	110.7 ±0.8	4.915 ±.047	(b)
LLL 062380	Ta	Ta	5.678 ±.010	2.6893 ±.0011	9.525 ±.100	4.345 ±.012	111.3 ±1.0	4.945 ±.052	(a)
LGG 134	Cu	Cu	6.328 ±.004	2.6912 ±.0008	9.785 ±.160	4.412 ±.017	116.2 ±1.5	4.901 ±.081	(b)
LGG 139	Ta	Cu	5.562 ±.003	2.6944 ±.0012	9.639 ±.089	4.444 ±.010	117.8 ±0.8	4.914 ±.045	(d)
LGG 129	Cu	Cu	6.547 ±.004	2.6924 ±.0020	9.784 ±.106	4.580 ±.012	120.6 ±1.0	5.082 ±.060	(a)
	Partial Release State (Fused quartz buffer)				9.328 ±.153	4.899 ±.082	100.7 ±3.3	4.935 ±.104	(a)
LGG 143	Ta	Ta	6.110 ±.005	2.6903 ±.0014	9.843 ±.136	4.899 ±.013	121.1 ±1.4	5.148 ±.077	(b)

(a) Standard equation of state experiment.

(b) Mirror "riders" - (density from mean of other shots).

(c) Transit time from shock temperature oscilliscope records.

(d) Transit time from optic fibers to streak camera.

(e) Free surface velocity listed as particle velocity.

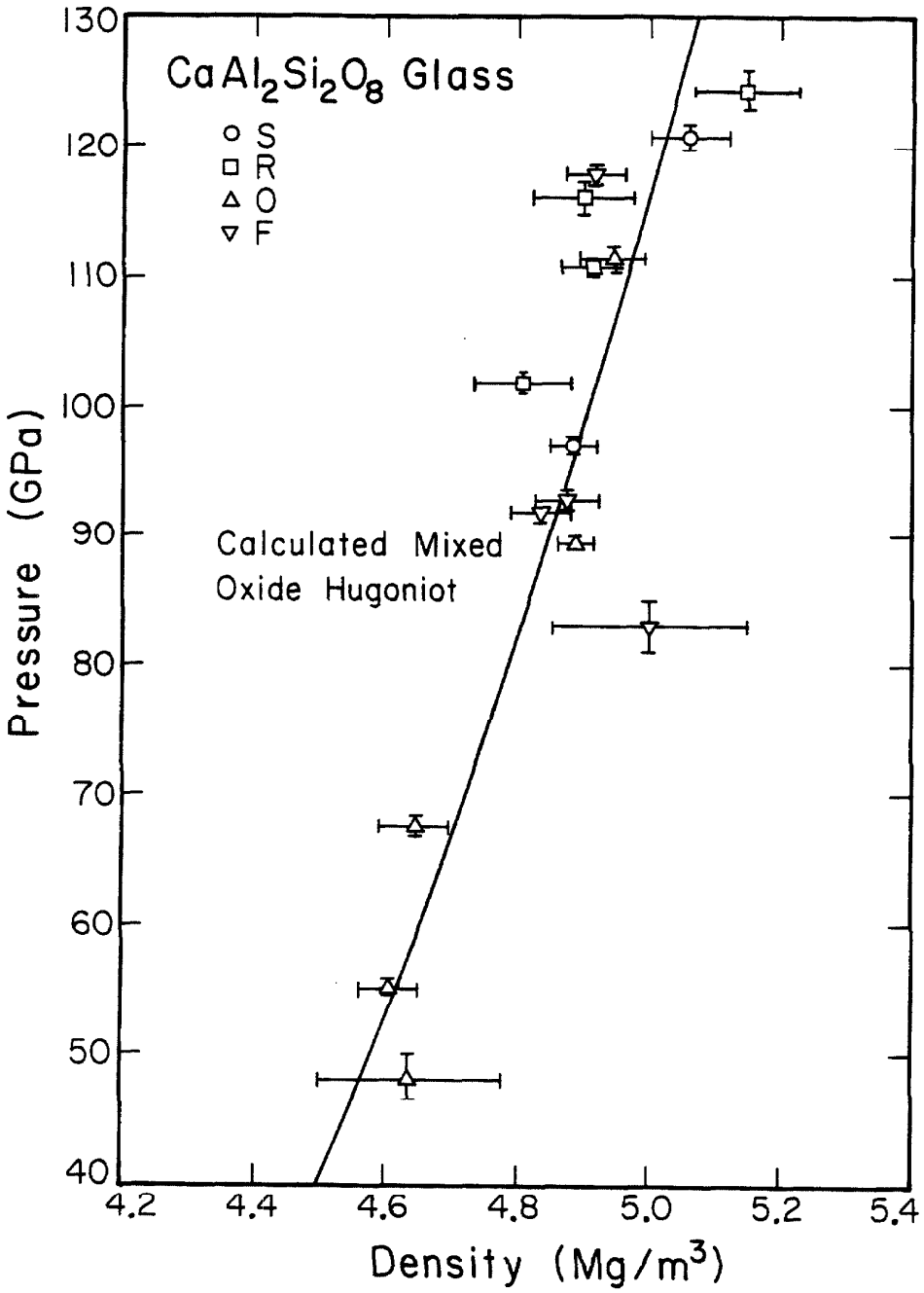

Fig. 3-5. Anorthite glass Hugoniot data in the high-pressure regime from Table 3-1 plotted in the pressure-density plane, with theoretical mixed oxide Hugoniot based on parameters in Table 3-2. Data were obtained by four experimental methods: (S) Standard Hugoniot, (R) "Rider" mirror, (O) Oscilloscope, (F) Optical fiber. These methods are described in text.

TJA83120SFD

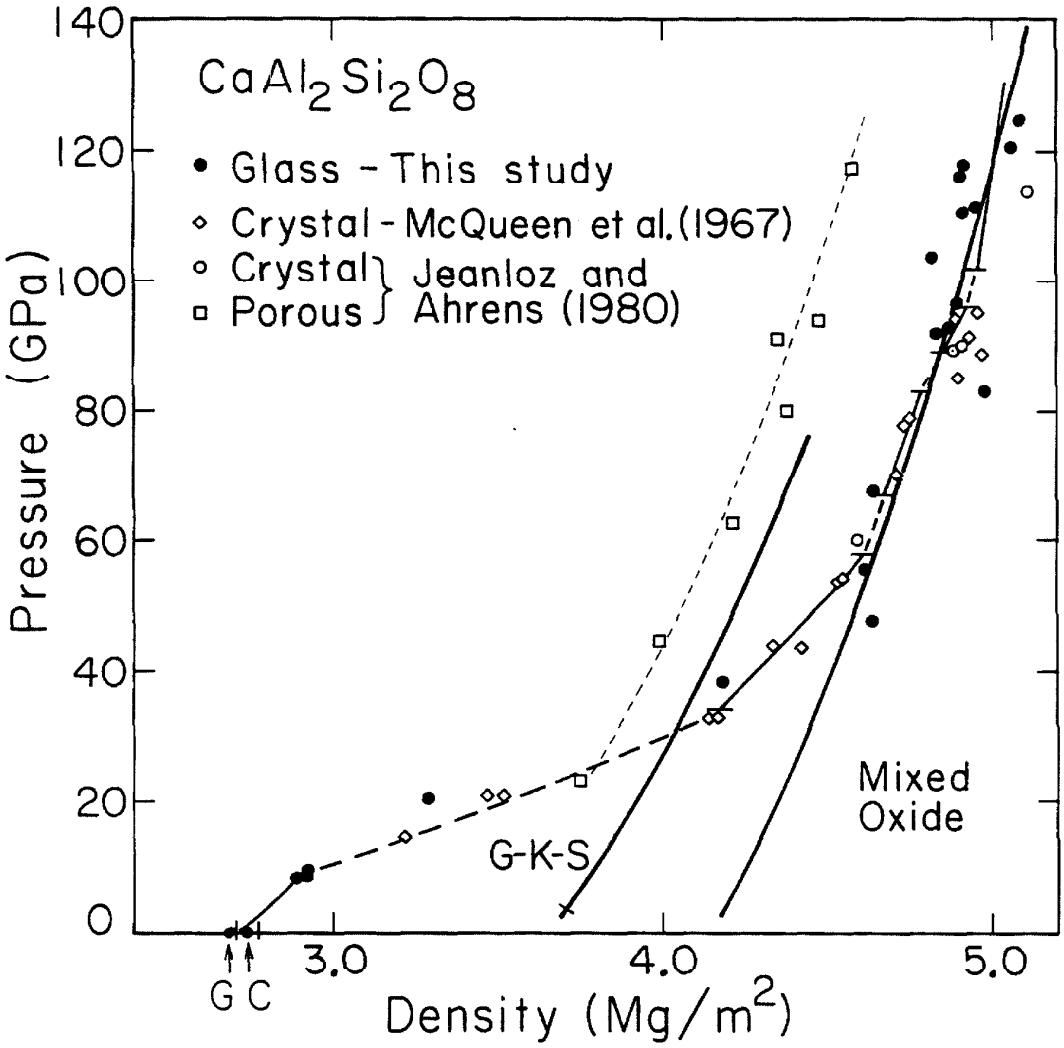

Fig. 3-6. Anorthite glass Hugoniot data from this study, anorthite crystal and porous anorthosite data from Jeanloz & Ahrens (1980), and anorthite crystal data from McQueen *et al.*, (1967). Solid and dashed curves give single phase and mixed phase regions, respectively, based on shock temperature data (Boslough *et al.*, 1983). Mixed oxide theoretical Hugoniot based on parameters in Table 3-2 gives good agreement with data above 55 GPa. Grossularite-Kyanite-Stishovite (G-K-S) theoretical Hugoniot does not agree with data anywhere.

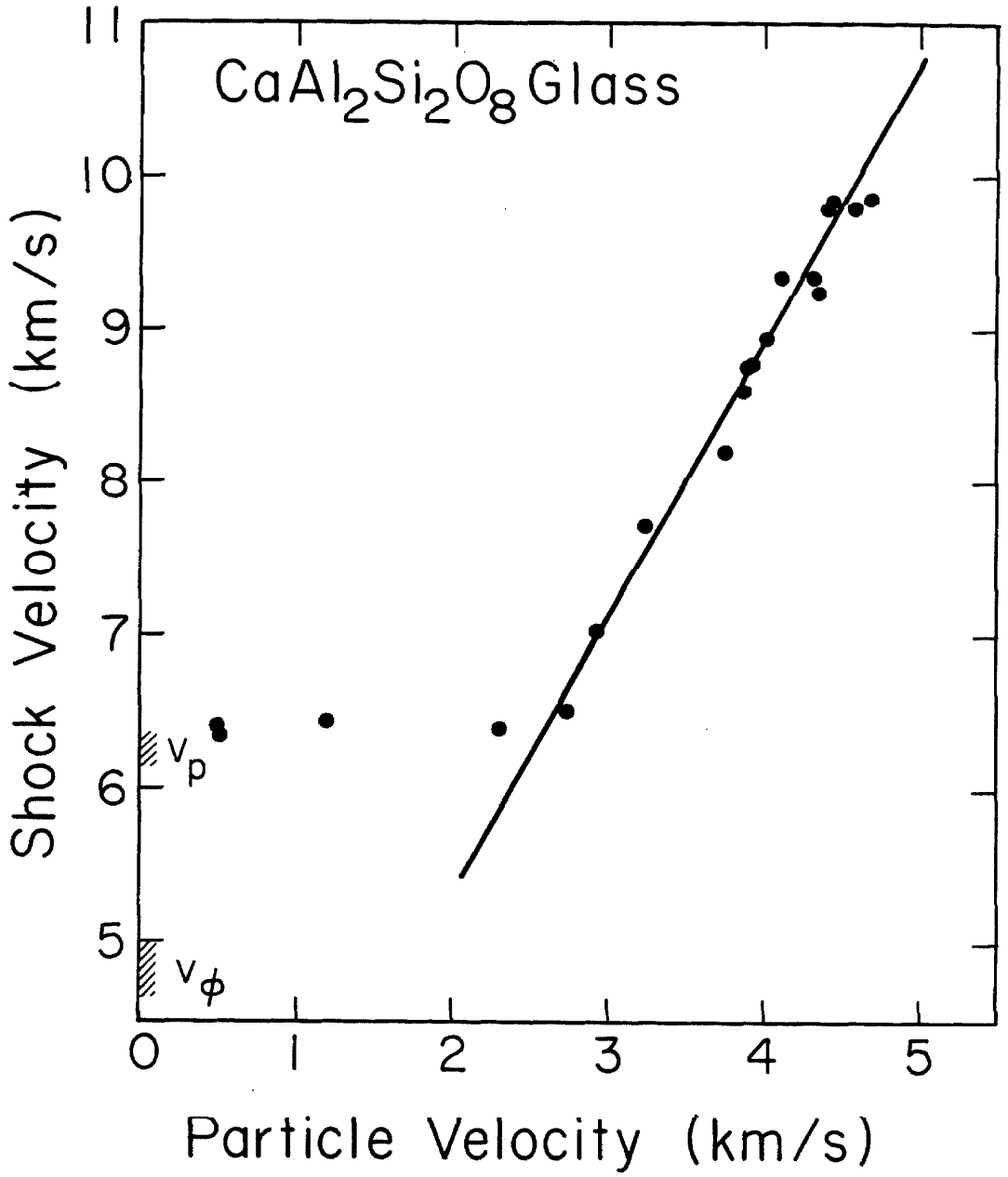

Fig. 3-7. Hugoniot data for anorthite glass shown in the shock velocity-particle velocity plane. Best straight-line fit to high-pressure phase regime data is shown: $U_s=1.64+1.82u_p$. Calculated zero-pressure longitudinal sound velocity (v_p) and bulk sound velocity (v_ϕ) are indicated.

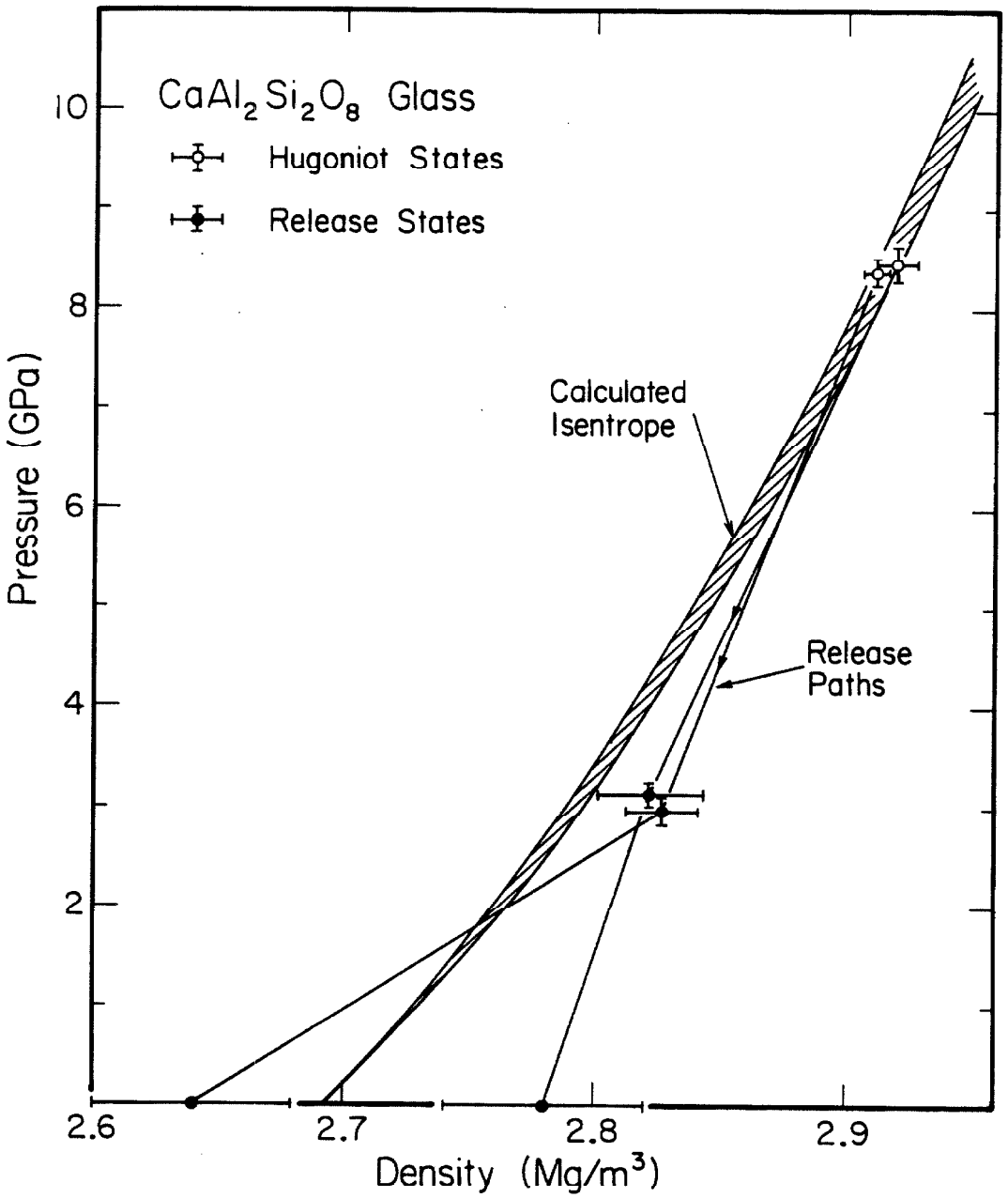

Fig. 3-8. Anorthite glass Hugoniot data with measured release states. Curves are Birch-Murnaghan isentropes constrained by K_{os}=60.4 GPa, K'_{os}=15-16 and K_{os}=67.0, K'_{os}=11.5-12.5. Release paths suggest that irreversible compression can occur in anorthite glass at low pressures and are consistent with the calculated range of isentropes.

quartz.

None of the data show any indication of a two wave structure. This suggests that the data lie below the Hugoniot elastic limit (H.E.L) or sufficiently far above it that the elastic wave has been overridden. Particle velocities calculated from free surface velocities which were derived from inclined mirror experiments are compatible with particle velocities calculated by impedance match. This is consistent with the observation of a single shock wave.

For crystalline feldspars H.E.L. states are dependent upon driving shock pressure and vary upwards from 3.2 GPa for albite, 4.5 GPa for anorthosite (Ahrens & Gregson, 1964) and 3.5 GPa for microcline (Ahrens & Liu, 1973). For crystalline and fused quartz the lowest H.E.L. states measured by Wackerle (1962) were 4.5 GPa. The states measured in this work for anorthite glass yield pressures on the order of 8 GPa. These pressures are considered to be too high to represent states below the H.E.L. and are suggested instead to be plastic deformational states well above the H.E.L.

Release data from the low pressure phase regime and at the low density end of the mixed phase region show generally steep release paths (Figs. 3-8 & 3-9). Buffer materials used were polystyrene foam (ρ_o = 0.056 Mg/m^3, c_o = 0.243 km/s, s = 1.118) and graphite foam (ρ_o = 1.081 Mg/m^3, c_o = 0.79 km/s, s = 1.30). Inclined mirrors were also used to help constrain the release path in two experiments. At the high density end of the mixed phase region the release path suggests reversion to a very low density phase. Fluid-like behavior above the H.E.L. has been observed by Ahrens & Rosenberg (1968) for polycrystalline quartz and has been predicted theoretically by Zamyshlyaev *et al.* (1982).

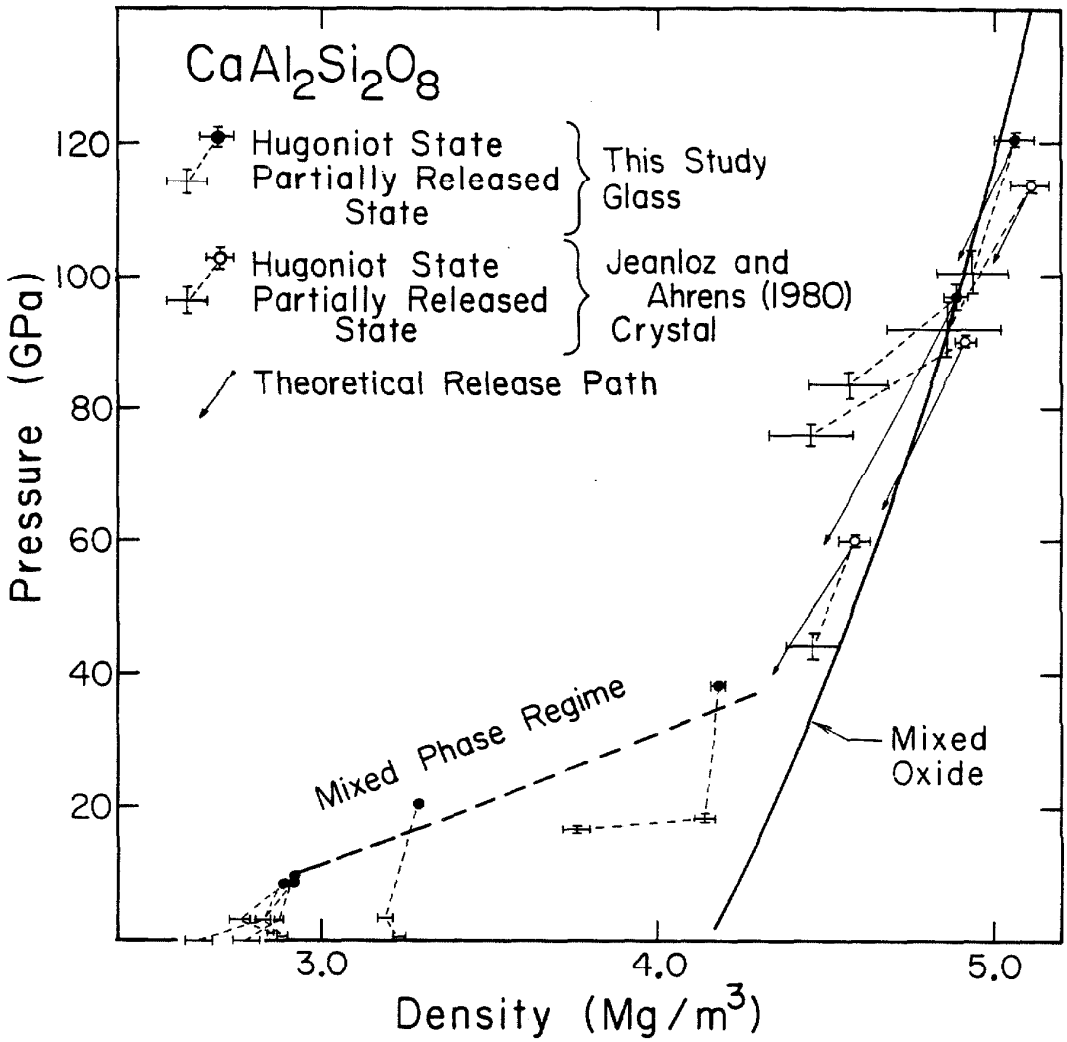

Fig. 3-9. Anorthite glass and crystal Hugoniot data, with measured release states. Theoretical mixed-oxide Hugoniot and corresponding theoretical release isentropes from experimental shock states are shown in the high pressure phase regime. The lowest and two highest states in the high pressure region demonstrate release paths which agree well with the theoretical paths. The two states between 90 and 100 GPa, however, release along significantly shallower paths.

TJA83124SFD

Low pressure equation of state

The low pressure equation of state can be constrained using the two lowest pressure data. The H.E.L. has probably been exceeded for these experiments. At shock states higher than the H.E.L. for anorthite glass it is expected that resistance to shear is lost and that it behaves as a fluid. This phenomenon has been observed in crystal and fused quartz (Wackerle, 1962), perthitic feldspar (Grady *et al.*, 1975) and sapphire (Graham & Brooks, 1971). It has been suggested (Grady *et al.*, 1975) that the loss of shear strength is related to partial melting in shear bands behind the shock front. Shock induced shear instabilities have also been reported for anorthite glass by Schmitt & Ahrens (1983) providing evidence that anorthite glass loses all resistance to shear in common with other ceramic materials.

In the region above the H.E.L., with no shear resistance, the Hugoniot should differ little from the hydrostat. In addition, at low pressures, thermal effects will be small and the Hugoniot will be well approximated by the principal isentrope.

No direct measurement of the bulk modulus of anorthite glass has been made but Young's modulus of an An_{70} glass measured by Birch & Bancroft (1942) is 89.9 GPa. A strong correlation between the product of Young's modulus (E) and ionic packing density (V_t), and the observed bulk modulus (K) for a set of 30 glasses of varying composition is observed by Makishima & MacKenzie (1975). This relation is given by $K = 1.2V_tE$ with V_t calculated from ionic radii and the component atoms normalized to glass density (Makishima & MacKenzie, 1975). From this linear relation, the bulk modulus is estimated to be 60.4 GPa based on E=89.9 GPa, the value measured by Birch & Bancroft (1942). Poisson's ratio for

these values of K and E is 0.252.

Further constraints may be placed on the bulk modulus of anorthite glass using recent ultrasonic data from a variety of silicate glasses. Meister *et al.* (1980) measured the elastic moduli of a range of silicate glass compositions up to 0.8 GPa and noted a good linear relation between bulk modulus and silica content. For anorthite glass this relation would predict a bulk modulus of 67 GPa, and a Poisson's ratio of 0.276, in reasonable agreement with the values calculated using the relation of Makishima & MacKenzie.

With these values of bulk modulus and an assumed Birch-Murnaghan equation of state the pressure derivative of the bulk modulus (K'_s) may be determined from the Hugoniot data. It is assumed that at these pressures the principal isentrope is coincident with the Hugoniot. For K_{os}=60.4 GPa, $K'_{os}\approx$15–16, and for K_{os}=67 GPa, $K'_{os}\approx$11.5–12.5 (Fig. 3-8). These values of K'_{os} suggest rapid stiffening of anorthite glass for moderate increases in pressure. In contrast, $K'_s<3$ for rock silicate glasses at pressures less than 0.8 GPa (Meister *et al.*, 1980). Elastic parameters have been measured for fused quartz from atmospheric pressure to 13.3 GPa (Shroeder *et al.*, 1981). Above about 3 GPa, K'_s increases in a non-linear fashion and at 8 GPa, $K'_s\approx$7.5. Boslough and Ahrens (1983b) suggest that jadeite, in which Al is in octahedral coordination, is formed on the anorthosite Hugoniot in the range 6-10 GPa. Development of some octahedral aluminum on the anorthite glass Hugoniot could lead to substantial stiffening and the observed strong dependence of bulk modulus on pressure.

High pressure equation of state

The shock temperature data of Boslough *et al.* (1983a) indicate that at least three phase transitions occur above 50 GPa on the principal Hugoniot of anorthite glass. The temperature data were used to estimate where the phase boundaries cross the Hugoniot, and this information was transformed to the $P-\rho$ plane in Fig. 3-6, where single- and mixed-phase regions are delineated along the Hugoniot. These phase transitions are not evident from the $P-\rho$ Hugoniot data, except perhaps between 80 and 90 GPa, where there appears to be a sudden increase in density with pressure.

The highest pressure phases are only stable on the Hugoniot in a density range of about 0.1 Mg/m^3, or about 5% of their density, which is the same order as the scatter in the data. This makes it impossible to carry out a meaningful finite strain fit to the data in the individual regions of stability, in which several of the parameters: zero pressure density, K_{os}, and K'_{os} are constrained independently. One alternative is to fix one parameter and determine what values the others must have in order to fit the data. This method does not, however, lead to a unique solution.

Another strategy which can be used is to choose a candidate phase or assemblage, *a priori* and determine its high pressure properties. It can then be compared to the data directly and accepted or rejected as a candidate on this basis. This is similar to the approach of Davies & Gaffney (1973). We used a mixed oxide model as the candidate high pressure assemblage, with CaO in the B2 phase, Al_2O_3 as corundum and SiO_2 as stishovite.

The isentrope for the composite mixed oxide assemblage was constructed from the isentropes of the individual oxides. Molar volumes as a function of

pressure were determined for each of the oxides using the Birch-Murnaghan equation and published values of K_{os} and K'_{os} (Table 3-2). The values for B2 CaO were taken from Boslough *et al.* (1983b), corundum from Anderson (1973) and stishovite from Lyzenga *et al.* (1983). The molar volumes at a given pressure were added to give the molar volume of the composite, from which the pressure-density isentrope was obtained to 100 GPa. K_{os}=227 GPa and K_{os}'=5.1 were determined for the composite by carrying out a Birch-Murnaghan least squares fit to the calculated isentrope (Vasiliou & Ahrens, 1981). The zero pressure bulk modulus calculated in this way is comparable to the Voigt-Reuss-Hill value of 228 GPa, and lies within the Voigt and Reuss bounds of 212 and 244 GPa, respectively (Watt *et al.* 1976).

The Gruneisen parameter (γ) for the composite was calculated by taking the mean of the components, weighted according to mass fraction. Although this is not strictly correct (Duvall & Taylor, 1971) it is a reasonable approximation. The energy of transformation between anorthite glass and the metastable high pressure assemblage at standard conditions (E_{tr}) was obtained from the difference between the sum of E_{tr} for the oxides, and E_{tr} for anorthite glass, with the stable oxides as the reference state.

A Hugoniot was calculated for the composite mixed oxides, with anorthite glass as the initial state. This theoretical Hugoniot is in agreement with shock wave data above 60 GPa (Figs. 3-5 & 3-6), but the temperatures predicted by this model are as much as 1500°K higher than those measured (Boslough *et al.*, 1983a). In order to fit data in both the P–ρ and P-T planes, a somewhat larger transition energy is required.

Table 3-2

Mixed Oxide Parameters - Anorthite glass

	CaO (B2)	Al_2O_3 (Corundum)	SiO_2 (Stishovite)	$CaAl_2Si_2O_8$ (Composite)
ρ_o (g)	4.00	3.986	4.29	4.07
K_{os} (GPa)	121	250	306	222
K'_{os}	5.2	4.0	5.4	5.1
γ	1.80	1.32	1.38	1.44
n	1.0	1.0	3.2	1.7
E_{tr}(kJ/ g)	2.1	0.00	0.82[a]	0.87[b]
m_i	.202	.366	.432	1.00
v_i	.216	.374	.410	1.00
Reference	(c)	(d)	(e)	

(a) Robie (1979)

(b) includes .09 kJ/ g energy of formation of anorthite glass oxides at standard conditions (Robie, 1979)

(c) Boslough et al. (1983)

(d) Anderson (1973)

(e) Lyzenga et al. (1983)

For comparison, a Hugoniot was calculated in the same manner for an assemblage consisting of $Ca_3Al_2(SiO_4)_3$ (grossularite), Al_2SiO_5 (kyanite), and SiO_2 (stishovite), which is the stable phase at 15 GPa according to Liu (1978). This assemblage has a zero pressure density of 3.61 Mg/m^3 and Voigt-Reuss-Hill bulk modulus of 170 GPa. A range of Hugoniots was calculated for this phase, with 3.0 $\leq\gamma_o\leq$ 2.0 and $\gamma=\gamma_o(\frac{\rho_o}{\rho})$. This calculated Hugoniot is steeper than the observed Hugoniot (Fig. 3-6) and crosses it at about 30 GPa.

Discussion

It was concluded by Boslough *et al.* (1983a) that, due to the complicated behavior observed in the anorthite Hugoniot in the P-T plane, a simple equation of state is insufficient to describe this material at high pressure. It is evident, however, that the mixed oxide assemblage is a good model for the behavior in the P–ρ plane above 60 GPa. whereas the grossularite-kyanite-stishovite assemblage is not a good description in any pressure regime. The Jeanloz-Ahrens (1980) equation of state adequately describes the data in both P–ρ and P-T planes from 33 to 60 GPa.

Comparison of the calculated mixed oxide Hugoniot to data in the P-T plane is evidence that the high pressure phase is not mixed oxides, but a phase with similar bulk properties and a greater energy of transformation. Above 55 GPa, the $CaAl_2Si_2O_8$ undergoes further phase transitions, and each higher pressure phase has a larger total energy of transformation. These higher phase transitions are sufficient to lower the shock temperature, but are not significant in the P–ρ plane, implying only a small volume change is associated with each phase

transition. The porous Hugoniot was determined experimentally by Jeanloz & Ahrens (1978, 1980), and does not agree with that calculated using the mixed oxide model, which predicts higher densities at a given shock pressure. In light of the complexity of the high pressure properties of $CaAl_2Si_2O_8$, a reasonable explanation for this is that the porous data do not represent the same phase as the non-porous data, but rather a lower pressure or higher temperature, less dense phase.

It must be remembered that, even though the mixed oxide Hugoniot fits the data well globally, the true Hugoniot goes through several phase transitions, and each phase is only stable along a short segment of the Hugoniot, where material properties such as the bulk modulus and Gruneisen parameter may differ greatly from those of the mixed oxides. Perhaps a better determination of the local compressibilities would be from partial release data. Fig. 3-9 shows that, in fact, the release paths do vary greatly with pressure along the glass and single crystal Hugoniots. Of the four high pressure phase regimes inferred from the shock temperature data by Boslough *et al.* (1983a), three are sampled by the five highest pressure Hugoniot-release experiments in this study and that of Jeanloz & Ahrens (1980). Two experiments sample the highest pressure regime, above 100 GPa. The release paths are within experimental error of those predicted by the mixed-oxide model. The two experiments in which anorthite is shocked into the next highest phase regime, between about 89 and 96 GPa, show significantly different release behavior, indicating release paths much shallower than predicted. The region of stability inferred for this phase is so small and the Hugoniot data so scattered that is not possible to correlate these release paths to a measured Hugoniot. One experimental data point, at about 60 GPa, lies just

above the lowest inferred high pressure phase regime, and its release path is slightly steeper than predicted. Highly variable release paths were also observed in porous anorthite (Jeanloz & Ahrens, 1978, 1980) and in some cases the release paths were steeper than the Hugoniot inferred in that study. Unfortunately, partial release data are generally of lower quality than Hugoniot data.

It is interesting to compare the mixed oxide adiabat to that of the lower mantle, determined seismologically (Dziewonski, *et al.* 1975; Anderson & Hart, 1976; Dziewonski & Anderson, 1981) in Figs. 3-10 through 3-12. In order to make a meaningful comparison, it is necessary to correct the theoretical mixed oxide adiabat to temperatures existing in the mantle. The geotherm of Stacey, (1977) was used. Whereas Jeanloz & Ahrens (1980) found the bulk modulus much too low for anorthite to be a significant component of the lower mantle, the mixed oxide model gives a bulk modulus that is somewhat high, but closer to the seismologically determined lower mantle value. Thus, the high pressure phases of anorthite should not be precluded as major constituents of the lower mantle, especially in light of the fact that there are unresolved phases on the Hugoniot which have bulk moduli which might deviate significantly in either direction from that of the mixed oxide composite.

Lunar anorthosite

In addition to anorthite glass, two experiments were conducted on lunar gabbroic anorthosite (Apollo 15, 418). These experiments were carried out with the standard method (Fig. 3-1), and partial release states were determined in both cases. The results are presented in Table 3-3 and Fig. 3-13. This rock was modeled as .74 volume fraction anorthite (an_{93}) and .26 volume fraction

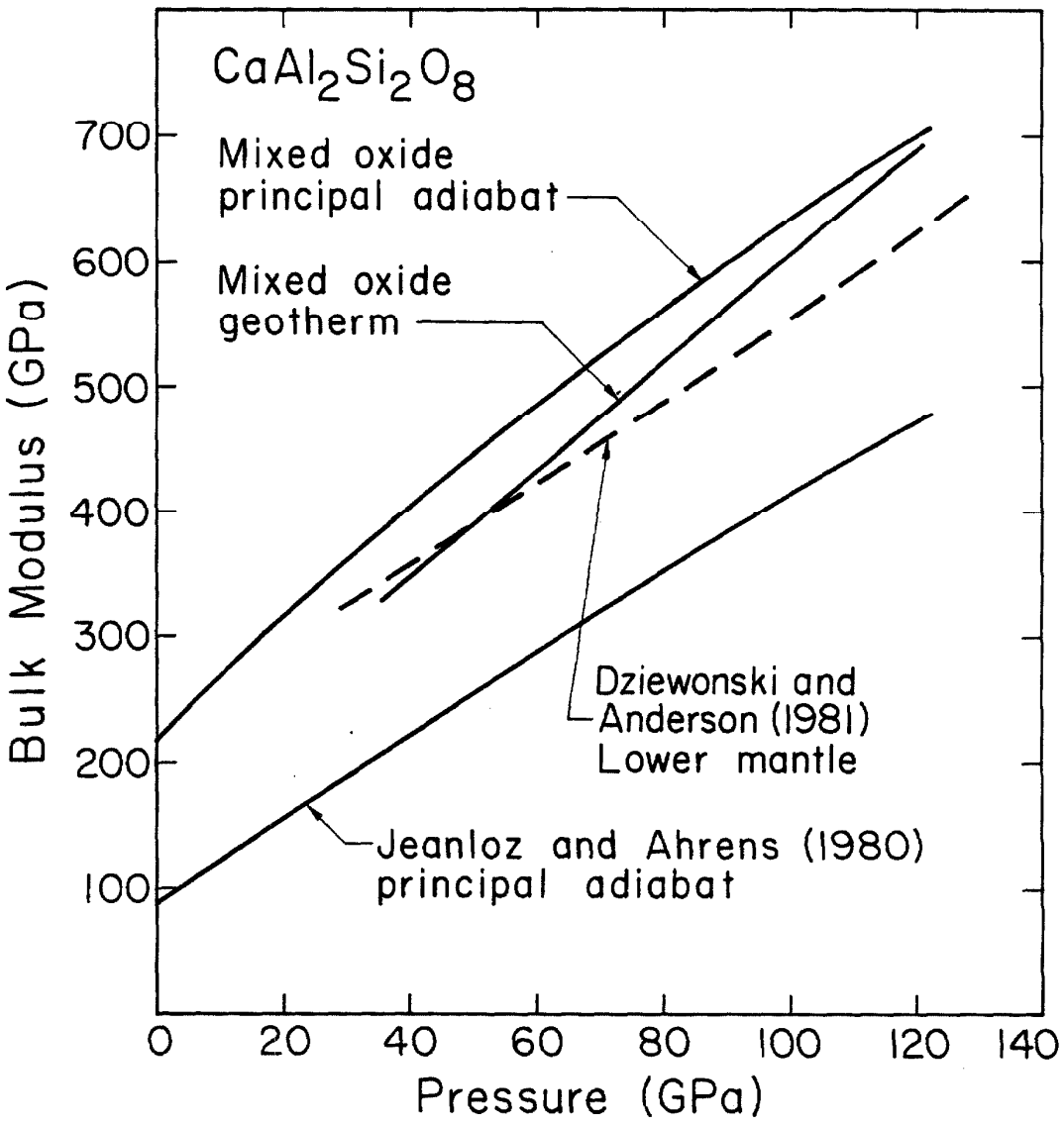

Fig. 3-10. Adiabatic bulk modulus of the mixed oxide model as a function of pressure on principal adiabat and geotherm (Stacey, 1977). Also shown is bulk modulus of mantle as determined from seismological data (Dziewonski & Anderson, 1981), and anorthite adiabat of Jeanloz & Ahrens (1980).

TJA83129SFD

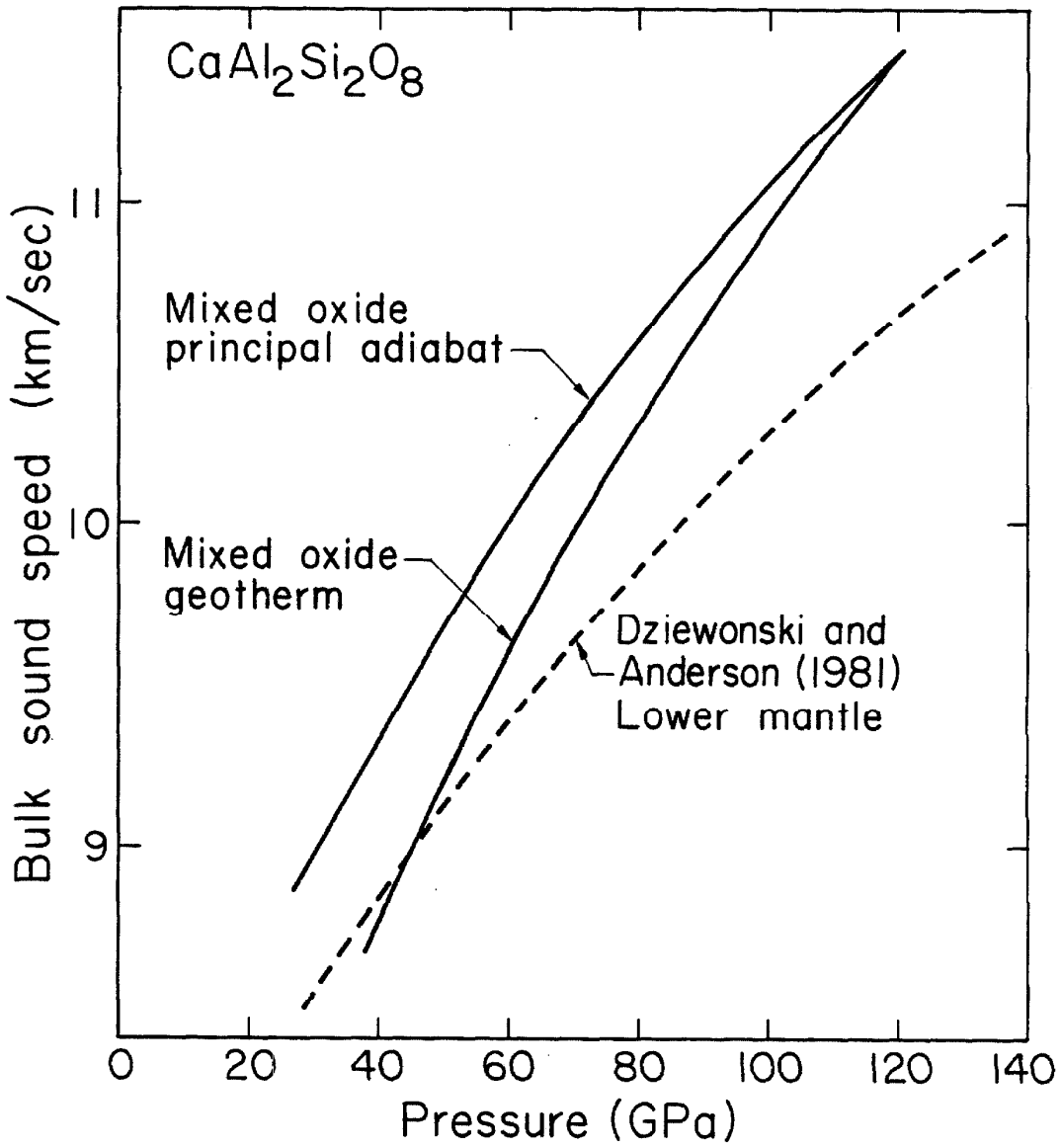

Fig. 3-11. Bulk sound speed of the mixed oxide model as a function of pressure on principal adiabat and geotherm (Stacey, 1977), compared to seismologically determined curve for the earths mantle (Dziewonski & Anderson, 1981).

TJA83128SFD

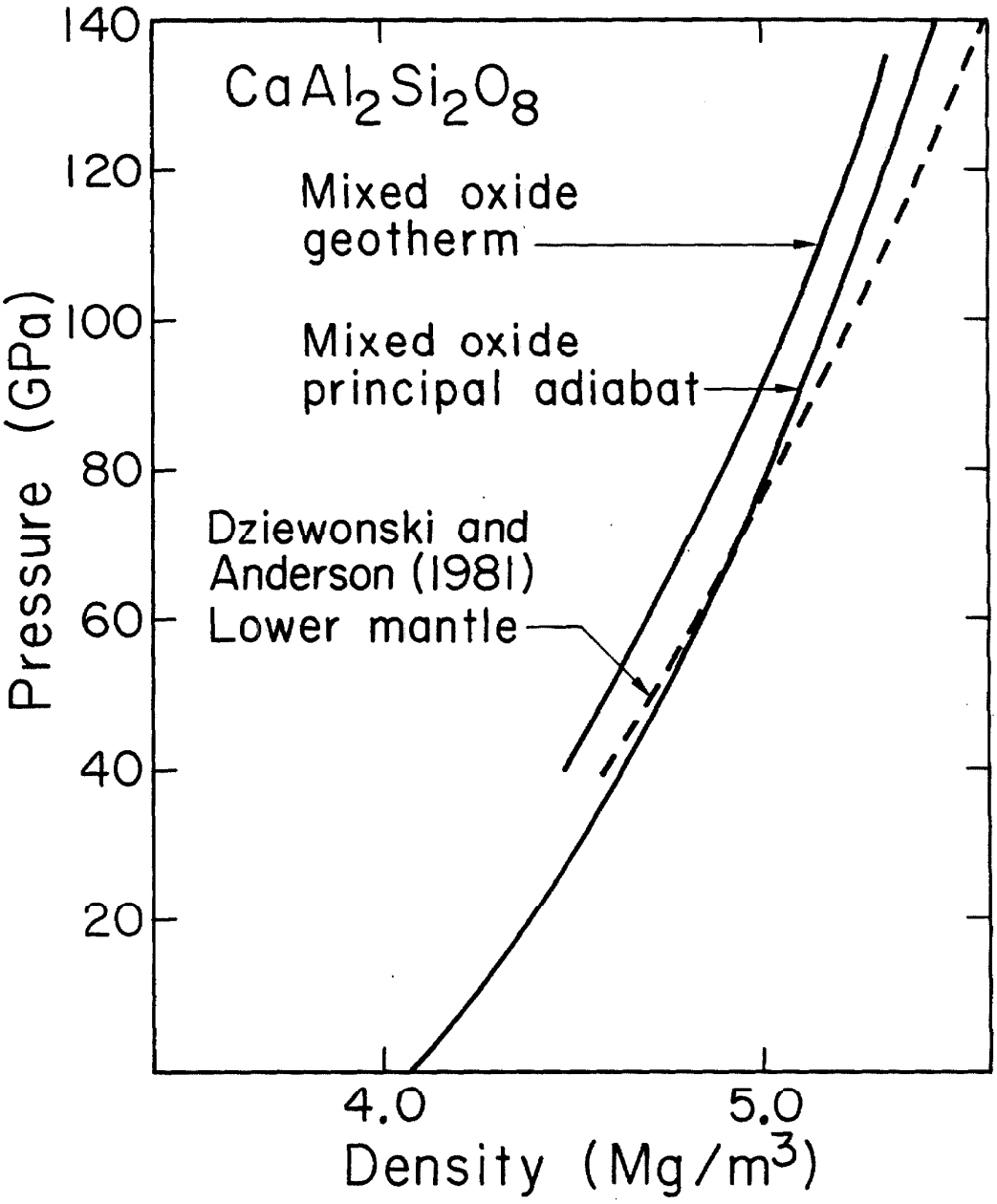

Fig. 3-12. Pressure as a function of density for the mixed oxide principal adiabat and geotherm (Stacy, 1977) compared to seismologically determined densities (Dziewonski & Anderson, 1981).

TJA83127SFD

Table 3-3

Apollo 15418 Hugoniot and Release Data

Shot	Flyer Material	Driver Material	Projectile Velocity (km/s)	Initial Density (Mg/m^3)	Shock Velocity (km/s)	Particle Velocity (Km/s)	Pressure (GPa)	Density (Mg/m^3)
LGG119	Ta	Ta	5.823 ± .005	2.8414 ± .0014	9.811 ± .060	4.397 ± .007	122.6 ± 0.6	5.149 ± .031
		Partial Release State (NaCl buffer)			9.838 ± .018	4.752 ± .014	101.2 ± 0.5	4.998 ± .033
LGG118	Ta	Ta	5.830 ± .005	2.8914 ± .0022	9.907 ± .035	4.380 ± .005	125.5 ± 0.4	5.183 ± .018
		Partial Release State (Graphite foam buffer)			9.170 ± .031	6.446 ± .024	63.9 ± 0.5	3.813 ± .032

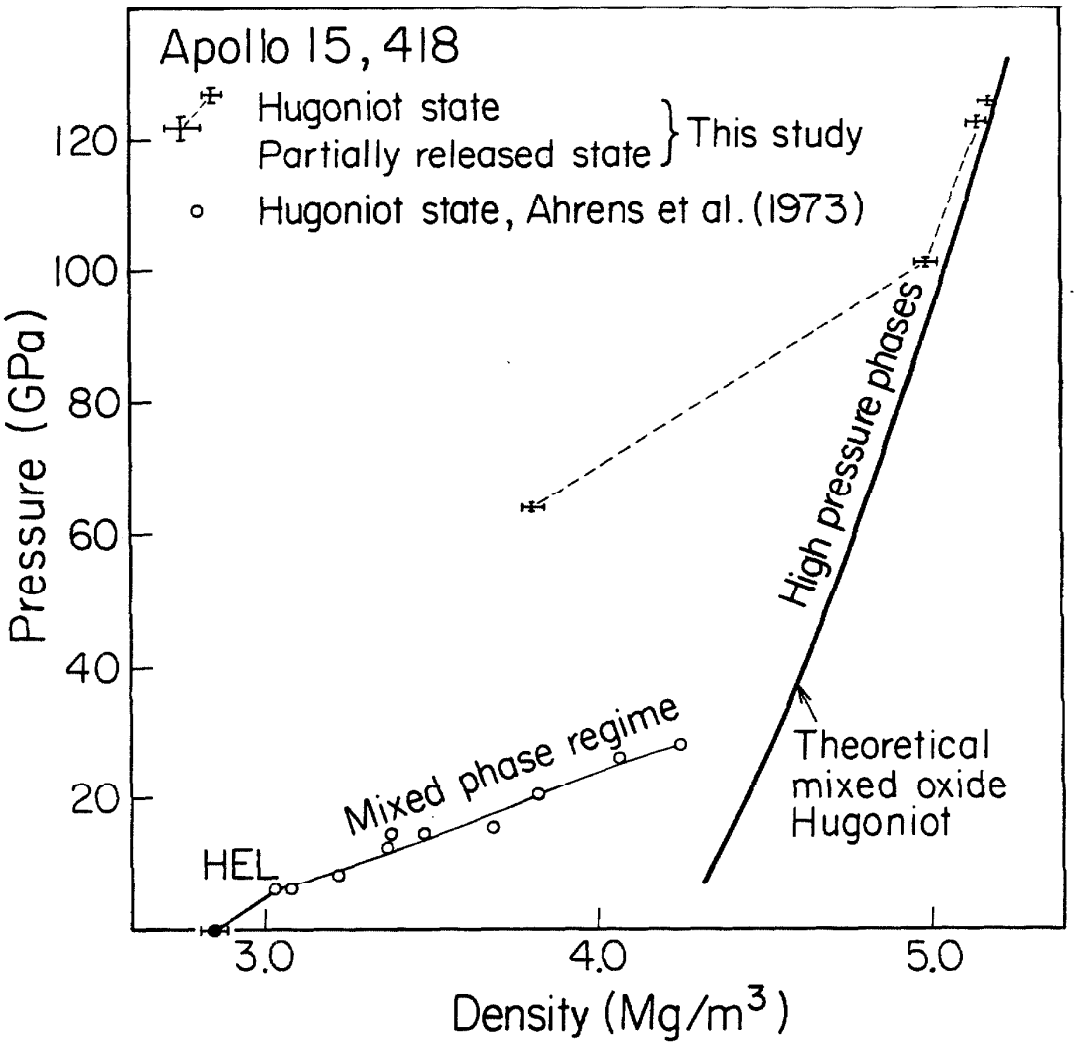

Fig. 3-13. Lunar gabbroic anorthosite Hugoniot and release data. Mixed oxide theoretical Hugoniot based on parameters in Table 3-4 gives good agreement with data. One partial release state was determined for each shock state, but because shock states are so close, the two partial release states outline an approximate release path.

enstatite (en_{84}) by Ahrens *et al.* (1973), taken from a microprobe analysis. In order to construct a theoretical mixed oxide Hugoniot for this rock, as was done for anorthite glass, we assumed the plagioclase fraction to be pure anorthite, due to our ignorance of the high-pressure behavior of Na_2O, and the observation that anorthite and albite have similar Hugoniots (McQueen *et al.*, 1976). The resulting mass fractions in the simplified model are .70 for anorthite ($CaAl_2Si_2O_8$), .19 for enstatite ($MgSiO_3$), and .11 for ferrosilite ($FeSiO_3$). These are broken down into their five component oxides (Table 3-4), and a high pressure adiabat and Hugoniot were constructed in the same manner as for anorthite glass. The theoretical Hugoniot constructed in this way is seen in Fig. 3-13 to give excellent agreement to the Hugoniot data, and to the initial slope of the measured release path. As in the case of pure anorthite, it is not likely that the lunar rock disproportionates into its component oxides at these pressures, but the mixed oxide model gives a good description of the bulk properties of whatever phases exist there. The second release datum indicates a large density decrease upon unloading, consistent with shock-vaporization of material. Entropy-gain calculations of Ahrens & O'Keefe (1977) and of Boslough & Ahrens (1983a) indicate that incipient vaporization may occur at shock pressures above 102 GPa for gabbroic anorthosite and above 92 GPa for anorthite, respectively. However, this is not observed in the release paths of shocked anorthite glass.

Table 3-4

Mixed Oxide Parameters - Lunar Gabbroic Anorthosite

	CaO (B2)	Al_2O_3 (Corundum)	SiO_2 (Stishovite)	MgO (B1)	FeO (B2)	Composite
ρ_o (g)	4.00	3.986	4.29	3.56	6.05	4.14
K_{os} (GPa)	121	250	306	170	195	219
K'_{os}	5.2	4.0	5.4	4.0	3.4	5.1
γ	1.80	1.32	1.38	1.3	1.8	1.44
n	1.0	1.0	3.2	1.0	1.25	1.8
E_{tr}(kJ/g)	2.1	0.0	0.8[a]	0.0	0.4	1.01[b]
m_i	.141	.257	.466	.076	.060	1.00
v_i	.154	.267	.450	.089	.041	1.00
References	(c)	(d)	(e)	(f)	(g)	

(a) Robie (1979)

(b) includes .35kJ/g energy of formation of anorthite and .35kJ/g energy of formation of enstatite from oxides (Robie, 1979)

(c) Boslough et al. (1983)

(d) Anderson (1976)

(e) Lyzenga et al. (1973)

(f) Vassiliou and Ahrens (1981)

(g) Jeanloz and Ahrens (1980)

Conclusions

The experimental Hugoniots of anorthite glass above 60 GPa and lunar gabbroic anorthosite at 120 GPa are well described by the Hugoniots calculated for their composite oxides, based on the individual properties of the oxides. The actual phases which are stable along the Hugoniot of anorthite, however, have larger energies of transformation. The zero pressure density of the mixed-oxide high pressure phase assemblage model is 4.07 Mg/m^3, and the zero-pressure bulk modulus is 228 GPa. These values are comparable to those for the lower mantle, indicating that $CaAl_2Si_2O_8$, or its high pressure reaction products, cannot be precluded as major components of the lower mantle on the basis of its equation of state. Such a refractory component could therefore be present in the lower mantle with a mass fraction in the range 0.12 to 0.16 as predicted by cosmochemical abundance considerations (Ross & Aller, 1976), or in greater concentrations as expected by inhomogeneous accretion models (Turekian & Clark, 1969).

Acknowledgments

We wish to thank E. Bus, E. Gelle, W. Ginn, M. Long and C. Manning for their excellent technical help. Support was provided by NASA NGL 5-002-105 and NSG 0019. This manuscript has been submitted to *Geophys. J. R. astr. Soc.* with co-authors Sally M. Rigden and Thomas J. Ahrens.

References

Ahrens, T. J. & Gregson, V. G., Jr., 1964. Shock compression of crustal rocks: data for quartz, calcite and plagioclase rocks, *J. Geophys. Res*, **69**, 4839-4874.

Ahrens, T. J. & Rosenberg, J. T., 1968. Shock metamorphism: experiments on quartz and plagioclase, in Shock Metamorphism of Natural Materials. B. M. French & W. M. Short eds. pp. 59-81, Mono Press, Baltimore, Md.

Ahrens, T. J., Peterson, C. F. & Rosenberg, J. T., 1969a. Shock compression of Feldspars, *J. Geophys. Res.*, **74**, 2727-2746.

Ahrens, T. J., Anderson, D. L. & Ringwood, A. E., 1969b. Equations of state and crystal structures of high-pressure phases of shocked silicates and oxides, *Rev. Geophys.*, **7**, 667-707.

Ahrens, T. J. & Liu, H.-P., 1973. A shock-induced phase change in orthoclase, *J. Geophys. Res.*, **78**, 1274-1278.

Ahrens, T. J., O'Keefe, J. D. & Gibbons, R.V., 1973. Shock compression of a recrystallized anorthositic rock from Apollo 15, *Proc. Lunar Sci. Conf. 4th*, 63-64.

Ahrens, T. J. & O'Keefe, J. D., 1977. Equations of state and impact-induced shock-wave attenuation on the moon, in Impact and Explosion Cratering. D. J. Roddy, R. O. Pepin, and R. B. Merrill eds. pp. 639-656. Pergamon Press, New York.

Anderson, D. L. & Hart, R. S., 1976. An earth model based on free oscillations and body waves, *J. Geophys. Res.*, **81**, 1461-1475.

Anderson, O. L., 1973. A scaling law for K'_o for silicates with constant mean

atomic mass, *Earth planet. Sci. Lett.*, **20**, 73-76.

Birch, F. & Bancroft, D., 1942. The elasticity of glass at high temperatures, and the vitreous basaltic substratum. *Am. J. Sci.*, **240**, 457-490.

Boslough, M. B. & Ahrens, T. J., 1983a. Shock-melting and vaporization of anorthosite and implications for an impact-origin of the moon, *Lunar and Planetary Science XIV.*

Boslough, M. B. & Ahrens, T. J., 1983b. Shock wave properties of anorthosite and gabbro, *J. Geophys. Res.*, submitted.

Boslough, M. B., Ahrens, T. J. & Mitchell, A. C., 1983a. Shock temperatures in anorthite glass, *Geophys. J. R. astr. Soc.*, submitted.

Boslough, M. B., Ahrens, T. J. & Mitchell, A. C., 1983b. Shock temperatures in CaO, *Geophys. J. R. astr. Soc.*, submitted.

Bridgeman, P. W., 1948. The compression of 39 substances to 100,000 kg/ cm^2, *Proc. Am. Acad. Arts Sciences*, **76**, 55-87.

Davies, G. F. & Gaffney, E. S., 1973. Identification of high-pressure phased of rocks and minerals from Hugoniot data, *Geophys. J. R. astr. Soc.*, **33**, 165-183.

Duvall, G. E. & Taylor, S. M., Jr., 1971. Shock parameters of a two component mixture, *J. Composite Materials*, **5**, 130-139.

Dziewonski, A. D. & Anderson, D. L., 1981. Preliminary reference earth model, *Phys. Earth Planet. Interiors*, **25**, 297-356.

Dziewonski, A. M., Hales, A. L., Lapwood, E. R., 1975. Parametrically simple earth models consistent with geophysical data, *Phys. Earth Planet. Interiors*, **10**, 12-48.

Grady, D. E., Murri, W. J. & DeCarli, P. S., 1975. Hugoniot sound velocities and

phase transformations in two silicates, *J. Geophys. Res.*, **80** 4857-4861.

Graham, R. A. & Brooks, W. P., 1971. Shock-wave compression of sapphire from 15 to 4000 kBar: The effects of large anisotropic compressions, *J. Phys. Chem. Solids*, **32**, 2311-2330.

Grossman, L. & Larimer, J. W., 1974. Early chemical history of the solar system, *Rev. Geophys. Space. Phys.* **12**, 71-101.

Jeanloz, R. & Ahrens. T. J., 1978. The equation of state of a lunar anorthosite: 60025, *Proc. 9th Lunar Planet. Sci. Conf.*, 2789-2803.

Jeanloz, R. & Ahrens, T. J., 1980. Anorthite: Thermal equation of state to high pressures, *Geophys. J. R. astr. Soc.* **62**, 529-549.

Liebermann, R. C., Ringwood, K. E., 1976. Elastic properties of anorthite and the nature of the lunar crust. *Earth Planet. Sci. Lett.*, **31**, 69-74.

Liu, L-G, 1978. A new high-pressure phase of $Ca_2Al_2SiO_7$ and implications for the earth's interior, *Earth planet. Sci. Lett.*, **40** 401-406.

Lyzenga, G. & Ahrens, T. J., 1978. The relations between the shock-induced free-surface velocity and post-shock density of solids, *J. appl. Phys*, **49**, 201-204.

Lyzenga, G. A. & Ahrens, T. J., 1979. A multi-wavelength optical pyrometer for shock compression experiments, *Rev. Sci. Instr.*, **50**, 1421-1424.

Lyzenga, G. A., Ahrens, T. J. & Mitchell, A. C., 1983. Shock temperatures of SiO_2 and their geophysical implications, *J. geophys. Res.*, **88**, 2431-2444.

Makishima, A. & MacKenzie, J. D., 1975. Calculation of bulk modulus, shear modulus and Poisson's ratio of glass. *J. Non. Cryst. Solids.*, **17**, 147-157.

McQueen, R. G., Marsh, S. P. & Fritz, J. N., 1967. Hugoniot equations of state of twelve rocks, *J. geophys. Res.*, **72**, 4999-5036.

Meister, R., Robertson, E. C., Werre, R. W. & Raspet, R., 1980. Elastic moduli of rock glasses under pressure to 8 kilobars and geophysical implications, *J. Geophys. Res.*, **85**, 6461-6470.

Rice, M. H., McQueen, R. G. & Walsh, J. M., 1958. Compressibility of solids by strong shock waves, *Solid State Phys.*, **6**, 1-63.

Robie, R. A., Hemingway, B. S. & Fisher, J. R., 1979. *Thermodynamic Properties of Minerals at 298.15 K and 1 Bar (10^5 Pascals) Pressure at Higher Temperatures*, Government Printing Office, Washington, D.C.

Ross, J. E. & Aller, L. H., 1976. The chemical composition of the sun, *Science*, **191**, 1223-1229.

Schroeder, J., Dunn, K.-J. & Bundy, 1981. Brillouin scattering from amorphous SiO_2 under hydrostatic pressure up to 133 kBar, General Electric Corporate Research and Development Report 81CRD216.

Schmitt, D. R. & Ahrens, T. J., 1983. Temperatures of shock-induced shear instabilities and their relationship to fusion curves, *Geophys. Res. Lett.*, in press.

Stacey, F. D., 1977. A thermal model of the earth, *Phys. Earth Planet. Interiors*, **15**, 341-341.

Turekian, K. K. & Clark, S. P., Jr., 1969. Inhomogeneous accretion model of the earth from the primitive solar nebula, *Earth planet. Sci. Lett.*, **6**, 346-348.

Vassiliou, M. S. & Ahrens, T. J., 1981. Hugoniot equation of state of periclase to 200 GPa, *Geophys. Res. Lett.*, **8**, 729-732.

Wackerle, J., 1962. Shock wave compression of quartz. *J. Appl. Physics.*, **33**, 922-937.

Watt, J. P., Davies, G. F. & O'Connell, R. J., 1976. The elastic properties of composite materials, *Rev. Geophys., Space Phys.*, **14**, 541-563.

Zamyshlyaev, B. V., Ciovorukha, E. A. & Shcherbatyuk, V. A., 1982. Polymorphic phase transformations in the presence of dynamical interactions. *Sov. Phys. Dokl.*, **27**, 324-326.

Chapter 4

Shock Wave Properties of Anorthosite and Gabbro

ABSTRACT

Shock wave experiments have been conducted in San Gabriel anorthosite to peak stresses between 5 and 11 GPa using a 40 mm-bore propellant gun. Particle velocities were measured directly at several points in each target by means of electromagnetic gauges. Hugoniot states were calculated by determining shock-transit times from the gauge records. Measured sound velocities indicate a loss of shear strength upon shock compression for both rocks, with the strength loss persisting upon release to zero stress. Sound velocities of anorthosite shocked to peak stresses between 6 and 10 GPa were measured to be between 5.1 and 5.3 upon release to zero stress. Stress-density release paths in the anorthosite indicate possible transformation of albite to jadeite + (quartz or coesite), with the amount of material transformed increasing from about .4 to .7 mass fraction as the shock stress increased from 6 to 10 GPa. Electrical interference effects precluded the determination of acurate release paths for San Marcos gabbro. Because of the loss of shear strength in the shocked state, the plastic behavior exibited by anorthosite indicates that calculations of energy partitioning due to impact onto planetary surfaces based

on elastic-plastic models may underestimate the amount of internal energy deposited in the impacted surface material.

Introduction

The plagioclase feldspar-bearing rocks anorthosite and gabbro are important components of the lunar and terrestrial crusts. It is necessary to understand the behavior of such rocks under high dynamic stress in order to model cratering processes which result from hypervelocity impacts, and to characterize the stress history of rocks which have been subject to shock loading on planetary surfaces such as the moon and in some meteorites. Shock-wave studies of these and similar materials have been conducted in the past (Ahrens *et al.*, 1969, McQueen *et al.*, 1967, Jeanloz and Ahrens, 1980, Boslough *et al.*, 1983a), but in these studies the data are limited to the Hugoniot state and in some cases a single state on the release isentrope. By employing particle-velocity gauges, a complete stress-strain history subsequent to shock-compression can be determined, along with sound velocity information (Fowles and Williams, 1970, Cowperthwaite and Williams, 1971, Seaman, 1974). Particle velocity experiments supply detailed release paths, which provide better constraint for mechanical properties and polymorphism than is available with Hugoniot experiments alone.

Peterson *et al.*, (1970) used particle velocity gauges to determine release paths of playa alluvium, tonalite, and novaculite shocked to stresses up to 5 GPa. They attributed high rarefaction velocities and steep release paths in the stress-density plane to irreversible compaction. Grady *et al.*, (1974) carried out experiments on polycrystalline quartz (novaculite) to 40 GPa using a

combination of particle velocity and manganin stress gauges to determine release adiabats and concluded that a partial quartz-stishovite transformation takes place above 15 GPa, with the quantity of material transformed an increasing function of peak stress, and that the Hugoniot states are not on the quartz-stishovite coexistence curve. Similar experiments were conducted on polycrystalline quartz and perthitic feldspar by Grady *et al.*, (1975) and Grady and Murri (1976), who used manganin stress gauges to determine Hugoniot sound velocities, and found that these rocks lose shear strength when shocked to pressures above 20 GPa. Larson and Anderson (1979) used particle velocity gauges to study limestone and tuff at lower stress levels (4 GPa), and attributed the observed time-dependent behavior to the closing of pores in these rocks.

In this paper we present new Hugoniot data on San Gabriel anorthosite and San Marcos gabbro to 11 GPa. Release paths in the stress-density plane and sound velocities are reported, as determined from particle velocity data.

Experimental Methods

San Gabriel anorthosite samples were collected in the San Gabriel Mountains near Pasadena, California. This rock is highly variable in composition and texture and has been studied in detail by Carter (1982). The particular specimen used in these experiments had randomly oriented plagioclase crystals with a mean grain size of 1-2 mm. Significant alteration was observed at grain boundaries, and the composition is given in Table 4-1; determined with a petrographic microscope. An electron microprobe analysis indicated a composition of An_{38} for the plagioclase component.

Table 4-1

San Gabriel Anorthosite Composition

Mineral	Volume %
Plagioclase *	91
White Mica	6
Epidate	3
Opaques	trace
Quartz	trace
Apatite	trace

* An_{40}

(Analysis by S. Rigden)

The San Marcos gabbro was obtained near Escondido, California, and has been studied petrologically by Miller (1937). Samples from the same specimen used in this study were used in impact and in spall-strength experiments by Lange *et al.*, (1983). The composition is tabulated in Table 4-2. Rock samples were cut into 1.5 mm thick, 3.2 by 4.5 cm rectangular slabs, and were bonded together with epoxy, with a U-shaped copper particle-velocity gauge at each interface and one at the free surface. Gauges were photo-etched from 10 μm thick copper foil with a 12.5 μm polyamide (kapton) film backing. Targets were shock-loaded by impact of flat-faced polycarbonate (Lexan) projectiles fired from a 40-mm bore propellant gun at velocities from 1.4 to 2.4 km/s. Projectile velocities were determined using a laser intervalometer (Ahrens *et al.*, 1971).

A uniform magnetic field at right angles to each gauge and to its direction of motion was supplied by a set of Helmholtz coils. An electromotive force V(t) was induced across the gauge element due to its motion through the field

$$V(t) = BLu_p(t) \qquad (4\text{-}1)$$

where B is the magnetic field (≈1.8 kG), L is the effective gauge length (≈1 cm), and $u_p(t)$ is the gauge velocity; equal to the particle velocity of the surrounding medium. These signals were recorded by an array of cathode ray oscilloscopes. The experiment is shown schematically in Fig. 4-1 and described in detail in Appendix IV.

The geometry and time history of a typical experiment is illustrated by means of an x-t diagram in Fig. 4-2. The stationary rock target lies to the right of the origin, with four particle velocity gauges initially at intervals of 1.5 mm. The polycarbonate projectile approaches from the left and strikes the x=0

Table 4-2

San Marcos Gabbro Composition

Mineral	Volume %
Plagioclase	67.9
Amphibole	22.5
Clinopyroxene	1.5
Orthopyroxene	1.1
Quartz	1.4
Biotite	0.9
Opaques	4.3
Alakali feldspar	trace
Calcite	trace
Chlorite	trace
Apatite	trace

(Analysis by R. Hill)

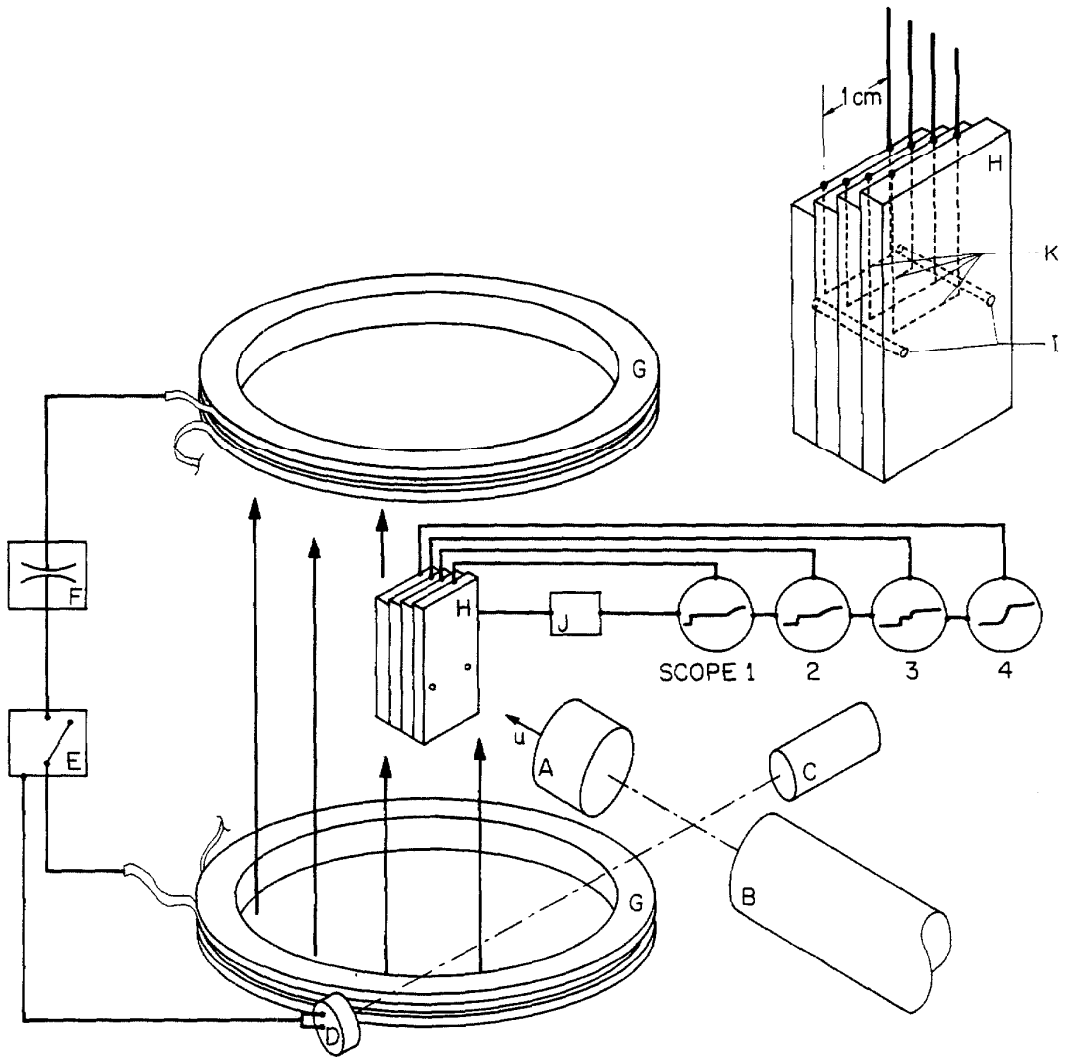

Fig. 4-1. Schematic drawing of particle velocity experiment, with major components indicated: A. Polycarbonate projectile, B. 40 mm-bore gun barrel, C. Timing laser, D. Photodectector, E. High-power switch (ignition), F. Capacitor bank, G. Helmholtz coils, H. Rock target, I. Self-shorting trigger pins, J. Fiducial pulse generator, K. Copper foil particle velocity gauge elements.

TJA83132SFD

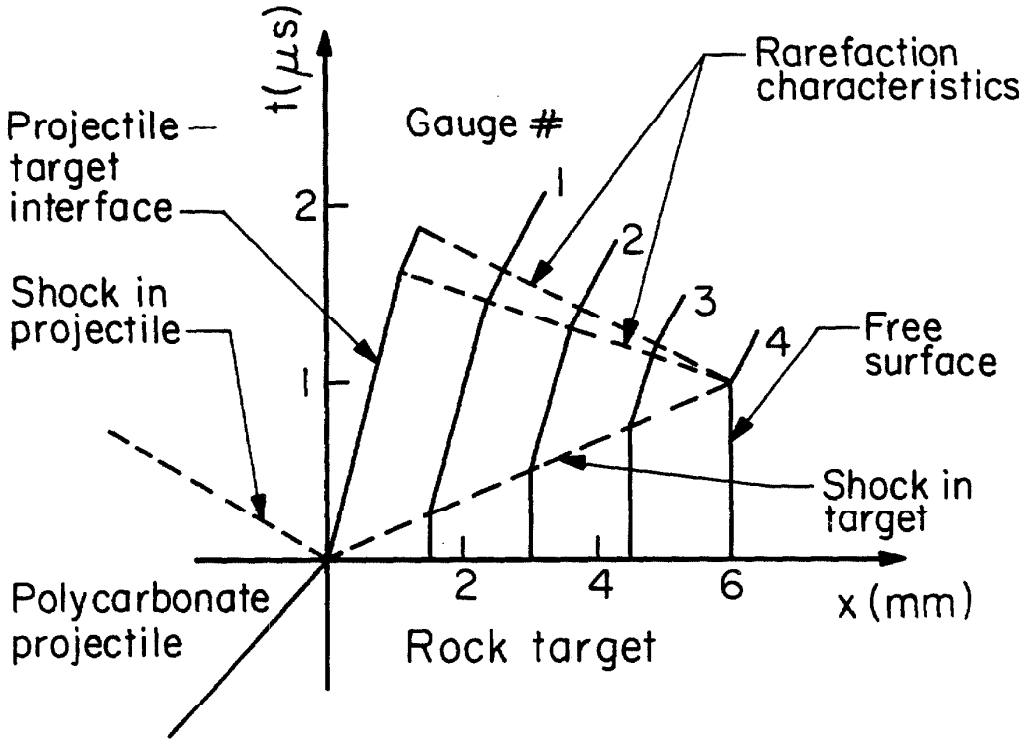

Fig. 4-2. Particle velocity experiment represented by x-t diagram. Projectile approaches stationary target from left and impacts at t=0.

TJA83133SFD

surface of the target at time t=0, driving a shock wave to the right into the rock and to the left into the projectile. Each gauge is stationary until overtaken from the left by the shock wave, at which time it begins moving with the particle velocity associated with the Hugoniot state. The shock wave reflects from the free surface as a rarefaction wave, and each gauge again accelerates to the right as this wave passes through it from the right.

Results

Typical particle velocity records for shocked anorthosite and gabbro are shown in Fig. 4-3. The sudden increase corresponds to shock wave arrival, and the second increase corresponds to the acceleration from free-surface rarefaction. The gabbro records were found to be significantly noisier than the anorthosite records in all cases. This was presumed to result from the presence of piezoelectric quartz grains in the gabbro, whereas the anorthosite was relatively free of quartz.

Digitized oscilloscope records for anorthosite shocked to 10 GPa are shown in Fig. 4-4. Synchronization of the four signals in time was achieved by means of a fiducial pulse received simultaneously at each oscilloscope. Shock-transit times were taken from the interval between arrival at different gauges and were used to determine shock velocity. The known projectile velocity and polycarbonate Hugoniot (Marsh, 1980) were used with an impedance-match solution (McQueen *et al.*, 1970) to determine the Hugoniot states achieved in the rocks. Eulerian sound velocities were determined from the transit time of the free-surface rarefaction front and the Hugoniot density. Hugoniot states and sound velocities for both rocks are given in Tables 4-3 and 4-4.

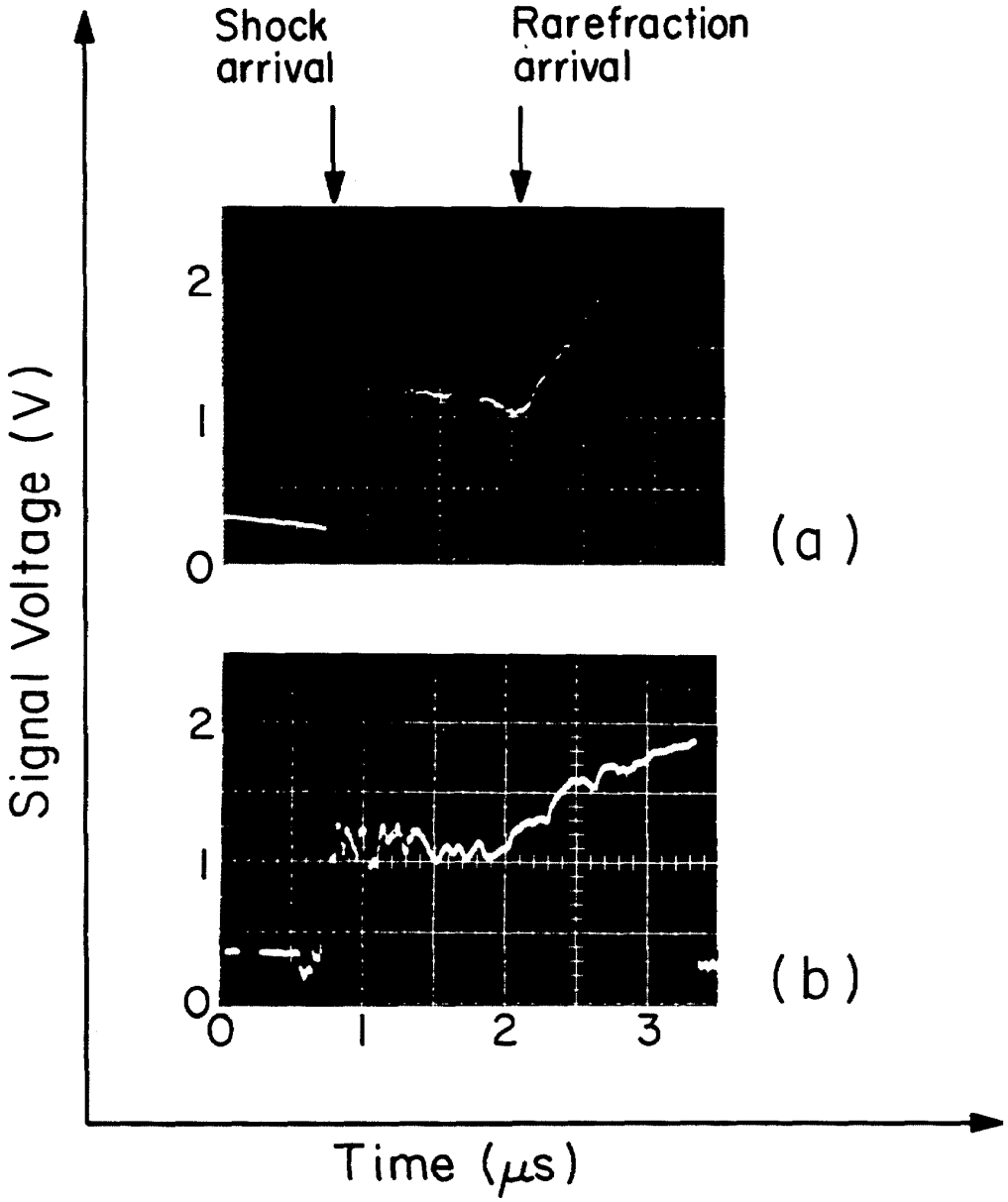

Fig. 4-3. Oscillograms of particle velocity-time profiles in (a) anorthosite and (b) gabbro. Gabbro signals are significantly noisier, presumably due to presence of quartz grains.

TJA83134SFD

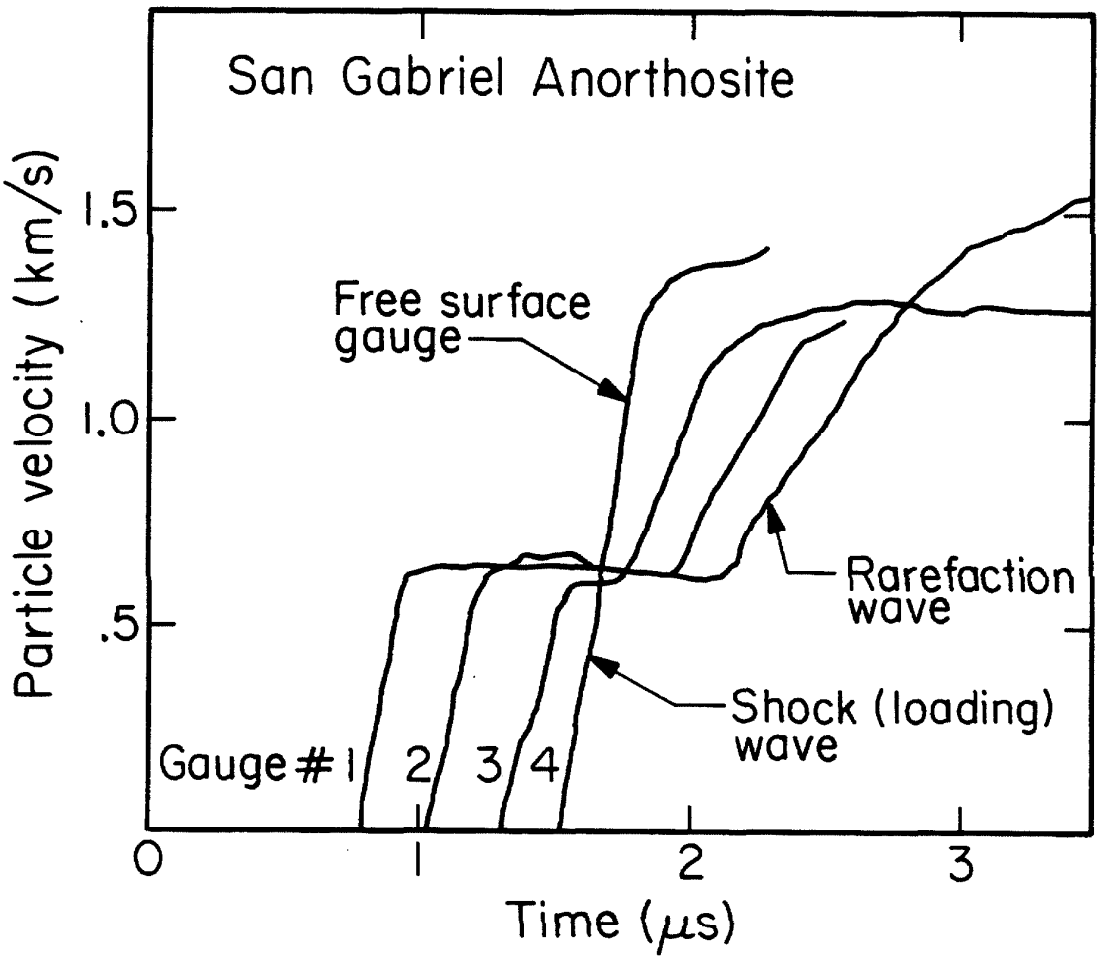

Fig. 4-4. Digitized particle velocity gauge records from experiment 40-571 in which anorthite was shocked to 10 GPa.

TJA83135SFD

Table 4-3

San Gabriel Anorthosite Shock Wave Data

Shot	Projectile Velocity (km/s)	Initial Density (Mg/m^3)	Shock Velocity (km/s)	Particle Velocity (km/s)	Pressure (GPa)	Density (Mg/m^3)	Sound Velocity (km/s)
40-572	1.575 ±.050	2.656 ±.013	5.648 ±.055	.394 ±.022	5.91 ±.31	2.855 ±.011	6.90 ±.36
40-570	1.881 ±.050	2.653 ±.007	5.725 ±.117	.493 ±.020	7.47 ±.28	2.903 ±.014	7.59 ±.10
40-571	2.351 ±.050	2.653 ±.007	5.985 ±.032	.644 ±.020	10.23 ±.30	2.973 ±.011	8.39 ±.44

Table 4-4

San Marcos Gabbro Shock Wave Data

Shot	Projectile Velocity (km/s)	Initial Density (Mg/m^3)	Shock Velocity (km/s)	Particle Velocity (km/s)	Pressure (GPa)	Density (Mg/m^3)	Sound Velocity (km/s)
40-569	1.394 ±.009	2.907 ±.008	6.487 ±.035	.286 ±.011	5.39 ±.20	3.041 ±.004	6.5 ±.1
40-573	1.968 ±.006	2.886 ±.001	6.11 ±.30	.474 ±.016	8.36 ±.14	3.129 ±.022	8.5 ±.4
40-555	2.187 ±.050	2.892 ±.007	6.66 ±.19	.515 ±.020	9.91 ±.34	3.135 ±.015	--- ---
40-556	2.242 ±.032	2.929 ±.039	6.898 ±.042	.515 ±.048	10.41 ±.0.84	3.165 ±.020	7.0 ±.5
40-574	2.418 ±.025	2.874 ±.049	6.404 ±.016	.608 ±.052	11.19 ±.77	3.176 ±.026	6.7 ±.5

The observed release waves are nonsteady simple waves and can be inverted to stress-density release paths by numerically integrating the equations for conservation of mass and linear momentum (Cowperthwaite and Williams, 1971)

$$\left[\frac{\partial \rho}{\partial u_p}\right]_h = \frac{\rho^2}{\rho_o C(u_p)} \tag{4-2}$$

$$\left[\frac{\partial \sigma}{\partial u_p}\right]_h = \rho_o C(u_p) \tag{4-3}$$

where ρ is the density, ρ_o is the initial density, σ is the stress, u_p is the particle velocity, and h is the Lagrangian space coordinate along the direction of wave propagation. The Lagrangian sound velocity is determined by the finite difference approximation

$$C(u_p) \approx \frac{\Delta h}{\Delta t} \tag{4-4}$$

where Δh is the initial distance between gauges and Δt is the transit time for a disturbance with particle velocity u_p. In the case of anorthosite, the release paths are smooth and single-valued (Fig. 4-4). The oscilloscope records were digitized and integrated directly. The resulting release paths are consistent, and are plotted in Fig. 4-5. Because of the noisiness of the gabbro records (Fig. 4-3b), it was necessary to approximate the rarefaction waves by smooth curves before integrating. Complete release paths were not obtained (Fig. 4-6), and the partial release paths are less consistent than those of anorthosite. Eulerian sound speeds, equal to $\frac{\rho_o}{\rho} C(u_p)$, were also calculated for the release paths in both rocks. These are plotted as a function of stress in Figs. 4-7 and 4-8.

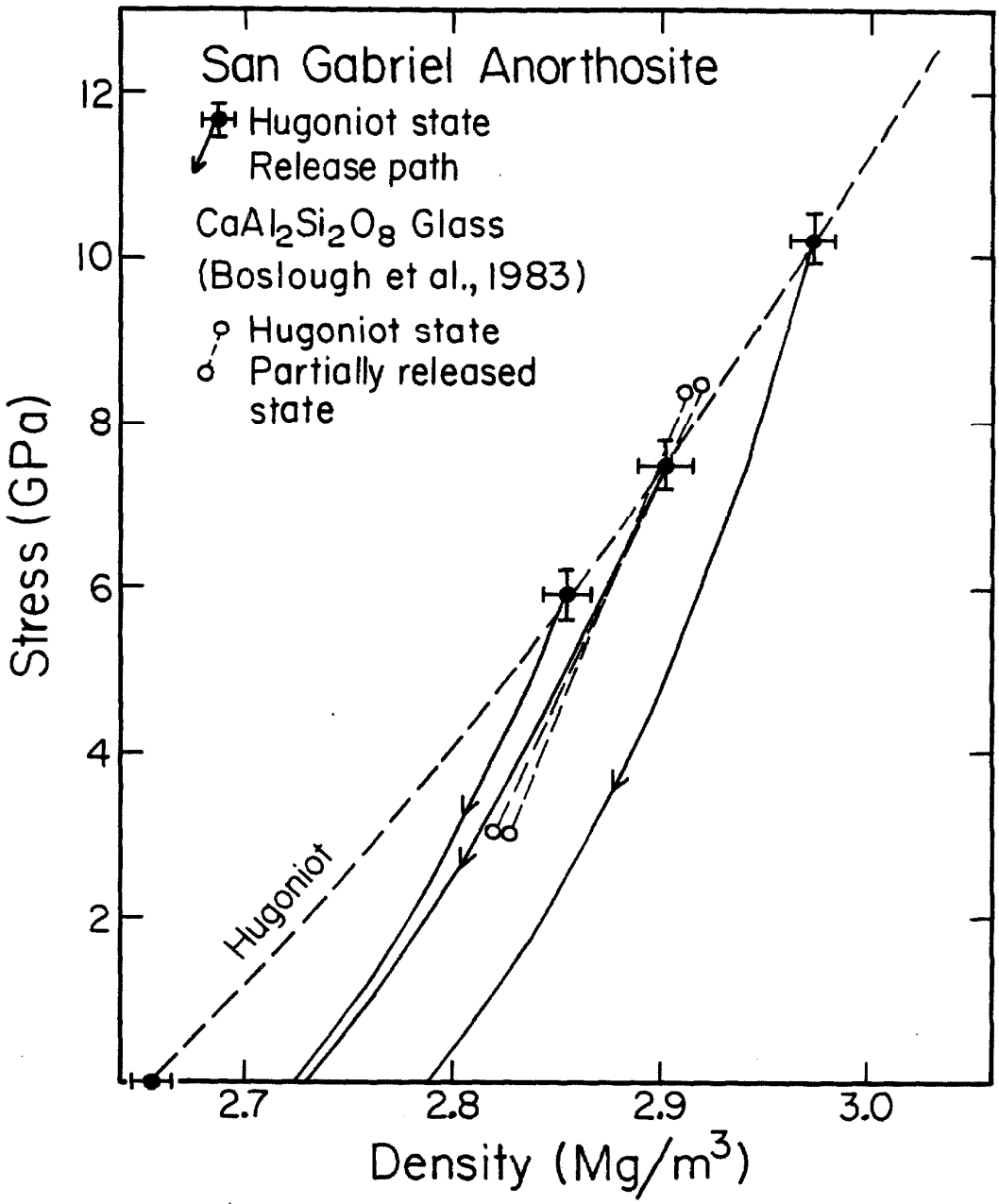

Fig. 4-5. Hugoniot states and release paths of San Gabriel anorthosite. Included are two Hugoniot states of anorthite glass (Boslough *et al.*, 1983), with respective partial release states.

TJA83136SFD

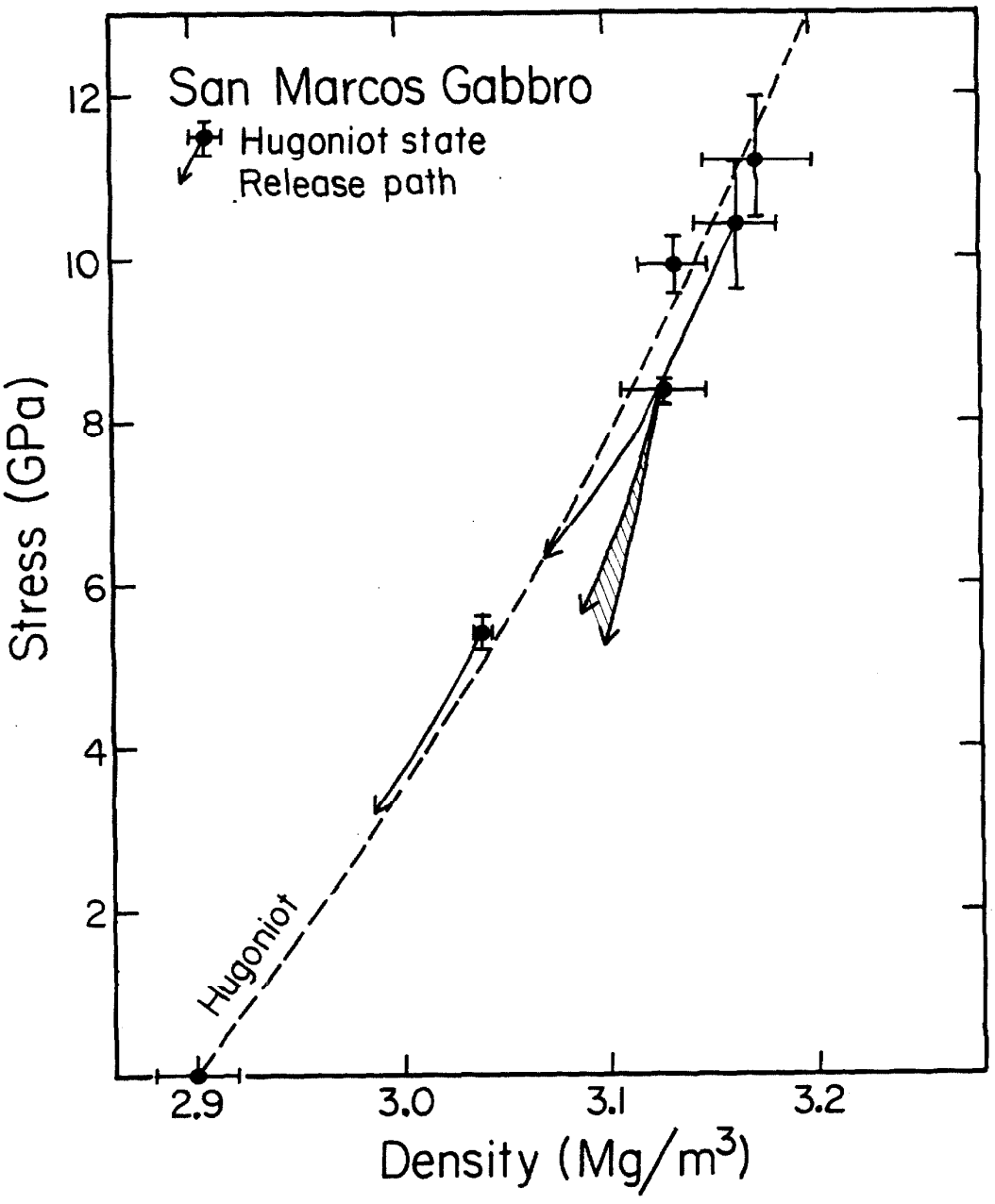

Fig. 4-6. Hugoniot states and partial release paths of San Marcos gabbro. Noisy particle velocity records precluded determination of release to zero stress.

TJA83137SFD

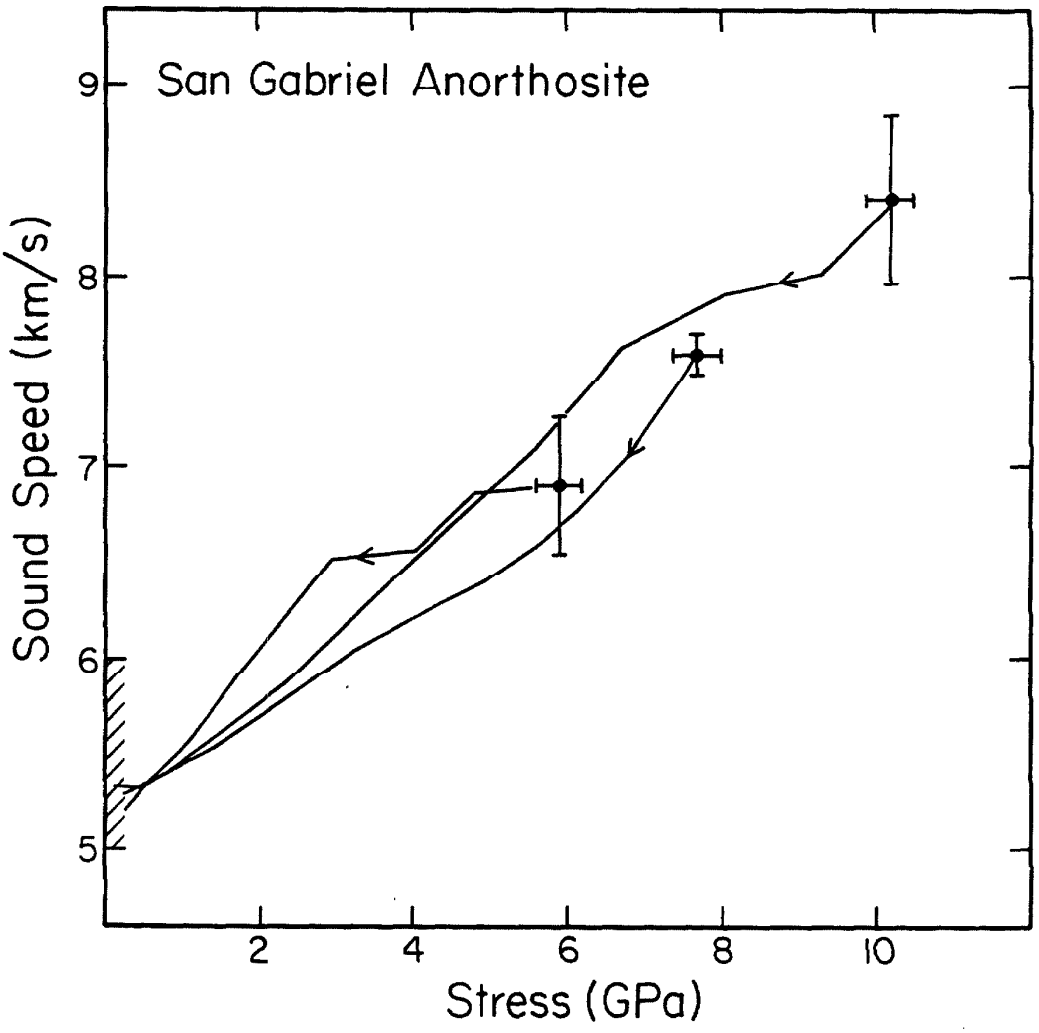

Fig. 4-7. Eulerian sound speeds along release paths of shocked San Gabriel anorthosite. Hatched region indicates range of possible zero pressure bulk sound velocities.

TJA83138SFD

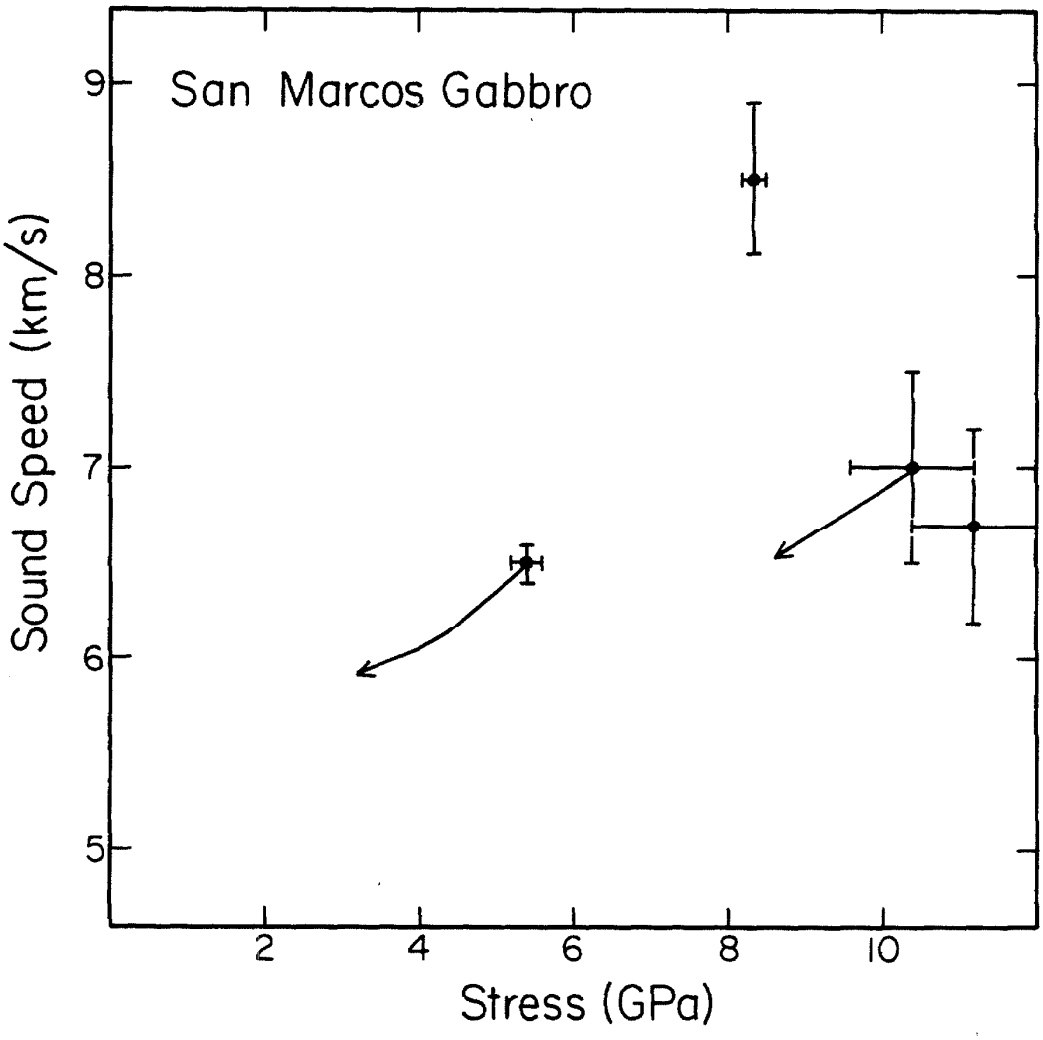

Fig. 4-8. Eulerian sound speeds of shocked San Marcos gabbro.

TJA83139SFD

Discussion

Sound velocities of anorthosite from this study can be compared to those measured ultrasonically for anorthosite rocks of similar composition (Birch, 1960, Birch, 1961, Simmons, 1964, Anderson and Liebermann, 1968, Liebermann and Ringwood, 1976). At T = 25°C and P > 0.4 GPa, longitudinal velocities have been measured in anorthosite with composition between An_{49} and An_{56} in the range $6.76 \geq v_p \geq 7.47$ km/s, and shear velocities in the range $3.87 \leq v_s \leq 4.09$ km/s. Bulk sound velocities,

$$v_\varphi^2 = v_p^2 - \frac{4}{3}v_s^2 \qquad (4\text{-}5)$$

are therefore in the range $5.04 \leq v_\varphi \leq 5.99$ km/s. Fig. 4-6 demonstrates that in all three shock wave experiments, the sound velocity approaches 5.2 km/s as the rock releases to zero pressure, indicating a loss of shear strength upon shock compression which is never regained. This is analogous to observations by Grady *et al.*. (1975) for polycrystalline quartz, where the loss of strength in that material was attributed to heterogeneous partitioning of shock energy into "shear bands" in which melting occurs. Optical observations consistent with this theory have been made for various minerals by Kondo and Ahrens (1983), and for anorthite glass by Schmitt and Ahrens (1983).

Not as clear a case can be made for the loss of shear strength in gabbro, due to the lower quality of the data. However, in most of the experiments the measured sound velocities are consistently lower for the gabbro than for the anorthosite.

Release paths for anorthosite, illustrated in Fig. 4-5, are significantly steeper than the Hugoniot. Similar release behavior was observed in anorthite glass (initial density = 2.69 Mg/m^3) by Boslough *et al.*. (1983b). The reason for the densification of the glass upon release was attributed to irreversible compaction of the amorphous material behind the shock wave to a denser form. Partial release paths can be extrapolated to the anorthite single crystal density of 2.76 Mg/m^3. This argument cannot be used to explain the release behavior of anorthosite, however. The phase transformation: $NaAlSi_3O_8$ (albite) → $NaAlSi_2O_6$ (jadeite) + SiO_2 (quartz or coesite) is a more reasonable explanation, particularly in light of the identification of shock-induced formation of jadeite from oligoclase in material from the Ries Crater in Germany (James, 1969). The assemblage $(anorthite)_{38}$ + $(jadeite + quartz)_{62}$ has a density of 3.01 Mg/m^3, and $(anorthite)_{38}$ + $(jadeite + coesite)_{62}$ has a density of 3.06 Mg/m^3. At 293°K, $NaAlSi_2O_6 + SiO_2$ are the stable phases above 0.6 GPa (Clark, 1966). The present experiments are well above the transformation pressure, so the only barriers to the phase transition are kinetic. The zero pressure density of the released anorthosite can be used to estimate the amount of material transformed. For example, the final densities are in the range 2.72 to 2.79 Mg/m^3, which requires the transformation of from 42 to 73% of the albite to high pressure phases. The possibility of pore-space crushing and irreversable compaction would bring this estimate down somewhat. It is clear from the data that the fraction of albite transformed to high pressure phases is an increasing function of peak stress. This result is analogous to the conclusion of Grady *et al.*, (1974) for higher pressures that the release path of shocked polycrystalline quartz is controlled by the quartz → stishovite transition. The release data for

gabbro, plotted in Fig. 4-7, are not of good enough quality to resolve whether the release paths are above or below the Hugoniot.

Conclusions

San Gabriel anorthosite loses shear strength upon shock to pressures greater than 6 GPa. Because strength effects can probably be neglected in this material, its release behavior can be attributed to the phase transformation of albite to jadite and quartz or coesite. The amount of material transformed is controlled by kinetics, and is an increasing function of shock pressure. This may be due to the localization of shock heating into shear bands, in which the temperature is high enough for the phase transition to occur. The mechanical result of the shear banding is plastic behavior upon release.

In calculations by O'Keefe and Ahrens (1977) of energy partitioning of a hypervelocity impact onto the surface of a planet, the release behavior of rocks was assumed to be elastic-plastic (Fowles, 1960, Davison and Graham, 1979). This assumption over-estimates the attenuation of the shock wave due to catch-up of the rarefaction wave from the free surface of the impacting body, because the assumed sound velocities are higher than they actually are for plastic behavior, as determined in this study. Thus a larger quantity of surface material is shocked above a given pressure, and estimates by O'Keefe and Ahrens (1977) of the fraction of meteoroid kinetic energy deposited in the planetary surface material will be too low.

Acknowledgements

We appreciate the assistance of E. Gelle, W. Ginn, J. Long, and M. Long in building and carrying out experiments. We thank R. Heuser, R. Hill, and S. Rigden for analyzing rock samples, and S. Sondergaard for help in fabricating gauges. This work was supported under NASA Grant NGL 05-002-105, and Defense Nuclear Agency Contract 001-82-C-0302. This manuscript has been submitted to *J. Geophys. Res.* with co-author Thomas J. Ahrens.

References

Ahrens, T.J., C.F. Petersen, and J.T. Rosenberg, Shock compression of feldspars, *J. Geophys. Res.*, *74*, 2727-2746, 1969.

Ahrens, T.J., J.H. Lower, and P.L. Lagus, Equation of state of fosterite, *J. Geophys. Res.*, *76*, 518-528, 1971.

Anderson, O. L., and R. C. Leibermann, Sound velocities in rocks and minerals: experimental methods, extrapolations to very high pressures, results, in: *Physical Acoustics IVB*, edited by W P. Mason, pp. 330-472, Academic Press, New York, 1968.

Birch, F., The velocity of compressional waves in rocks to 10 kilobars, 1, *J. Geophys. Res.*, *45*, 1083-1102, 1960.

Birch, F., The velocity of compressional waves in rocks to 10 kilobars, 2, *J. Geophys. Res.*, *66*, 2199-2224, 1961.

Boslough, M. B., T. J. Ahrens, and A. C. Mitchell, Shock temperatures in anorthite glass, *Geophys. J. R. astr. Soc.*, submitted, 1983a.

Boslough, M. B., S. M. Rigden, and T. J. Ahrens, Hugoniot equation of state of anorthite glass and lunar anorthosite, *Geophys. J. R. astr. Soc.*, submitted, 1983b.

Carter, B. A., Field petrology and structural development of the San Gabriel anorthosite-syonite body, Los Angeles County, California, in: *Geologic Excursion in the Transverse Ranges*, edited by J. D. Cooper, pp. 1-47, Geological Society of America, 1982.

Clark, S. P., Jr., High-pressure phase equilibria, in: *Handbook of Physical Constants*, edited by S. P. Clark, Jr., pp. 345-883, Geological of America,

New York, 1966.

Cowperthwaite, M., and R. F. Williams, Determination of constitutive relationships with multiple gages in nondivergent flow, *J. Appl. Phys.*, *42*, 456-462, 1971.

Davison, L. and R. A. Graham, Shock compression of solids, *Physics Reports*, *55*, 255-379, 1979.

Dremin, A. N., and K. K. Shvedov, The determination of Chapman-Jouguet pressure and of the duration of reaction in the detonation wave of high explosives, *Zh. Prikl, Mekh. Tekh. Fiz.*, *2*, 154-159, 1964.

Fowles, G. R., Attenuation of the shock wave produced in a solid by a flying plate, *J. Appl. Phys. 31*, 655-661, 1960.

Fowles, R., and R. F. Williams, Plane stress wave propagation in solids, *J. Appl. Phys.*, *41*, 360-363, 1970.

Grady, D. E., W. J. Murri, and G. R. Fowles, Quartz to Stishovite: wave propagation in the mixed phase region, *J. Geophys. Res.*, *79*, 332-338, 1974.

Grady, D. E., W. J. Murri, and P. DeCarli, Hugoniot sound velocities and phase transformations in two silicates, *J. Geophys. Res.*, *80*, 4857-4861, 1975.

Grady, D. E., and W. J. Murri, Dynamic unloading in shock compressed feldspar, *Geophys. Res. Lett.*, *80*, 472-474, 1976.

Grady, D. E., Shock deformation of brittle solids, *J. Geophys. Res.*, *85*, 913-914, 1980.

James, O. B., Jadeite: shock-induced formation from oligoglase, Ries Crater, Germany, *Science*, *165*, 1005-1008, 1969.

Jeanloz, R., and T. J. Ahrens, Anorthite: Thermal equation of state to high pressures, *Geophys. J. R. astr. Soc.*, *62*, 529-549, 1980.

Kondo, K. and T. J. Ahrens, Heterogeneous shock-induced thermal radiation in minerals, *Phys. Chem. Minerals*, *9*, 173-181, 1983.

Lange, M., T. J. Ahrens, and M. B. Boslough, Impact cratering and spall fracture of gabbro, *Icarus*, submitted, 1983.

Larson, D. B., and G. D. Anderson, Plane shock wave studies of porous geologic media, *J. Geophys. Res.*, *84*, 4592-4600, 1979.

Liebermann, R. C., and A. E. Ringwood, Elastic properties of anorthite and the nature of the lunar crust, *Earth Planet. Sci. Lett.*, *31*, 69-74, 1976.

Marsh, S. P., *LASL Shock Hugoniot Data*, 680 pp., University of California Press, Berkeley, 1980.

McQueen, R. G., S. P. Marsh, and J. N. Fritz, Hugoniot equation of state of twelve rocks, *J. Geophys. Res.*, *72*, 4999-5936, 1967.

McQueen. R. G., S. P. Marsh. J. W. Taylor, J. N. Fritz, and W. J. Carter, The equation of state of solids from shock wave studies, in *High Velocity Impact Phenomena*, edited by R. Kinslow, pp. 294-419, Academic Press, New York, 1970.

Miller, F. S., Petrology of the San Marcos gabbro, Southern California, *Bull. Geol. Soc. Amer.*, *48*, 1397-1426, 1937.

O'Keefe, J. D. and T. J. Ahrens, Impact-induced energy partioning, melting, and vaporization on terrestrial planets, *Proc. Lunar Sci. Conf. 8th*, 3357-3374, 1977.

Peterson, C. F., W. J. Murri, and M. Cowperthwaite, Hugoniot and release-adiabat measurements for selected geologic materials, *J. Geophys. Res.*, *75*, 2063-2072, 1970.

Rice, M. H., R. G. McQueen, and J. M. Walsh, Compressibility of solids by strong

shock waves, *Solid State Phys.*, *6*, 1-63, 1958.

Schmitt, D. R., and T. J. Ahrens, Temperatures of shock-induced shear instabilities and their relationship to fusion curves. *Geophys. Res. Lett.* in press, 1983.

Seaman, L., Lagrangian analysis for multiple stress or velocity gages in attenuating waves, *J. Appl. Phys.*, *45*, 4303-4314, 1974.

Simmons, G., Velocity of shear waves in rocks to 10 kilobars, 1, *J. Geophys. Res.*, *69*, 1123-1130, 1964.

Appendix I

Wide-Band Optical Pyrometer Design

The wide-band optical pyrometer is the temperature-measuring portion of the shock temperature-equation of state combination experiment at Caltech. It was designed with the intention of giving up some of the spectral- and time-resolution available with the six-channel narrow-band pyrometer (Lyzenga and Ahrens, 1979) in exchange for increased sensitivity. It is over two orders of magnitude more sensitive in spectral radiance than the narrow-band pyrometer, and can be used to measure temperatures lower than 2500°K without preamplification of the signals. At the same time, the loss of spectral- and temporal-resolution appears to be negligible in terms of data quality. Sensativity might in fact be further increased by using even wider-band filters.

The description of the optical pyrometer will proceed in the direction of light flow, beginning with the target assembly (Figs. 1-1, 3-3). Samples are transparent solids about 17 mm in lateral dimension and about 3 mm thick. Both surfaces are lapped to optical quality, and the samples are glued to flat metallic driver plates with epoxy. Great care is taken to minimize the gap between driver plate and target, and it is generally on the order of one micron according to measurements made by counting visible fringes with an optical flat. In some cases the contact surface of the sample is silvered before attaching to the driver plate in order to mask any flash which might occur when the shock wave transits the gap.

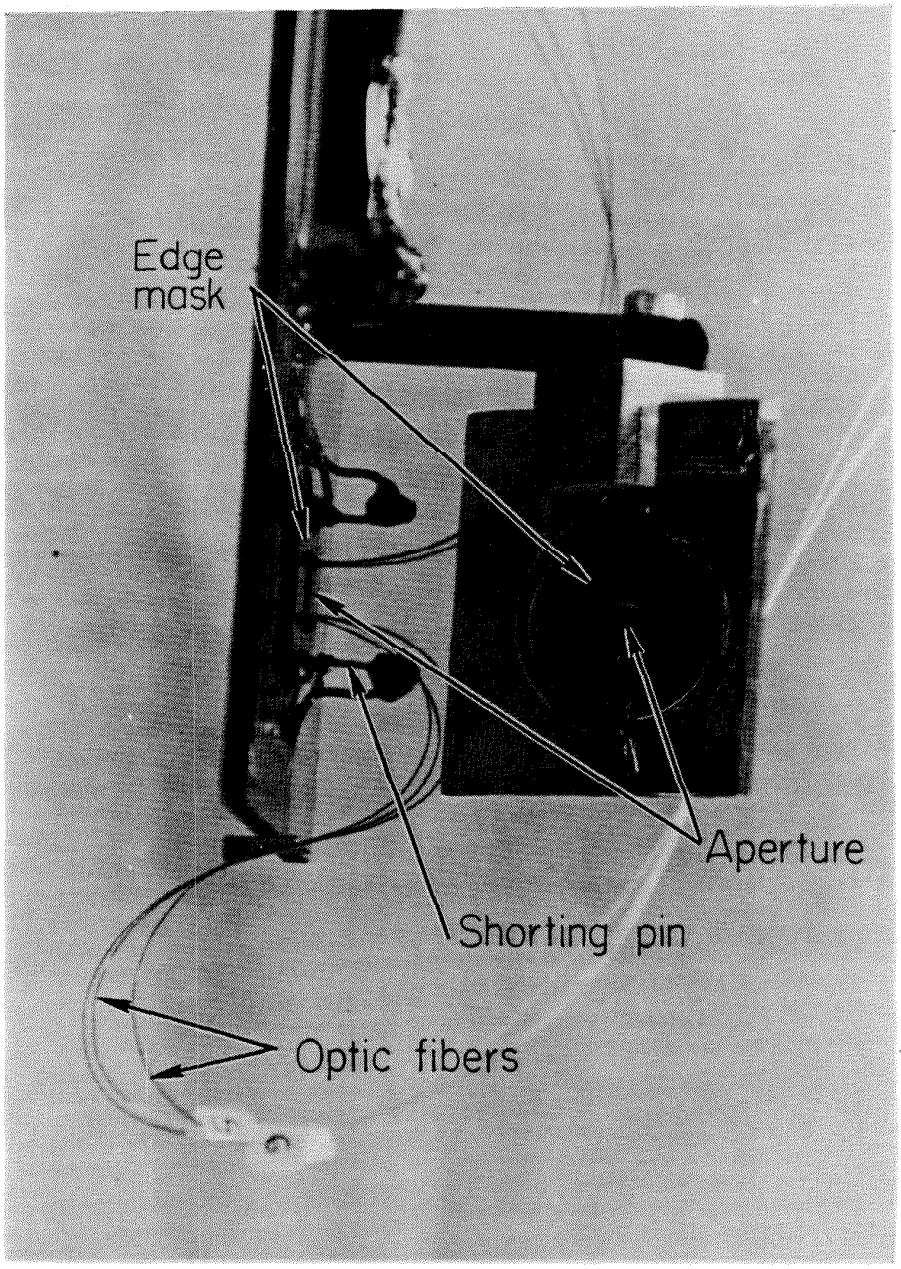

Fig. I-1. Photograph of shock-temperature target assembly from direction of pyrometer. Aperture (6.35 mm diameter) in edge mask can be seen in reflection in turning mirror. Optical fibers carry light pulse to streak camera.

The driver plates are the same as those used in standard equation of state experiments. They are circular disks 35 mm in diameter and 2.0 mm thick. and are mounted on the same target assembly, in the same manner as the standard experiment. As in the standard experiment, shorting pins are used to generate a triggering pulse. Two pins are mounted on the driver plate 9 mm above and below the center point so as not to block light radiated from the sample. The pins protrude through holes drilled in the driver plate, so the projectile reaches them about 200 ns before it collides with the target. The pins act as high speed switches which short upon impact. They are biased at 335 V, and when they close, a pulse is sent to the triggering circuits of the oscilloscopes and streak camera.

Because the field of view of the pyrometer is greater than the diameter of the sample, it is necessary that the edges be masked. It is also important that the outer portions of the sample, where edge effects (two-dimensional flow) might occur must also be masked from view. For this reason an aluminum edge-mask is attached to the free surface of the sample. A circular hole, 6.35 mm in diameter, and concentric with the axis of the driver plate (which is aligned with the gun barrel) is the only path by which light can get to the pyrometer. The edge mask also serves to hold the optical fibers--which carry light to the streak camera and make up the equation of state portion of the combined experiment--in position.

The light generated in the sample is reflected by an aluminized mirror, turning it 90° toward the optical pyrometer port. The same mirrors and mirror mounts as used in the standard experiment are employed, but light is reflected toward the pyrometer, which is in the opposite direction from the streak

camera. Also, the mirror mounts are slotted to provide an extra degree of freedom for optical alignment.

The port through which the light is reflected is covered with a glass window which separates the evacuated target chamber from the external instruments, and protects the objective lenses from flying debris generated by the impact. The objective is made up of two identical sets of achromats, with focal lengths of 49.5 cm and clear apertures of 10.6 cm. The target is near the focal point of the first achromat, with the beam folded by the turning mirror.

The converging light is separated into four legs by three beamsplitters (Figs. I-2, I-3). The primary beamsplitter is an Ealing 22-8924 pellicle, or stretched-membrane. The secondary beamsplitters are identical Melles-Griot 03 BTF 007 silvered plate-glass beamsplitters. Each of the four resulting beams falls upon a detector assembly , which consists of an interference filter, a focusing lens, and a silicon photodiode with a bias circuit (Fig. I-4). The filters are 25.4 mm in diameter and have wavelengths in the visible or near infrared, between the effective bandwidth limits of the silicon photodiodes of 400 and 1100 nm. Most of the filters used have half-height bandwidths of about 40 nm.

Each channel utilizes an RCA C30822 N-type silicon pin photodiode, with an active area of .20 cm^2. In order to ensure that the image of the sample (and calibration lamp, which is larger), falls entirely within the photodiode active area, it was necessary to employ a glass focusing lens, with diameter 18 mm and focal length 15 mm. This lens is positioned between the filter and photodiode, and demagnifies the image by a factor of about 0.2. The detector assembly is mounted on a three-dimensional translation stage to allow alignment and focus. The focusing lens and filter holder can be moved independently to permit

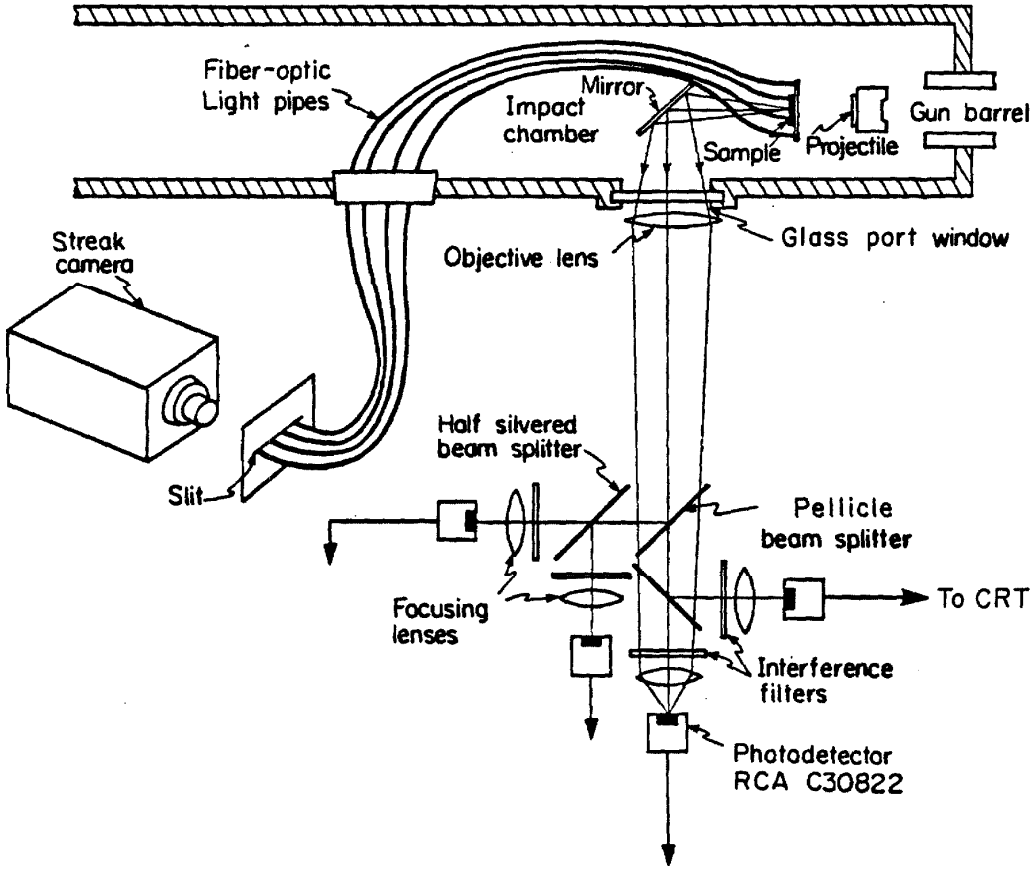

Fig. I-2. Schematic of shock temperature-equation of state experiment.

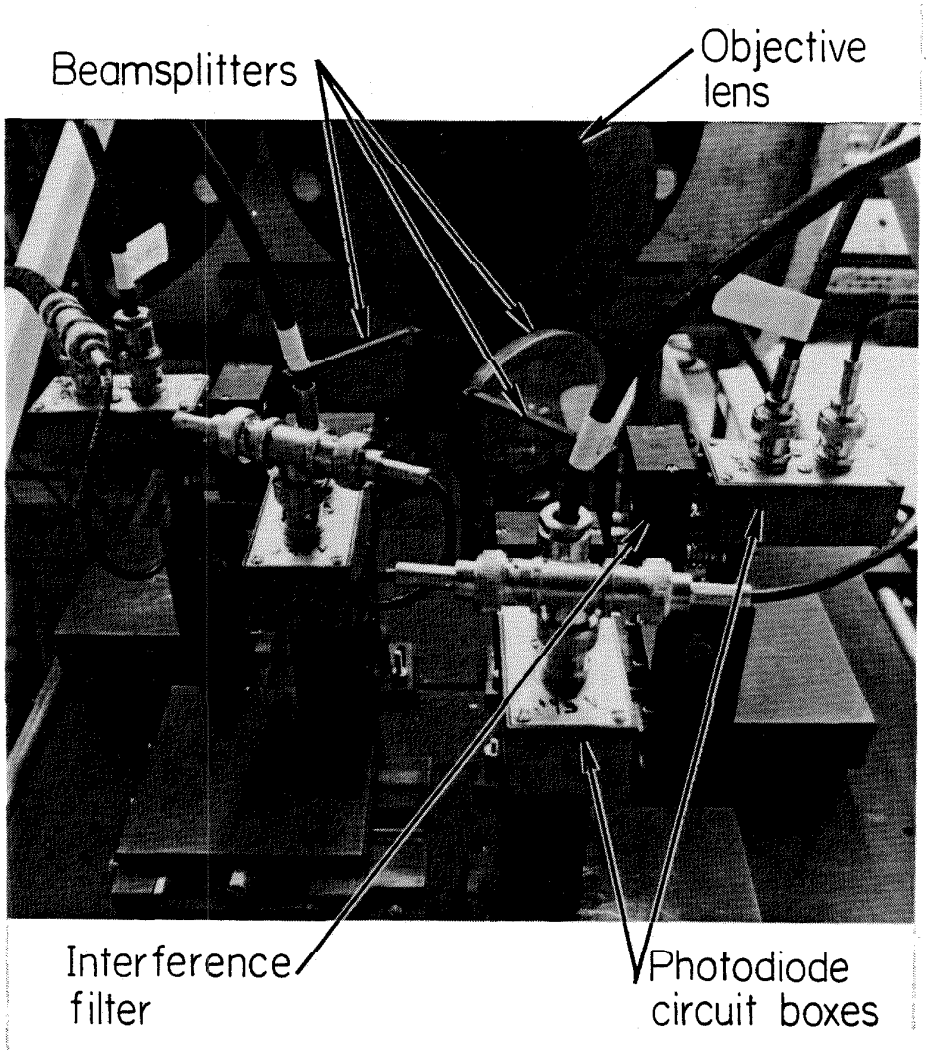

Fig. I-3. Photograph of four-channel wide-band optical pyrometer.

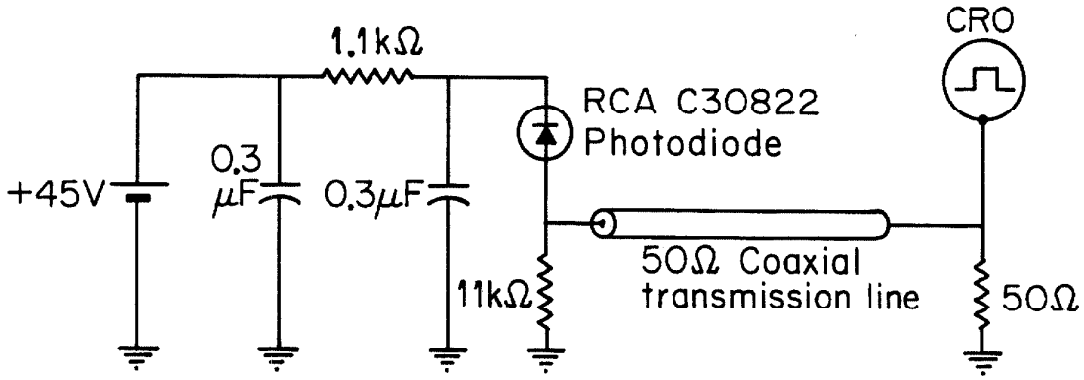

Fig. 1-4. Circuit diagram for single optical pyrometer channel.

separate adjustment of focus and demagnification.

This optical configuration ensures that each detector views precisely the same image, only at a different wavelength. Thus, if the radiation is heterogeneously emitted, as would be the case if shear bands or hot spots developed, the average brightness would be measured by each detector. This eliminates the possibility of one detector viewing a hot spot while another views between hot spots. Also, by viewing the entire unmasked portion of the target, the sensitivity of the instrument is maximized (Fig I-5). Because the image is demagnified there is sufficient leeway in alignment and focusing; as long as the entire image falls on the active area of the detector, it doesn't have to be centered or precisely focused.

The photodiode circuit is shown schematically in Fig. I-4. The circuit supplies 45 V reverse bias from a battery to the photodiode. The signal is carried to oscilloscopes by a 50 Ω coaxial cable, where it is terminated by a 50 Ω terminator. The principal recording oscilloscopes are Tektronix 485 models. These are triggered by a pulse generated by the closing of shorting pins mounted on the target as described above. Backup recording is provided by Tektronix 475, 454, and 545 oscilloscopes. These are set at lower sensitivities and slower sweep rates, and are triggered by the same pulse that triggers the second projectile-velocity-determining flash x-ray. Tektronix series C-30 cameras with ASA 20,000 Polaroid type 612 ultra high speed instrument recording film are used to record the oscillograms.

The light gas gun on which these experiments are carried out is described by Jeanloz and Ahrens (1977). Details on the operation of the light gas gun and determination of the projectile velocity are discussed there.

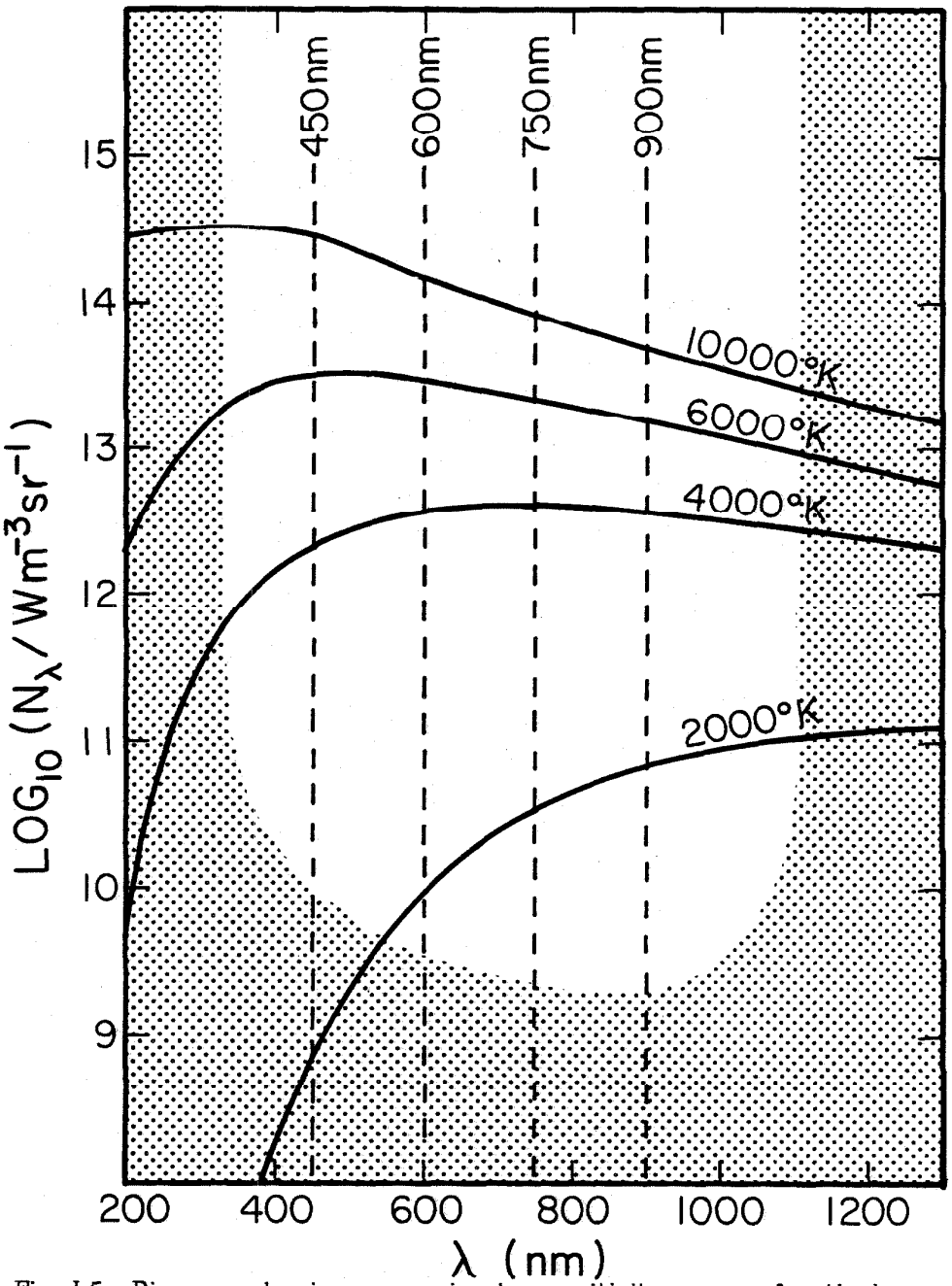

Fig. I-5. Diagram showing approximate sensitivity range of optical pyrometer. Curves give spectral radiance as a function of wavelength for a 6.35 mm diameter blackbody emitter at the position of the target. Dashed lines represent wavelength of detectors in typical experiment. Unstippled area is within sensitivity range of silicon photodiodes.

References

Jeanloz, R., and T.J. Ahrens, Pyroxenes and olivines: structural implications of shock-wave data for high-pressure phases, in *High Pressure Research*, edited by M.H. Manghani and S. Akimoto, pp. 439-461, Academic Press, New York, 1977.

Lyzenga, G.A., and T.J. Ahrens, A multi-wavelength optical pyrometer for shock compression experiments, *Rev. Sci. Instrum.*, *50*, 1421-1424, 1979.

Appendix II

Wide-Band Optical Pyrometer Calibration

The calibration procedure of the wide-band optical pyrometer was designed to minimize calibration error. By calibrating the instrument *in situ*, geometry-induced errors are minimized. The same oscilloscopes used to record the signals are used in the calibrations, minimizing the number of oscillograms to be read, which reduces possible reading and transfer error. Finally, because a separate calibration is performed before each experiment, the effect of variability in replacement windows and turning mirrors is taken into account. Also, any contamination of optical components, such as dust or residue, becomes less important, and components can be replaced readily.

A standard of spectral irradiance is placed in the position of the target in the impact chamber (Fig. II-1), and the pyrometer is aligned. Spectral irradiance is the power radiated per unit wavelength per unit solid angle, regardless of the surface area of the radiator. The standard source is a G.E. type Q6.6A/T4Q/1CL 200 Watt tungsten-filament quartz-halogen lamp, calibrated by Optronics Laboratories, Inc. It is mounted on a dummy target assembly and aligned in the same manner as a real target. It is driven by 6.50 Amperes from a Hewlett-Packard Model 6268B DC power supply constant current power supply. Current is monitored by a Keithley Model 173 Digital Multimeter, which measures the voltage across a .005 Ω resister in series with the lamp. The light is physically chopped at about 200 Hz, and the resulting square wave is recorded.

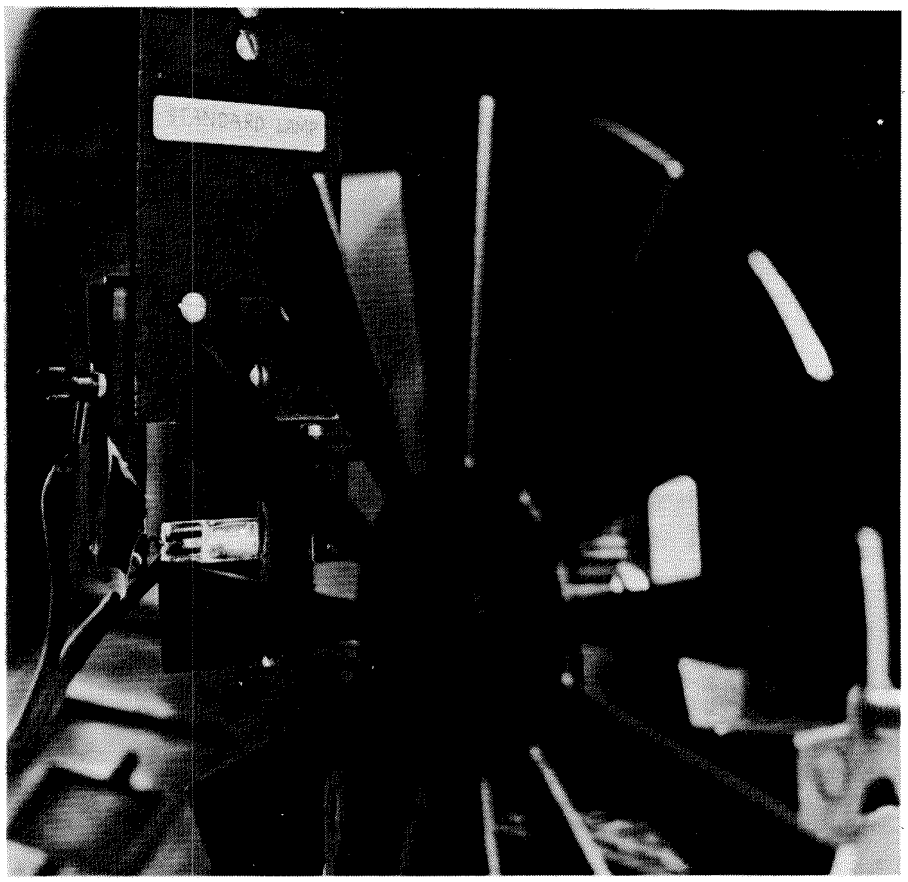

Fig. II-1. Photograph of pyrometer calibration set-up, with standard lamp in target position and chopper in place.

The amplitude of the wave is divided by the spectral irradiance of the lamp at the wavelength at which it is filtered, to determine the calibration factor. This calibration factor is multiplied by the amplitude of the shock record to get the spectral irradiance of the shocked material. To determine the spectral radiance, from which the temperature is calculated, the spectral irradiance is divided by the area of the hole in the edge mask. The solid angle needs not be known, as long as the calibration lamp and the target are in the same position.

The measured spectral irradiance in the wavelength range of interest of the calibration lamp is shown in Table II-1, as supplied by Optronics Laboratories. Note that the units are $\mu W/cm^2nm$ at 50 cm, where the cm^2 at 50 cm is a measure of solid angle and can be converted to steradians.

Table II-2 shows the uncertainty in lamp calibration as a function of wavelength in the range of interest, also supplied by Optronics Laboratories. This is the "reported uncertainty in the NBS 1973 irradiance scale along with the uncertainty associated with the transfer from the NBS standard to the issued 200 Watt standard". There is another 1% uncertainty quoted by Optronics in the stability of the lamp.

Because of the large (40 nm) half-height bandwidths of the filters used with this pyrometer, it is necessary to calculate the effective central wavelength of each filter, which is dependent on the spectral dependence of the other optical components, and on the temperature of the source. The other optical components have a weak spectral dependence relative to the filters, and this does not change greatly from shot to shot as components are replaced. It is thus possible to use nominal values published in component specifications, and measured values for the expendable components (the mirror and window) without

Table II-1

Standard lamp calibration

Wavelength (nm)	Spectral Irradiance(1)
400	.438
450	.908
500	1.52
550	2.21
600	2.90
650	3.52
700	4.07
750	4.50
800	4.77
900	5.01
1000	4.92

1. Spectral Irradiance in microwatts per (cm^2 nanometer) at a distance of 50 cm.

Table II-2

Spectral irradiance uncertainties of standard lamp

Wavelength (nm)	NBS Uncertainty[1] (%)	Transfer Uncertainty[2] (%)
250	2.5	1.1
350	1.4	0.8
450	1.2	0.5
555	1.0	0.5
655	0.75	0.5
800	0.9	0.7
1300	0.7	0.8
1600	0.7	1.0

1. Reported uncertainty in the National Bureau of Standards 1973 irradiance scale on which the lamp calibration was based.

2. Uncertainty associated with the transfer from the NBS standard, reported by Optronics Laboratories, Inc.

greatly affecting the results. The wavelength- dependent parameters of the various optical components (Fig. II-2) are:

$R_M(\lambda)$ = reflectance of the aluminized turning mirror; a typical mirror was measured at the Lawrence Livermore standards laboratory.

$T_W(\lambda)$ = transmittance of a typical glass port window; measured at Caltech with a Cary Model 17 spectrophotometer.

$T_L(\lambda)$ = transmittance of one Jeagers 35B1542 objective lens; measured at Caltech.

$T_{B_1}(\lambda)$ = transmittance of Ealing 22-8924 pellicle beamsplitter; from Ealing Optics catalog.

$R_{B_1}(\lambda)$ = reflectance of Ealing 22-8924 pellicle beamsplitter; from Ealing Optics catalog

$T_{B_2}(\lambda)$ = transmittance of Melles-Griot 03BTF007 plate-type beamsplitter; from Melles-Griot Optics catalog.

$R_{B_2}(\lambda)$ = reflectance of Melles-Griot 03BTF007 plate-type beamsplitter; from Melles-Griot Optics catalog.

$T_i(\lambda)$ = transmittance of filter i; measured at Caltech.

$T_l(\lambda)$ = transmittance of Melles-Griot 01LAG003 aspheric glass focusing lens; measured at Caltech

$R_i(\lambda) = r_i(\lambda)T_i(\lambda)$ = net spectral responsivity of channel i.

$r_i(\lambda)$ = net spectral reduction factor of channel i

$r_1(\lambda) = R_M T_W T^2_L T_{B_1} T_{B_2} T_l R_d.$

$r_2(\lambda) = R_M T_W T^2_L R_{B_1} R_{B_2} T_l R_d.$

$r_3(\lambda) = R_M T_W T^2_L T_{B_1} R_{B_2} T_l R_d.$

$r_4(\lambda) = R_M T_W T^2_L R_{B_1} T_{B_2} T_l R_d.$

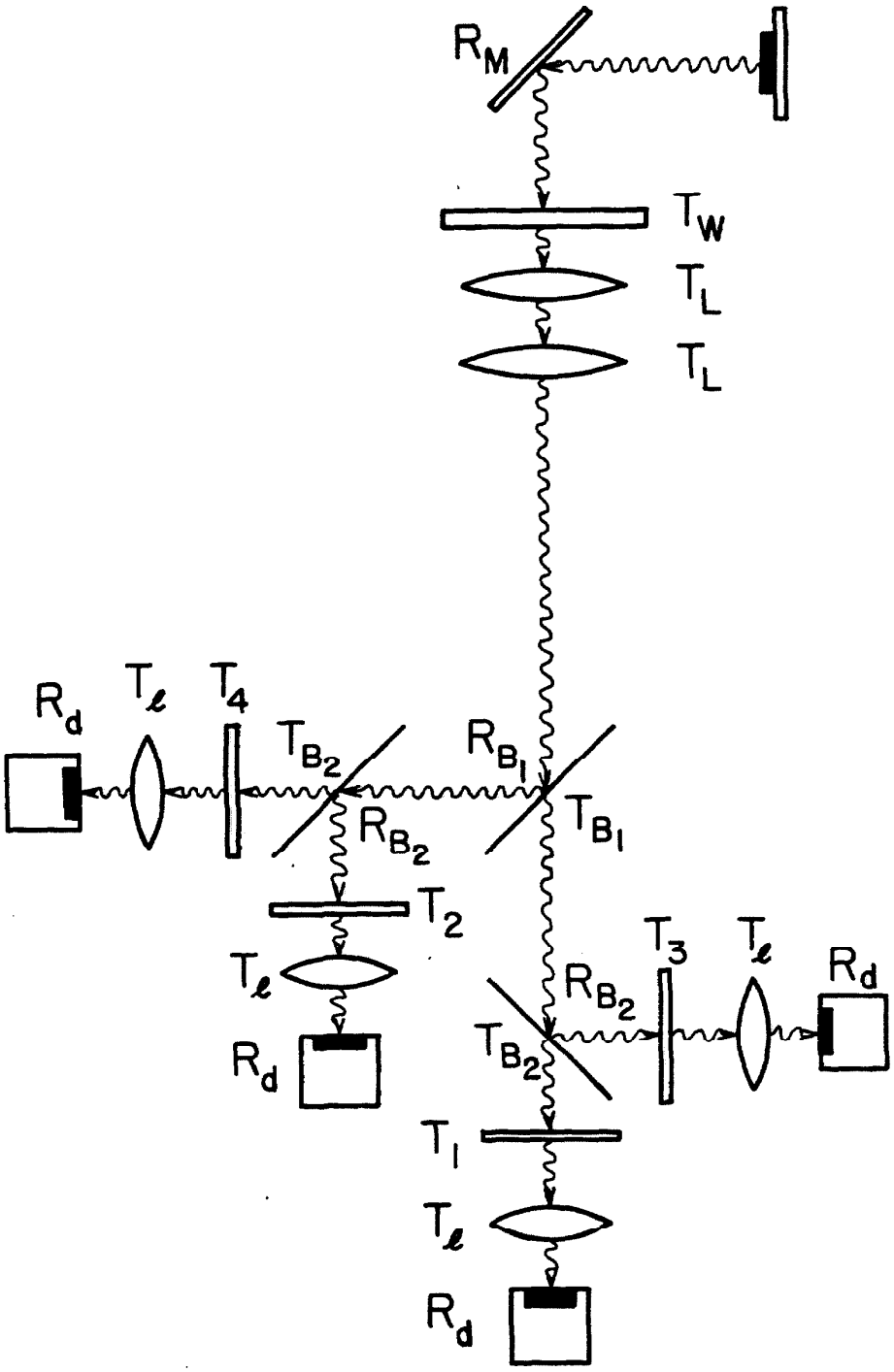

Fig. II-2. Schematic of optical pyrometer (Compare to Fig. I-2). Symbols are explained in text.

The mean wavelength of channel i is therefore

$$\bar{\lambda}_i = \frac{\int_0^\infty r_i(\lambda)T_i(\lambda)\lambda d\lambda}{\int_0^\infty r_i(\lambda)T_i(\lambda)d\lambda}. \qquad \text{(II-1)}$$

There will also be a shift in effective wavelength as a function of temperature of the source, and this should be included. To calculate the shift, we must assume *a priori* that the source radiates a Planck function. This assumption will also need to be made in order to reduce the data, so nothing is lost in making it now. The data will confirm the validity of the assumption, in the cases studied (Appendix III).

The mean effective wavelength as a function of temperature is

$$\bar{\lambda}_i = \frac{\int_0^\infty r_i(\lambda)T_i(\lambda)f(T,\lambda)\lambda d\lambda}{\int_0^\infty r_i(\lambda)T_i(\lambda)f(T,\lambda)d\lambda}, \qquad \text{(II-2)}$$

where $f(T,\lambda)$ is the Planck function

$$f(T,\lambda) \propto \lambda^{-5}(e^{\frac{hc}{k_B\lambda T}}-1)^{-1}. \qquad \text{(II-3)}$$

The mean effective wavelengths of the channel-filter combinations which have been used are plotted in Figs. II-3 and II-4. The calibration lamp temperature is about 2700°K, so the effective wavelengths for calibration are those at 2700°K. The appropriate spectral irradiance is found by interpolating between values given in Table II-1.

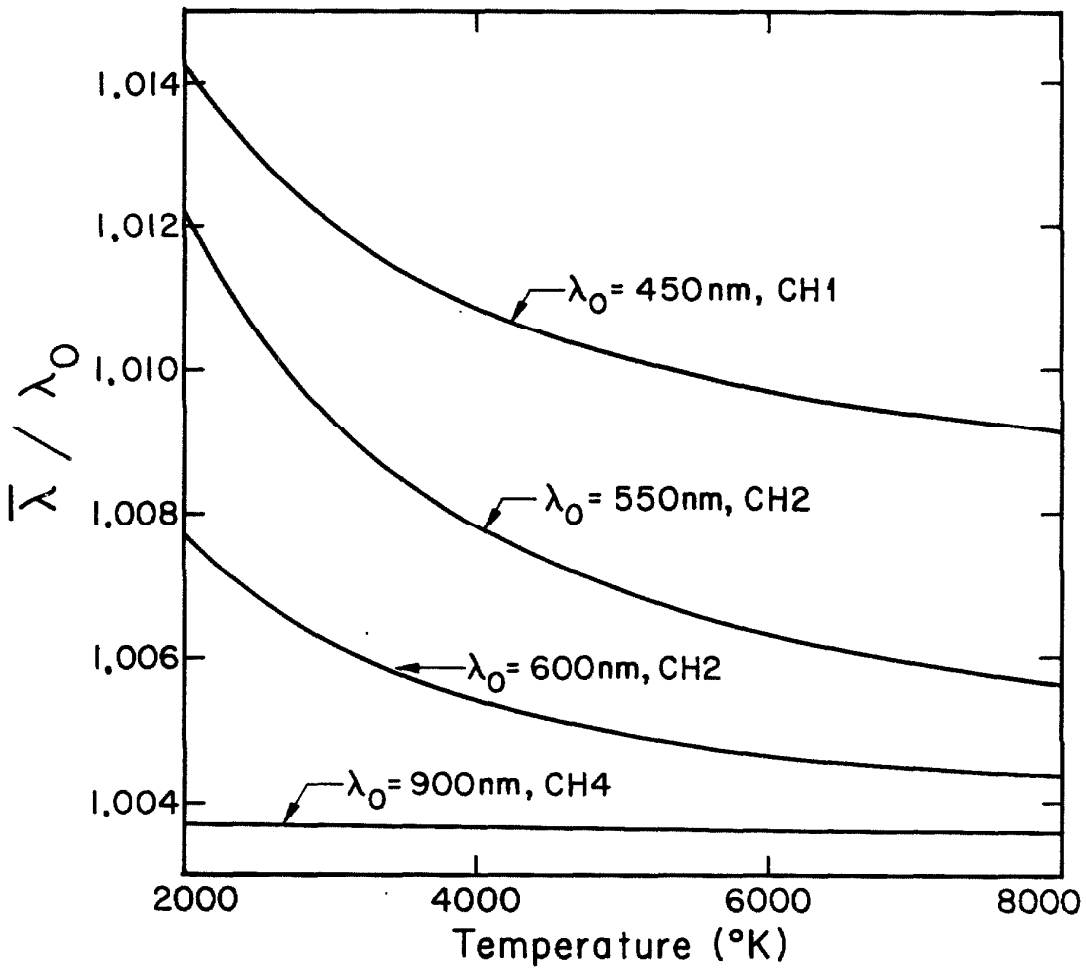

Fig. II-3. Mean effective wavelength $\bar{\lambda}$ of four wavelength-channel combinations, normalized to nominal filter wavelength λ_o.

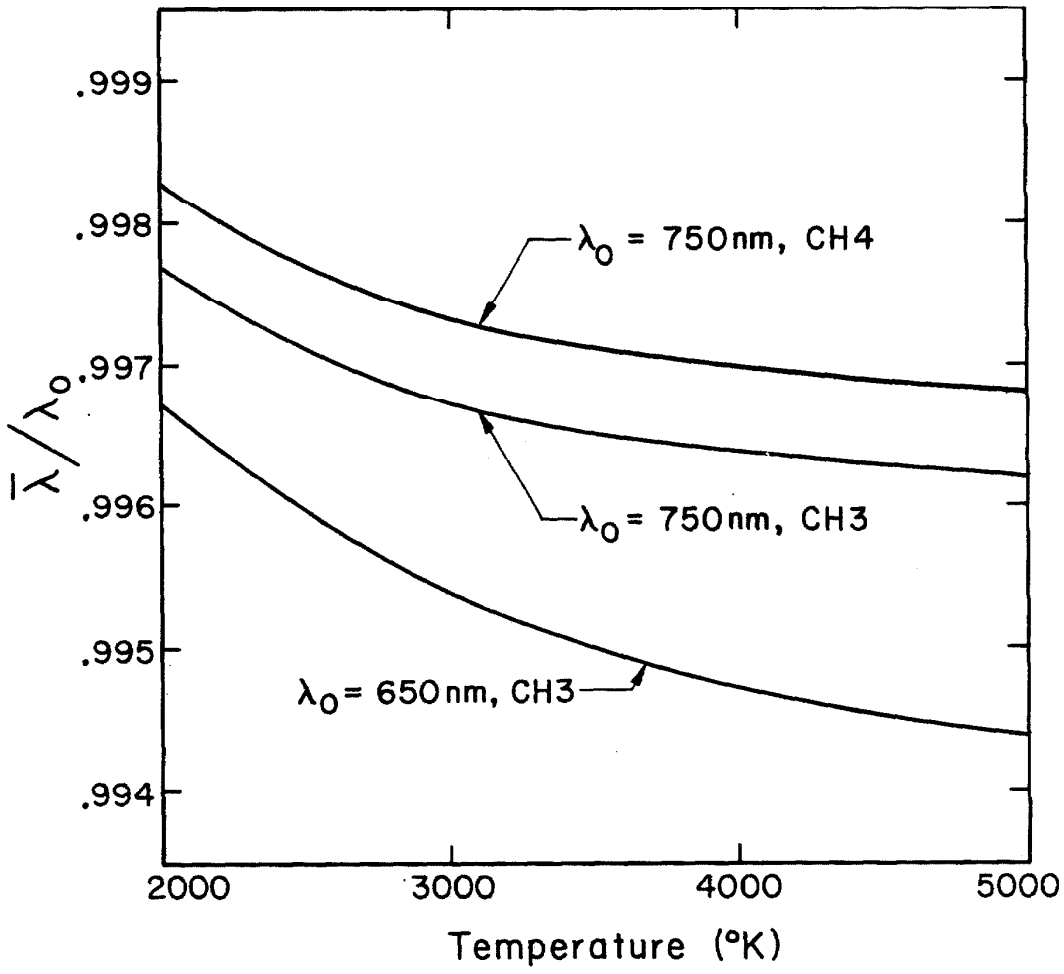

Fig. II-4. Mean effective wavelength $\bar{\lambda}$ of three wavelength-channel combinations, normalized to nominal filter wavelength λ_o.

Appendix III

Measured spectral radiances and calculated temperatures

The measured spectral radiances used to calculate shock temperatures are reported here. In Tables III-1 and III-2, spectral radiances obtained in seven shots conducted with the narrow-band six-channel optical pyrometer at Lawrence Livermore National Laboratory are tabulated. The design, calibration, and execution of experiments with this instrument are described by Lyzenga et. al. (1979) and Lyzenga (1980). Because narrow bandwidth (10 nm wide) filters have been used with this instrument, the effective wavelengths are not a function of temperature. Table III-3 gives the spectral radiances measured at Caltech using the wide-band four-channel optical pyrometer for five experiments. This table includes the effective wavelength of each channel, which is temperature-, and therefore shot-dependent.

The temperature is calculated in all cases assuming a Planck distribution of radiated light

$$N_\lambda = \varepsilon C_1 \lambda^{-5} (e^{\frac{C_2}{\lambda T}} - 1)^{-1}, \qquad \text{(III-1)}$$

where N_λ is the spectral radiance in $WSr^{-1}m^{-3}$, ε is the emissivity, λ is wavelength in m, and T is absolute temperature in °K. The constants are $C_1 = 1.191 \times 10^{-16}$ and $C_2 = 1.439 \times 10^{-2}$. The measured spectral radiances and

the best fitting blackbody Planck curves (with $\varepsilon \equiv 1.0$) are plotted together in Figs. III-1 through III-12.

Table III-1

Calcium oxide spectral radiance data

Channel	CaO1T		CaO2T		CaO3T	
	$\lambda^{(1)}$	$N_\lambda^{(2)}$	λ	N_λ	λ	N_λ
1	450.2	13.9 ±0.9	450.2	1.38 ±0.30	450.2	32.1 ±2.1
5	507.9	18.6 ±1.0	507.9	2.11 ±0.25	507.9	32.4 ±2.0
2	545.1	17.3 ±1.4	545.1	2.72 ±0.38	545.1	34.2 ±2.3
6	598.0	19.6 ±1.2	598.0	2.31 ±0.33	598.0	33.7 ±2.0
3	650.0	16.4 ±0.9	650.0	2.47 ±0.23	650.0	27.8 ±1.6
4	792.0	12.3 ±0.6	792.0	2.78 ±0.34	792.0	18.9 ±1.2

1. Wavelength (λ) in nm.

2. Spectral radiance (N_λ) in 10^{12} $Wm^{-3}Sr^{-1}$.

Table III-2

Anorthite glass spectral radiance data

Channel	An1T		An2T		An3T	
	$\lambda^{(1)}$	$N_\lambda^{(2)}$	λ	N_λ	λ	N_λ
1	450.2	11.4 ±0.6	450.2	1.92 ±0.15	450.2	0.109 ±0.070
5	507.9	13.3 ±0.5	507.9	2.73 ±0.29	507.9	0.327 ±0.049
2	545.1	14.9 ±0.6	545.1	3.24 ±0.13	545.1	0.489 ±0.094
6	598.0	14.3 ±0.4	598.0	3.72 ±0.23	598.0	0.433 ±0.044
3	650.0	14.5 ±0.7	650.0	4.09 ±0.21	650.0	0.670 ±0.123
4	792.0	11.5 ±0.3	792.0	4.34 ±0.32	792.0	0.951 ±0.044

1. Wavelength (λ) in nm.

2. Spectral radiance (N_λ) in 10^{12} $Wm^{-3}Sr^{-1}$.

Table III-3

Anorthite glass spectral radiance data

Channel	An5T		An6T		An7T		An9T		An10T	
	$\lambda^{(1)}$	$N_\lambda^{(2)}$	λ	N_λ	λ	N_λ	λ	N_λ	λ	N_λ
1	454.4	0.0455 ±0.0078	454.8	0.0137 ±0.0076	off scale		453.5	2.18 ±0.09	453.0	23.5 ±1.2
2	556.8	0.165 ±0.014	557.2	0.0595 ±0.0105	off scale		603.2	3.98 ±0.14	602.8	19.0 ±0.7
3	647.6	0.314 ±0.028	647.6	0.0128 ±0.019	off scale		747.5	4.25 ±0.15	747.3	19.0 ±1.6
4	748.3	0.412 ±0.036	748.4	0.0228 ±0.024	903.3	0.623 ±0.026	903.3	3.77 ±0.17	903.3	11.9 ±0.5

1. Wavelength (λ) in nm.

2. Spectral radiance (N_λ) in 10^{12} $Wm^{-3}Sr^{-1}$.

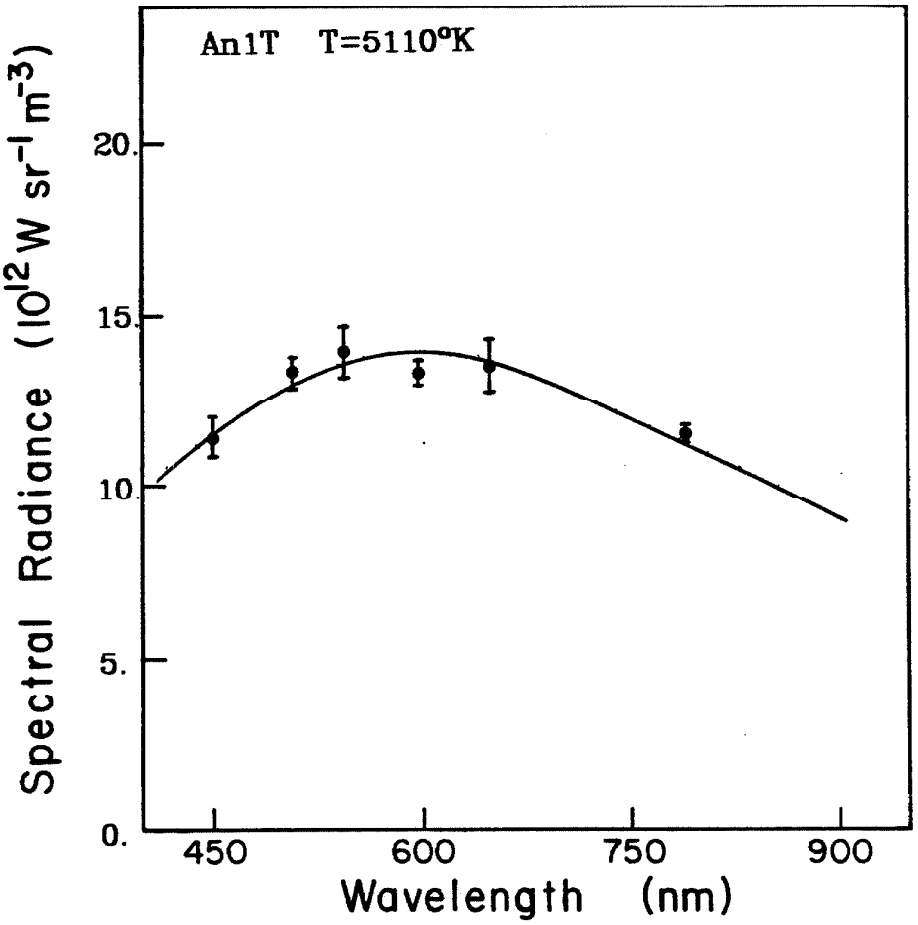

Fig. III-1. Spectral radiance data for shot An1T.

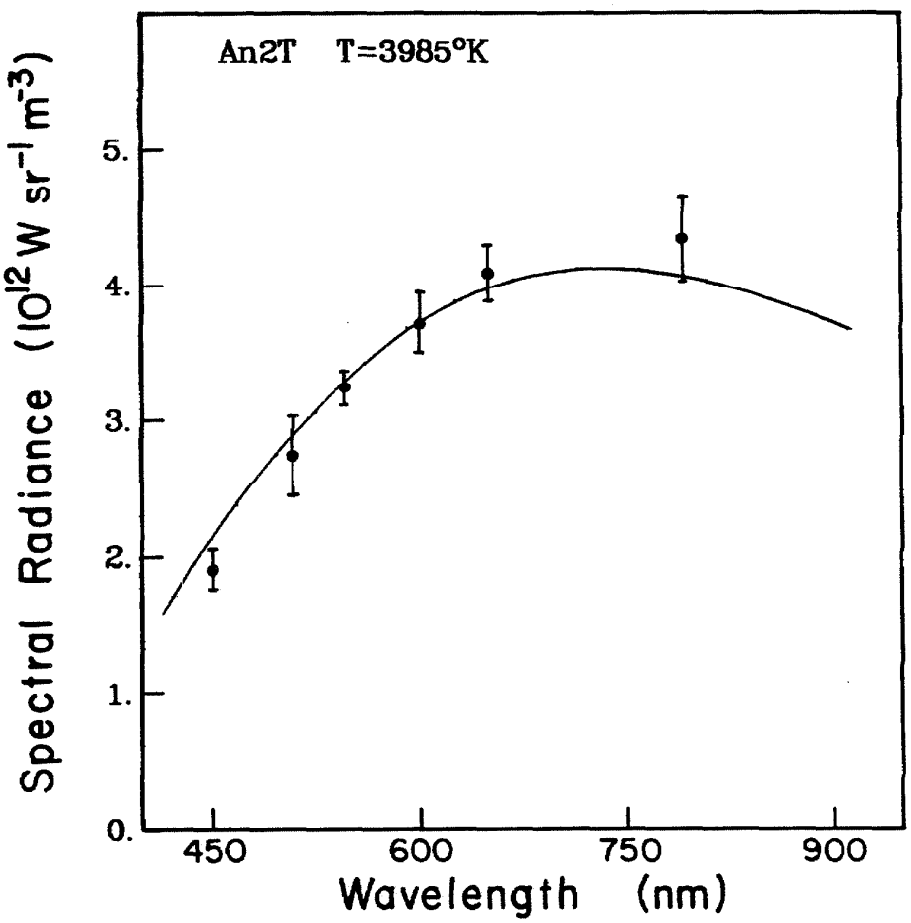

Fig. III-2. Spectral radiance data for shot An2T.

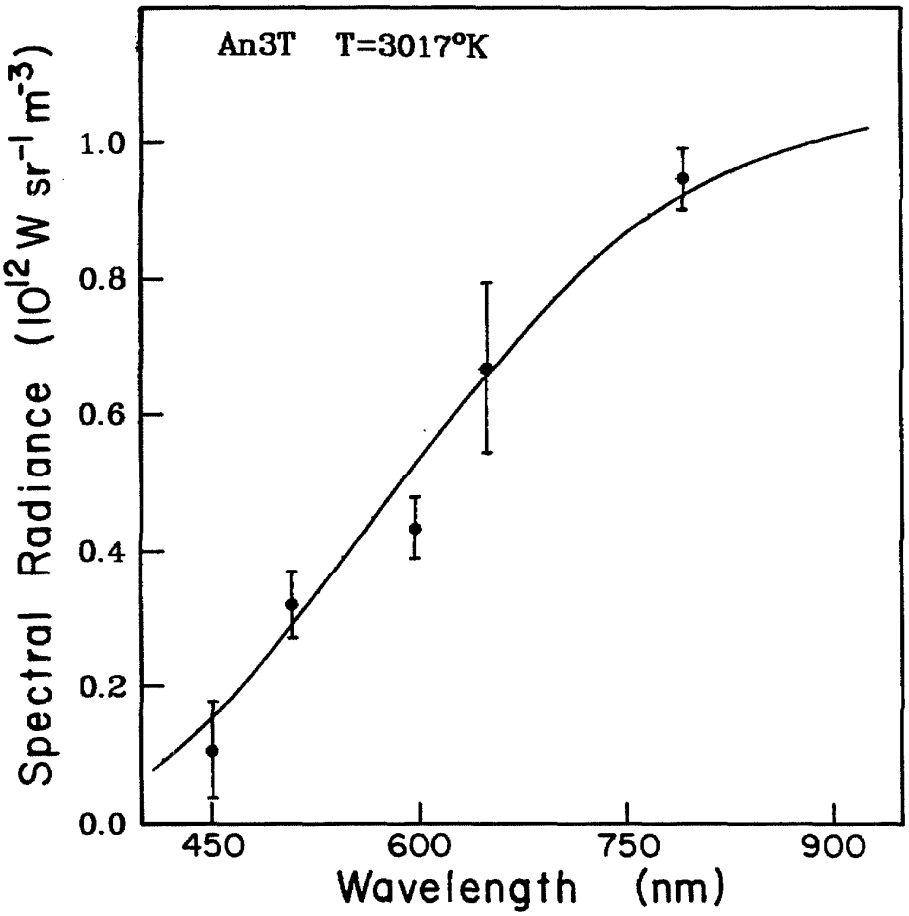

Fig. III-3. Spectral radiance data for shot An3T.

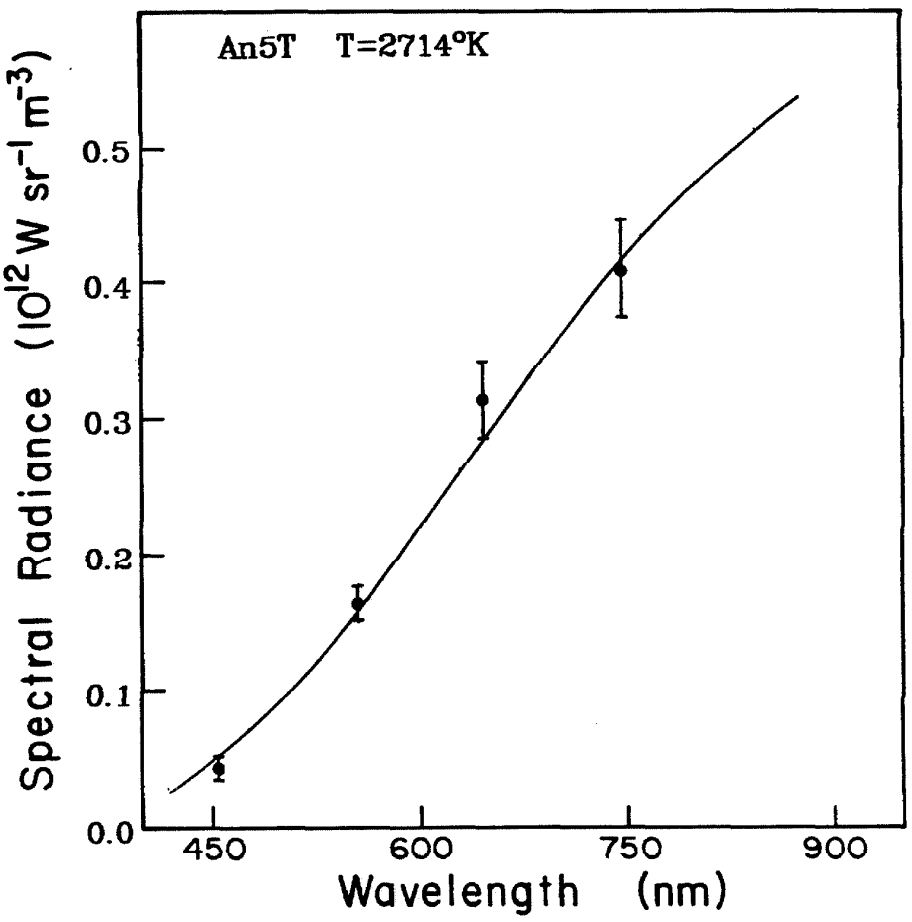

Fig. III-4. Spectral radiance data for shot An5T.

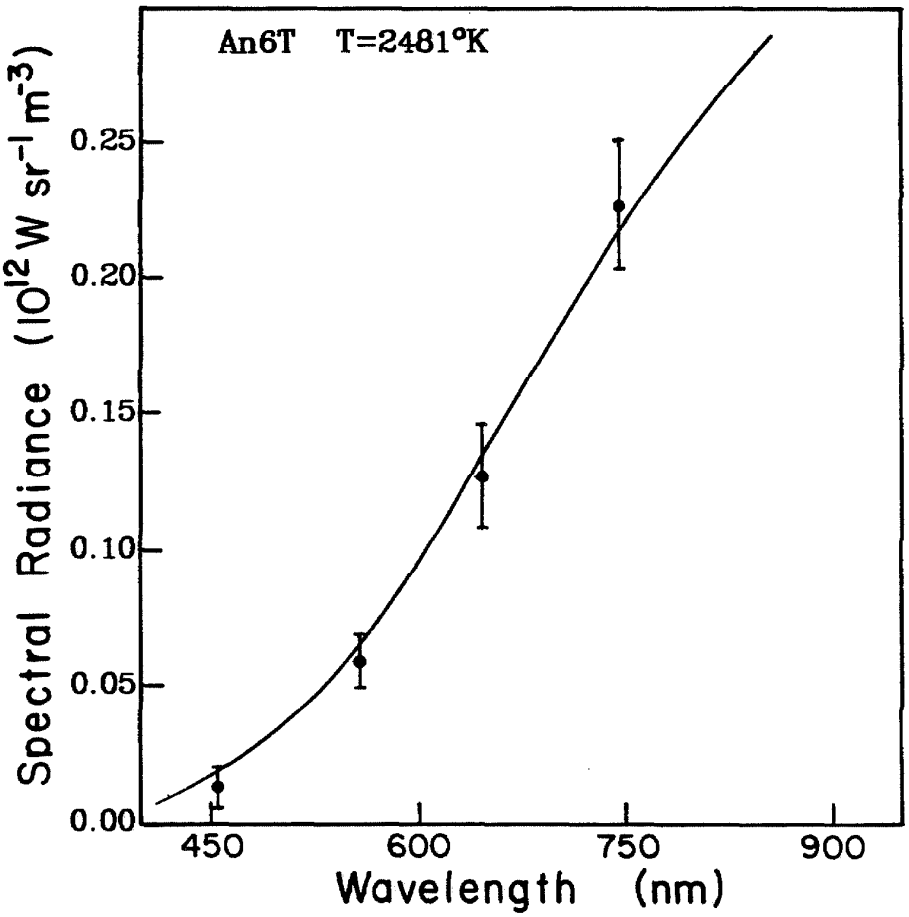

Fig. III-5. Spectral radiance data for shot An6T.

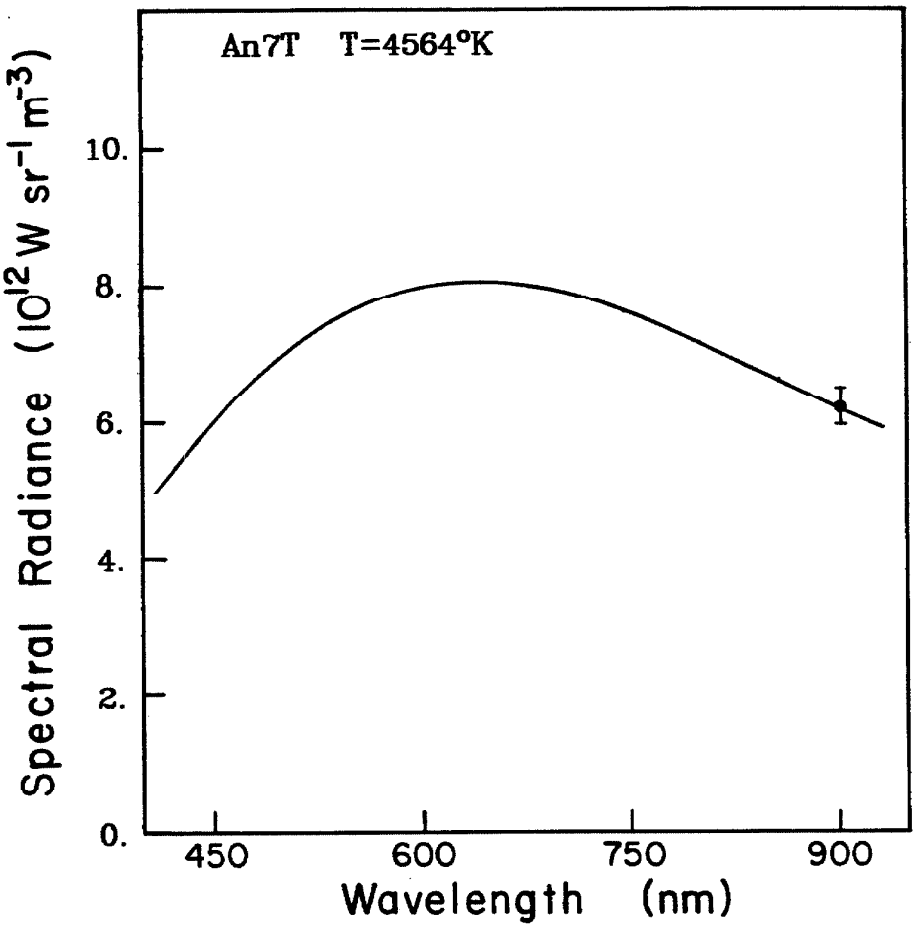

Fig. III-6. Spectral radiance data for shot An7T.

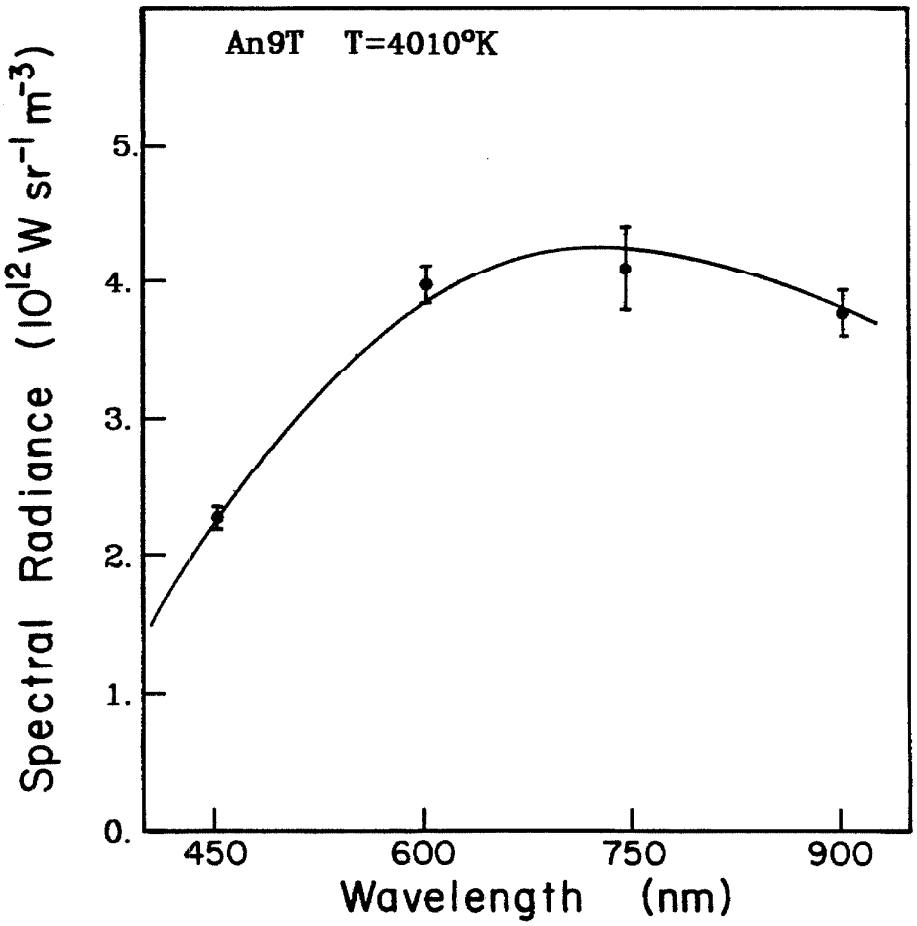

Fig. III-7. Spectral radiance data for shot An9T.

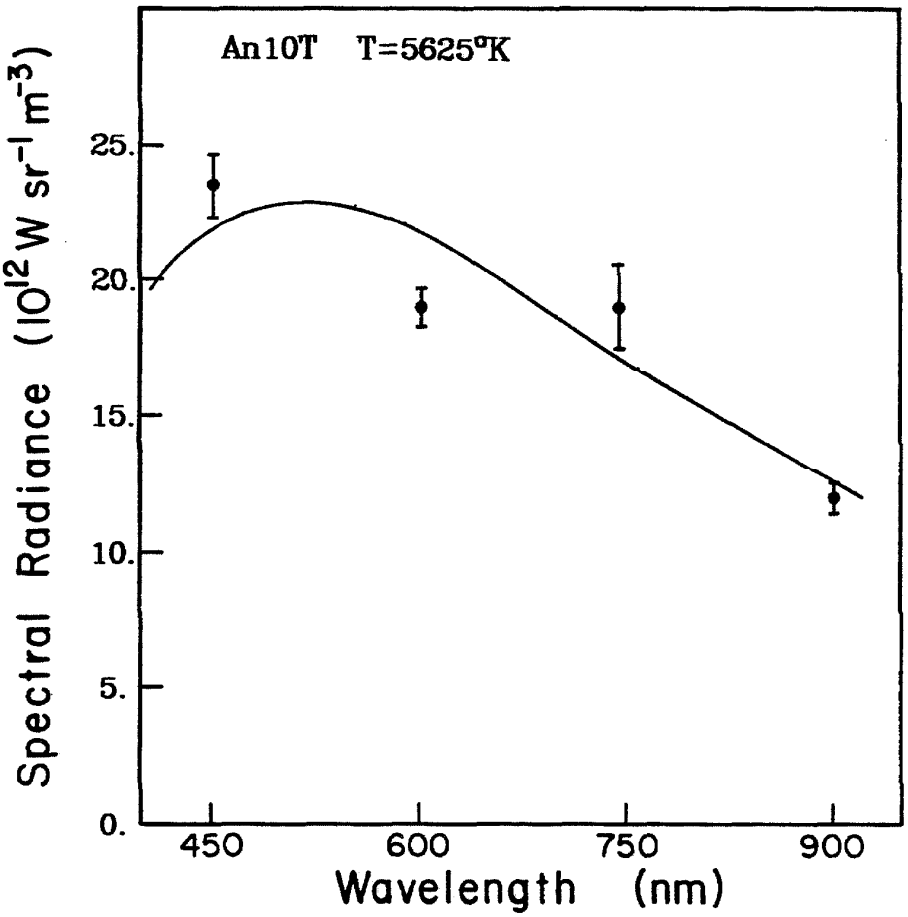

Fig. III-8. Spectral radiance data for shot An10T.

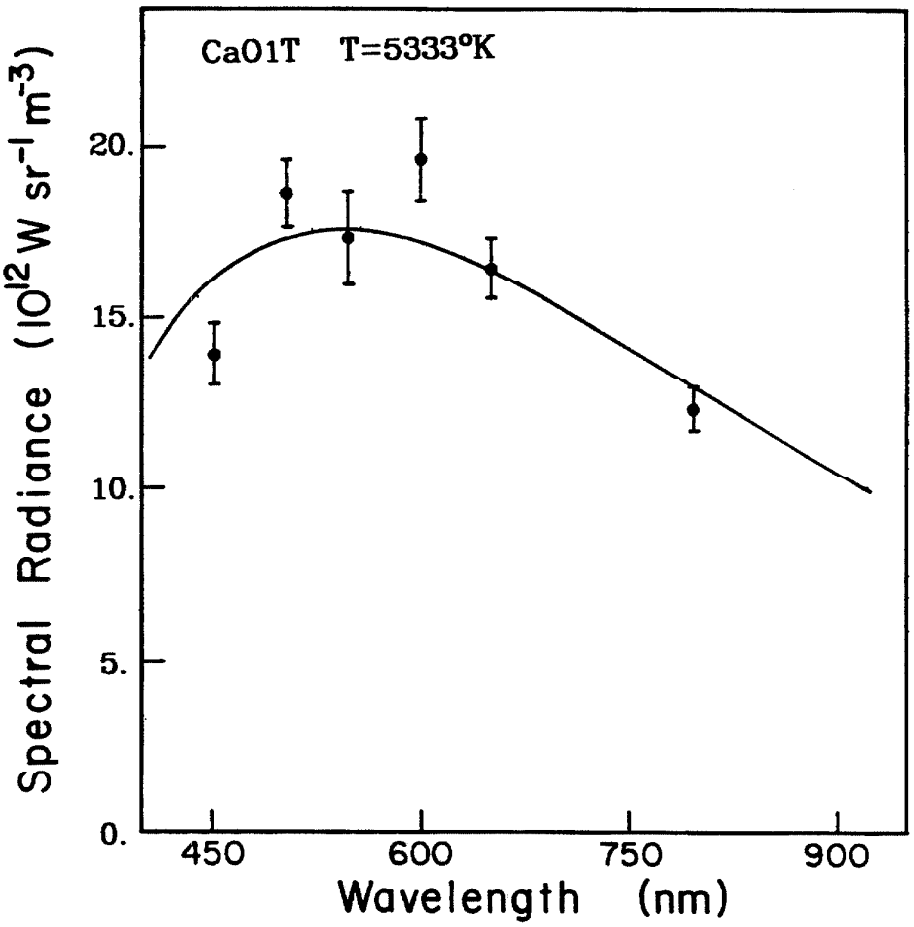

Fig. III-9. Spectral radiance data for shot Ca01T.

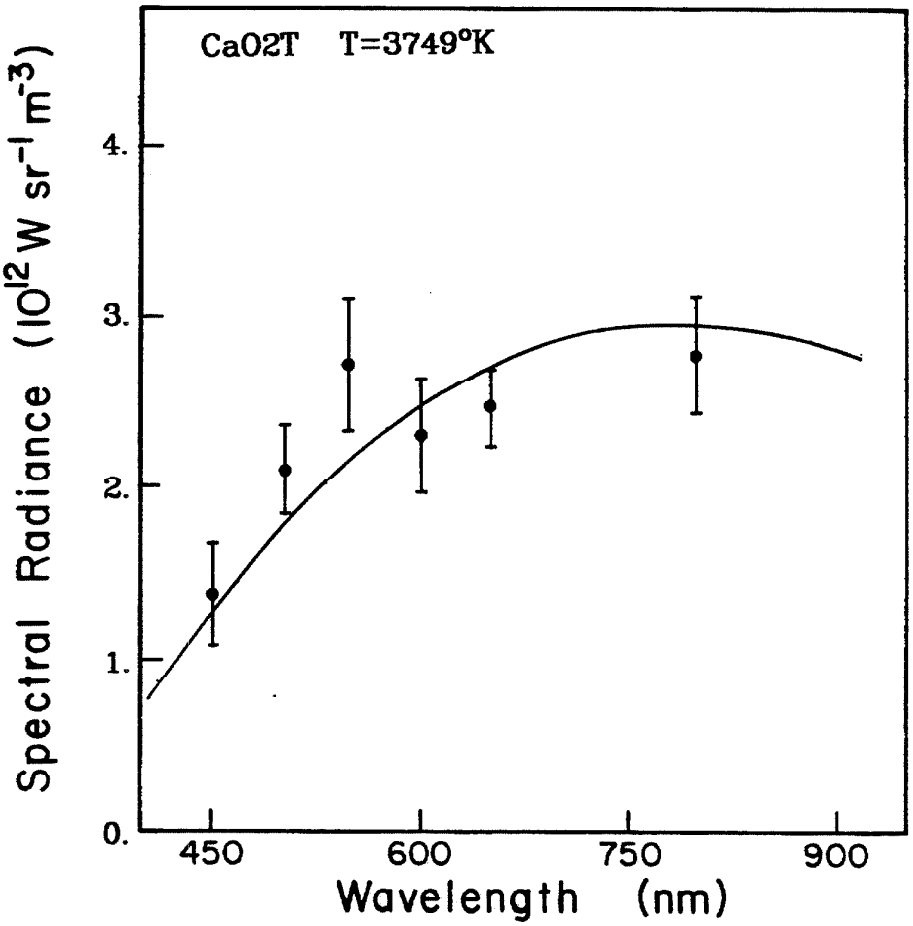

Fig. III-10. Spectral radiance data for shot CaO2T.

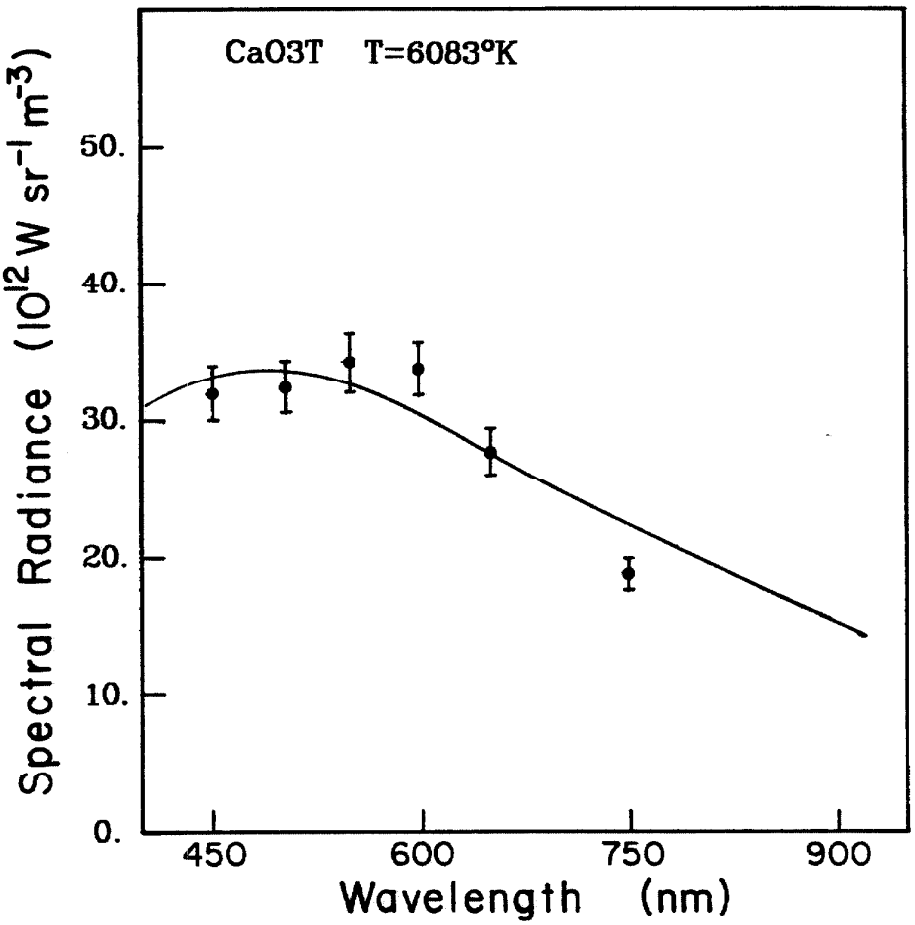

Fig. III-11. Spectral radiance data for shot CaO3T.

References

Lyzenga, G.A., and T.J. Ahrens, A multi-wavelength optical pyrometer for shock compression experiments, *Rev. Sci. Instrum.*, *50*, 1421-1424, 1979.

Lyzenga, G.A., Shock temperatures of materials: experiments and applications to the high pressure equation of state, Ph.D. Thesis, Calif. Inst. of Technol., Pasadena, 1980.

Appendix IV

Particle Velocity Experiment Design

The purpose of the particle velocity experiment is to provide Hugoniot, sound speed, and release data in a single experiment. The experimental design is similar to those of Grady *et al.* (1974), Larson and Anderson (1979), and Kondo *et al.* (1980), and makes use of electromagnetic particle velocity gauges (Dremin and Shvevdov, 1974). Gauges are oriented in a steady, uniform magnetic field such that the active element of the gauge, the magnetic field lines, and the direction of motion are all mutually perpendicular (Fig. IV-1), and the gauge leads are parallel to the magnetic field. An electromotive force is induced along the length of the gauge element, proportional to the velocity of the gauge. For a gauge with effective length L in a magnetic field B, the potential measured across the gauge leads is

$$V(t)=BLu_p(t) \qquad \text{(IV-1)}$$

where u_p is the particle velocity of the material in which the gauge is embedded.

Gauges were photoetched from 10.0 μm thick copper foil with a 12.5 μm thick polyamide (Kapton) film backing. The active elements of the gauges were 0.9 to 1.0 cm long (Fig. IV-2). The precise effective gauge length (used in equation IV-1) is dependent on the geometry of the gauge due to edge effects from the leads and the finite gauge width. It is about equal to the center-to-center lead distance of .95 cm.

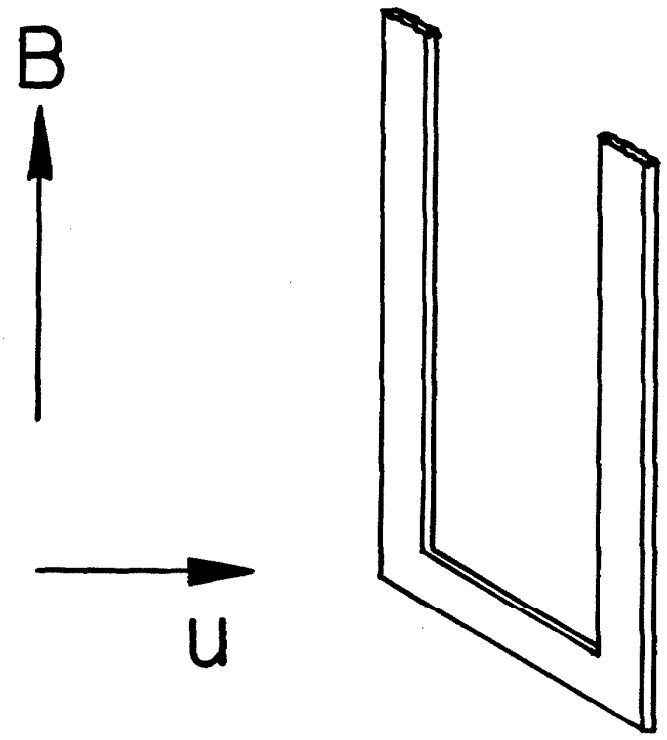

Fig. IV-1. Orientation of electromagnetic particle velocity gauge with respect to magnetic field B, and gauge velocity, u.

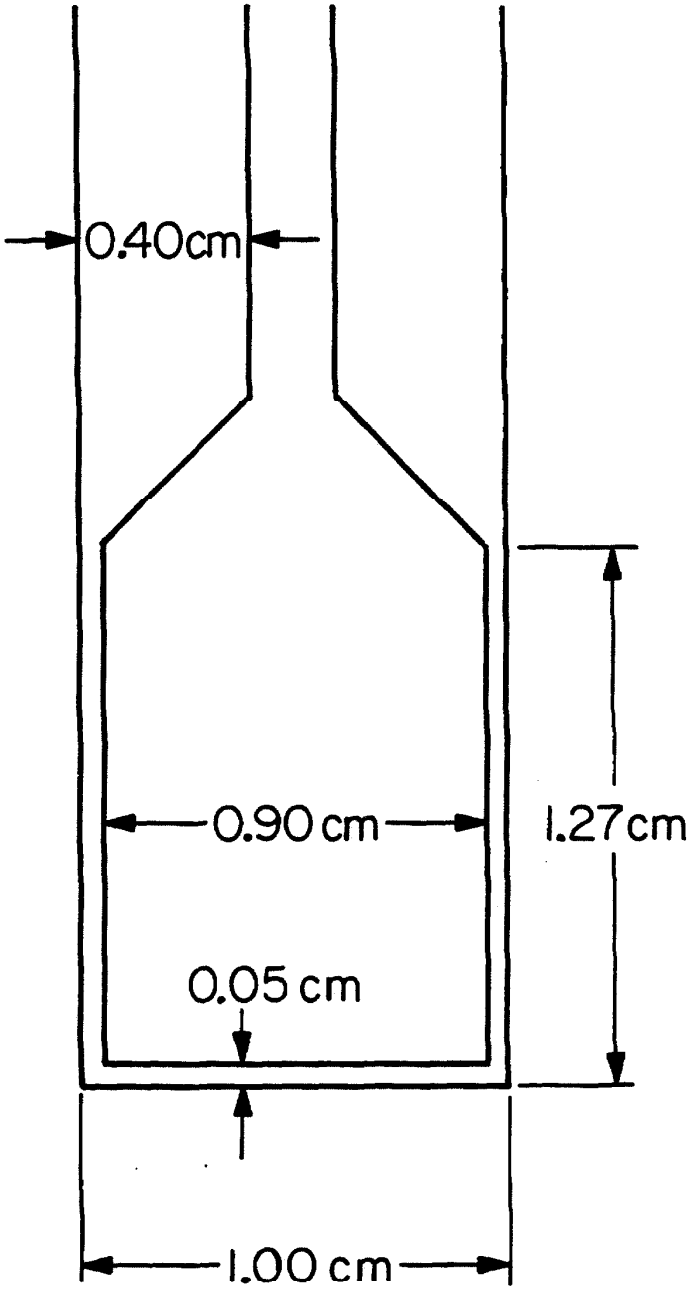

Fig. IV-2. Dimensions of gauges used in particle velocity experiment.

Rock samples were constructed by sawing rectangular slabs about 3.2 cm by 4.5 cm and grinding them to a uniform thickness of about 1.5 mm. Archimedean densities were determined for each slab individually. Four slabs were bound together with epoxy, with three gauges at the interfaces and one at the free surface. The mean thickness of the glue at each interface was 9 μm, as determined by measuring the total thickness of the completed target and subtracting from it the thicknesses of the individual component slabs and gauges. All four sets of gauge leads extended from the sample in the same direction, along the long axis of the slabs, such that the gauges were all parallel and even. Coaxial cables were soldered to the gauge leads, and were connected to oscilloscopes for the shot. A typical rock target is pictured in Fig. IV-3.

Water targets were constructed similarly, with the slabs replaced by 1.5 mm thick fiberglass rings. The polyamide membranes were tightly stretched over the rings, and the rings were bonded together with epoxy. They were mounted on a 3.0 mm thick polycarbonate (Lexan) driver plate, and each cell-like space between the sets of gauges was injected with distilled water. The distance between the gauges was determined by focusing a microscope on each gauge and recording the difference in focal positions, and correcting for the index of refraction the water between the gauges. A water target is pictured in Fig. IV-4.

In Fig. 4-1, the entire particle velocity experimental assembly is shown schematically, with a rock target mounted on the center of the axis of a set of Helmholtz coils, which supply the magnetic field. To ensure mutual perpendicularity between the gauge, field, and particle velocity, the target is aligned by shining an alignment laser beam down the gun barrel and adjusting the target

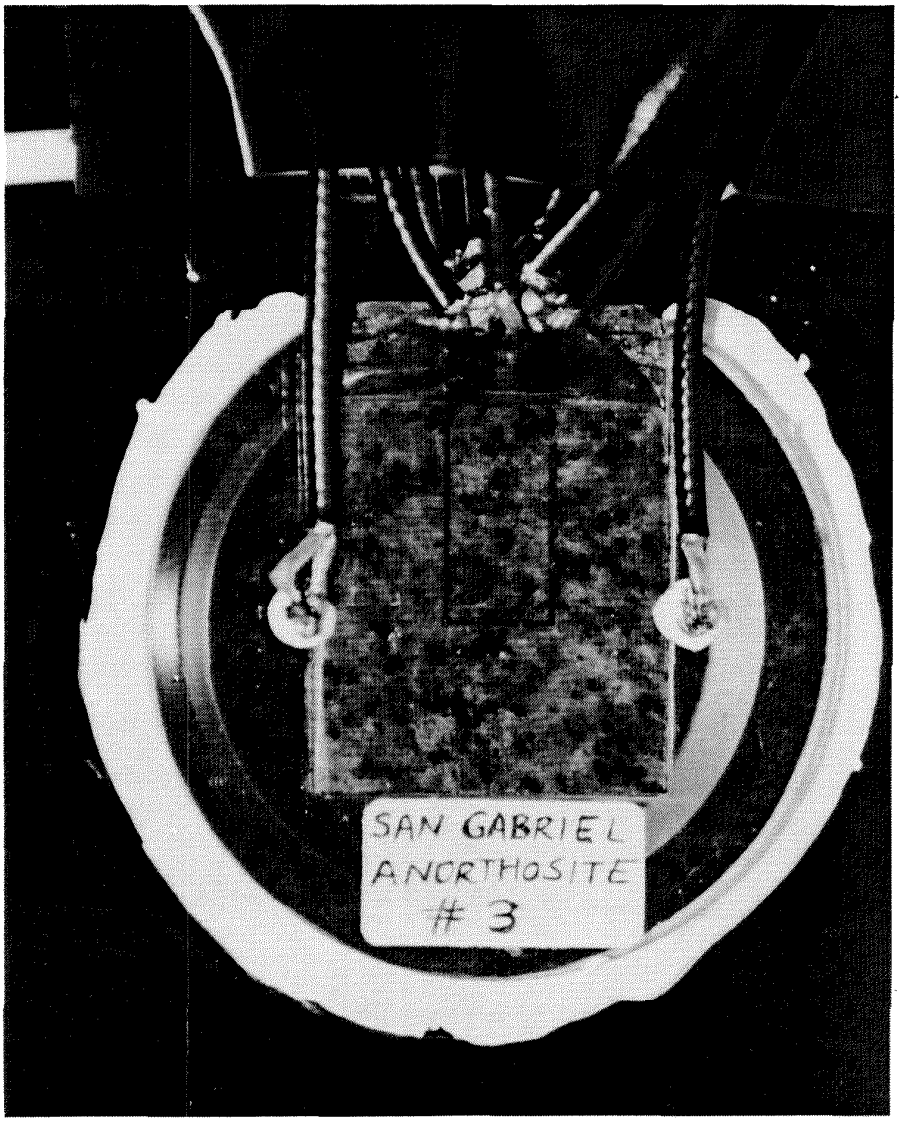

Fig. IV-3. Typical rock sample, with free-surface gauge visible.

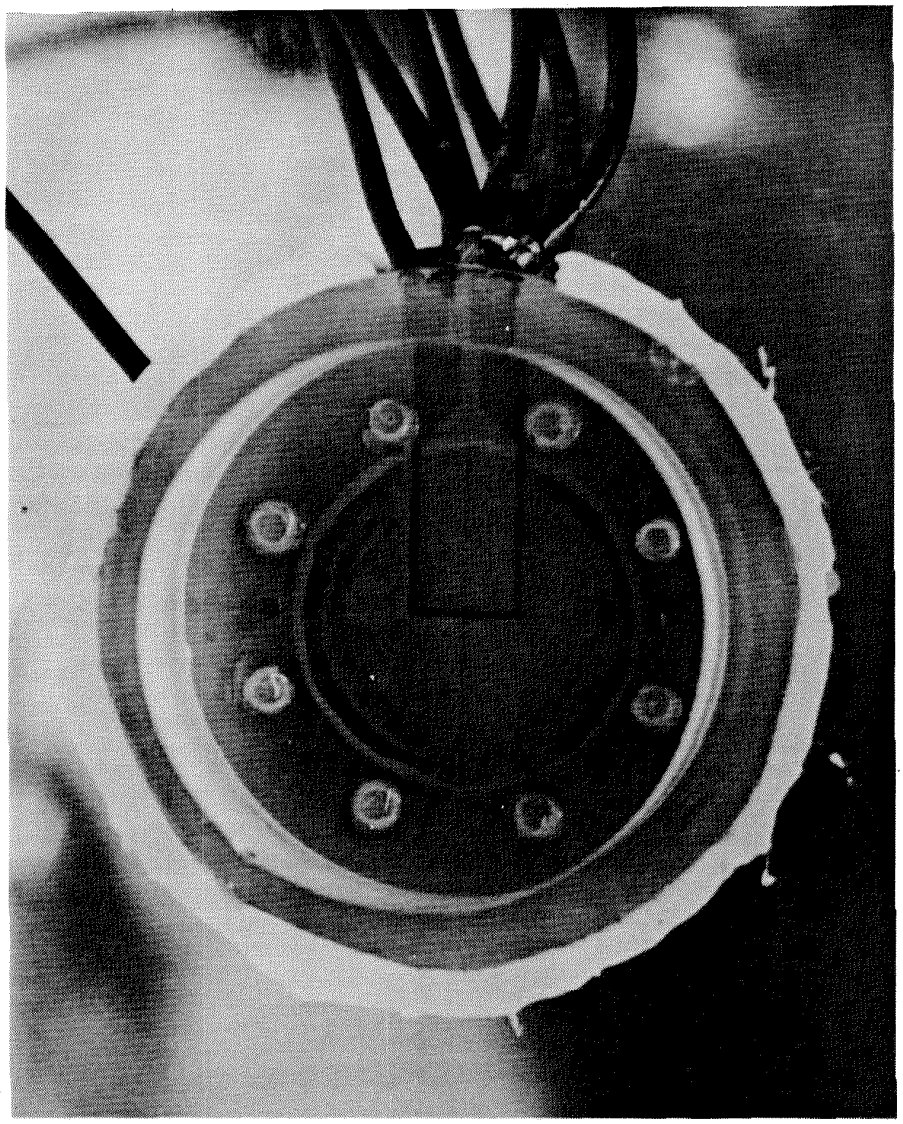

Fig. IV-4. Typical water sample.

until the beam is reflected back up the barrel by a mirror mounted on the target front surface.

The Helmholtz coils (Fig. IV-5) have a radius and separation of 14.1 cm, and are wound with four turns of gauge 10 copper wire. The magnetic field at the center point of the coil axis is constant to third order, and equal to

$$B=\frac{8\mu_o IN}{(5)^{3/2}r} \qquad \text{(IV-2)}$$

where μ_o is the permeability constant, I is the current, N is the number of turns and r is the radius and distance between coils. The field is typically about 1.8 kG. The current is supplied by a bank of 5 15 μF capacitors charged to 5.0 kV, and reaches its peak value of about 6.7 kA in about 60 μs (Fig. IV-6). Because the time scale of the experiment--which is determined by the shock and rarefaction transit times through the sample ($\approx 2\mu$s)-- is short compared to the period of the capacitor-coil circuit ($\approx 250\mu$s), the timing can be controlled so that impact occurs at the peak current, when the field is effectively constant.

A simplified circuit diagram is shown in Fig IV-7. As the projectile approaches the end of the gun barrel, it interrupts a timing laser beam. This sends a signal to a trigger delay unit, which, after a pre-determined delay, sends a pulse to an EG&G TM-11 trigger module, closing a spark gap which in turn fires an ignitron, which dumps the charge in the large capacitor bank through the Helmholtz coils. The current is monitored by a Pearson Electronics Inc. Model 301x Wide Band current transformer, which is fed into a Tektronix Model 545A Oscilloscope, which is triggered by the same pulse that triggers the ignitron.

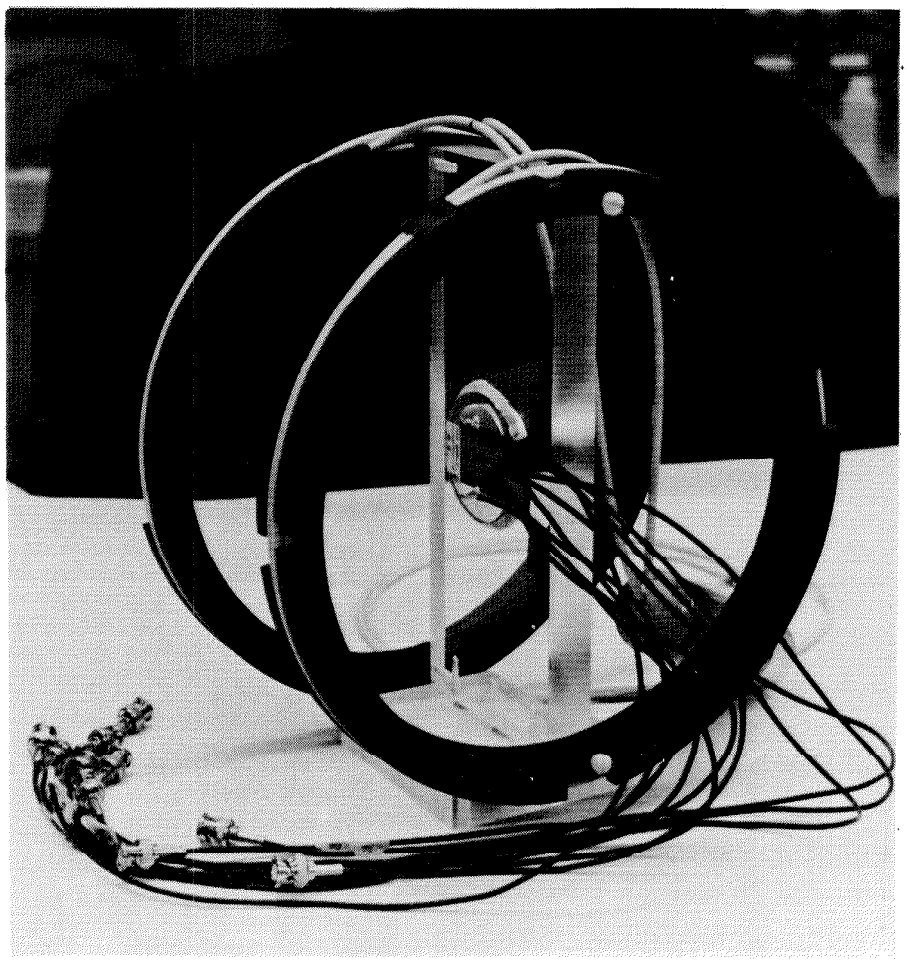

Fig. IV-5. Helmholtz coil assembly, with rock target in place.

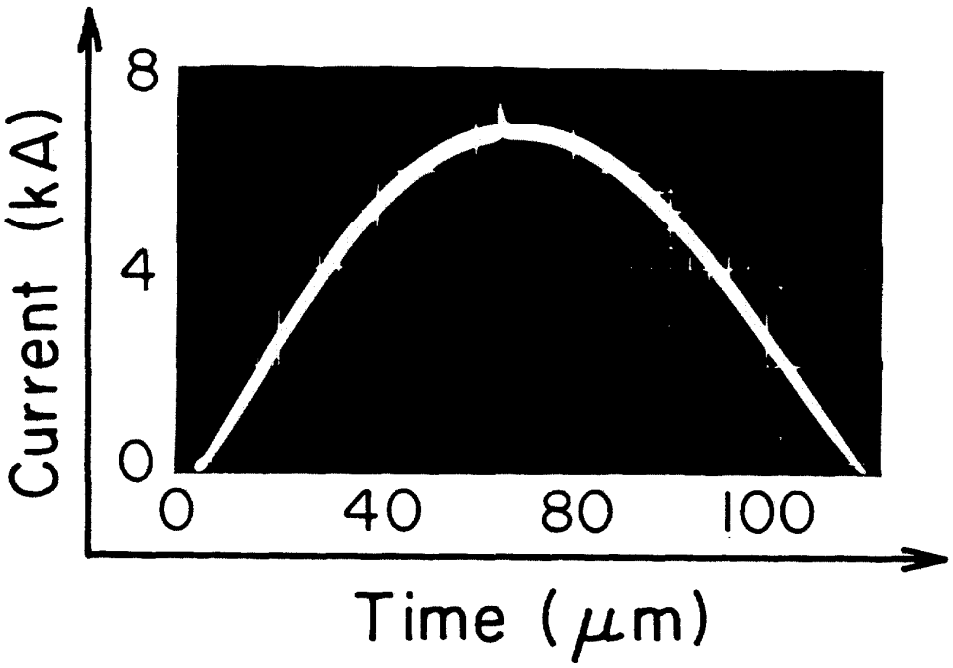

Fig. IV-6. Oscillogram showing time dependence of current through Helmholtz coils during experiment. Sharp pulse at current peak is fiducial mark, which indicates time at which impact occurs.

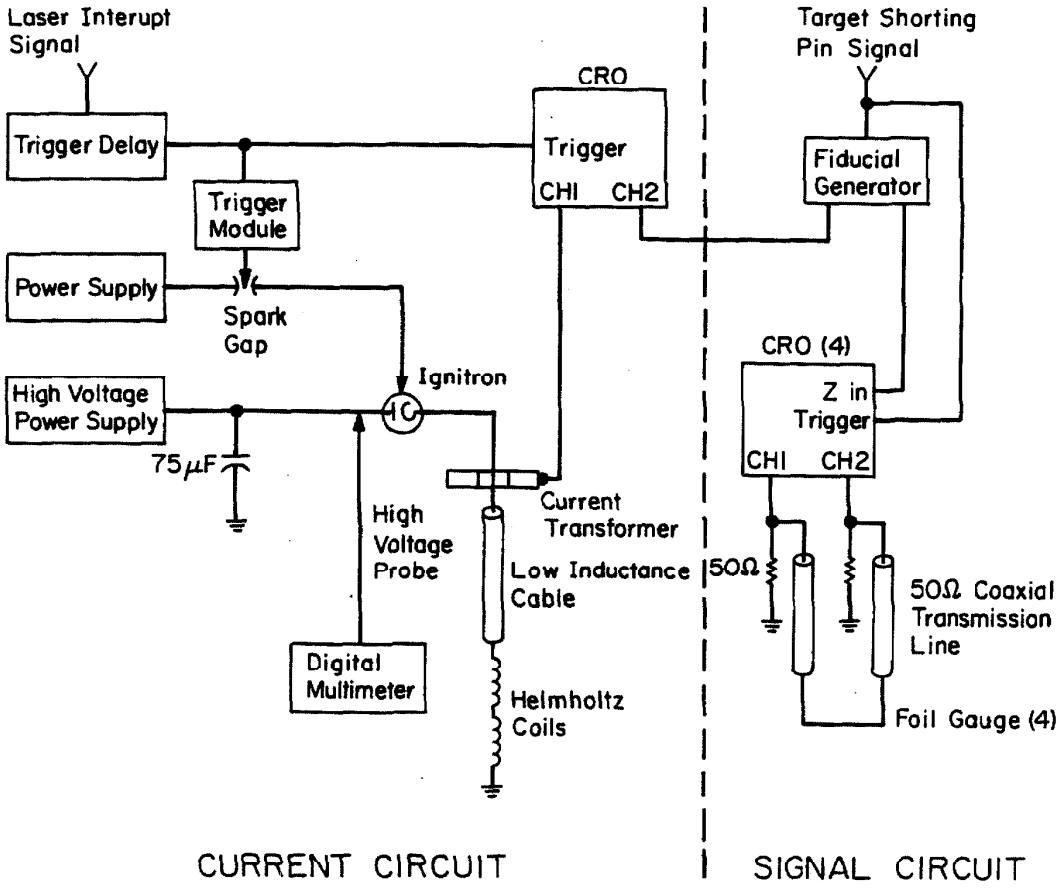

Fig. IV-7. Circuit diagram for particle velocity experiment.

In the signal circuit, self-shorting coaxial shorting pins are used to trigger all four oscilloscopes and a fiducial generator. The fiducial pulse arrives at each oscilloscope 100ns after the oscilloscope trigger. It is 50ns wide, and is fed into the Z channel of each scope. It leaves a gap in the trace which allows synchronization of the signals along the time axis. Each foil lead is connected to the center lead of a coaxial cable and the cable shields are grounded together. The two cables are connected to the two oscilloscope channels and terminated by 50Ω, and the scope is operated on differential mode in order to reduce line noise. Tekronix 475 and 485 models were used in conjunction with Polaroid cameras to record the signals. Time and voltage calibrations were conducted using the Tektronix 485 built-in calibrators.

Not all the particle velocity experiments were conducted with the exact circuit design and set-up outlined above. For example, in some experiments only one cable per gauge was used and the oscilloscopes were not operated in differential mode; and in the early (not always successful) experiments, smaller coils and different gauge fabrication techniques were used. The experiment described here was a product of evolution, and was the most successful.

References

Dremin, A.N., and K.K. Shvedov, The determination of Chapman-Jouget pressure and of the duration of reaction in the detonation wave of high explosives, *Zh. Prikl. Mech. Tekh. Fiz.*, *2*, 154-159, 1964.

Grady, D.E., W.J. Murri, and G.R. Fowles, Quartz to stishovite: wave propagation in the mixed phase region, *J. Geophys. Res.*, *79*, 332-338, 1974.

Kondo, K., Y. Yasumoto, H. Sugiura, and A. Sawaoka, Multiple reverberations in a layer structure observed by particle-velocity and pressure gauges, *Proc. 31st Aeroballistic Range Association Conf.*, 1980.

Larson, D.B. and G.D. Anderson, Plane shock wave studies of porous geologic media, *J. Geophys. Res.*, *84*, 4592-4600, 1979.